GATE Phase III Mean Synoptic-Scale Radiative Convergence Profiles

by
Steven A. Ackerman
and
Stephen K. Cox

Department of Atmospheric Science
Colorado State University
Fort Collins, Colorado

Colorado State University

Department of Atmospheric Science

Paper No. 324

GATE PHASE III MEAN SYNOPTIC-SCALE RADIATIVE CONVERGENCE PROFILES

by

Steven A. Ackerman
and
Stephen K. Cox

Research supported by
The Global Atmospheric Research Program
National Science Foundation and the
GARP Atlantic Tropical Experiment (GATE) Project Office, NOAA
under grants ATM 78-05743 and ATM 78-12631

Department of Atmospheric Science
Colorado State University
Fort Collins, Colorado

March, 1980

Atmospheric Science Paper Number 324

ABSTRACT

Tropospheric radiative convergence profiles are derived for an easterly wave composite during Phase III of the GATE. The easterly waves observed during this period were generally well developed. The profiles also represent the magnitude and the spatial distribution of the Intertropical Convergence Zone (ITCZ) in the GATE area. The 12 hour mean daytime and nighttime profiles are presented. Cloud top pressure distributions, as a function of wave position, are also presented. Day-night differences in the cloud top pressure distributions and radiative convergence profiles are discussed.

The results of this research indicate three possible radiative induced mechanisms which contribute to the observed diurnal cycle in mass convergence. They are:

1) Radiative convergence differences between the ITCZ and the surrounding regions; 2) Mesoscale radiative convergence differences between clear and cluster regions and; 3) A nighttime upper-level tropospheric cooling maximum that is centered one-half a wavelength from the region of maximum convective activity.

ACKNOWLEDGEMENTS

The authors would like to express their appreciation to Professor William M. Gray for his helpful suggestions. Other valuable assistance was provided by Ms. S. Wunch, Ms. P. Martin and Mr. M. Howes during the preparation of this document. The research reported here was supported by the National Science Foundation and the GATE Project Office NOAA under Grants ATM 78-05743 and ATM 78-12631. Acknowledgement is also made to the Aviation Facility and the Computing Facility of the National Center for Atmospheric Research, which is sponsored by the National Science Foundation.

TABLE OF CONTENTS

TABLE OF CONTENTS (Continued)

LIST OF TABLES

LIST OF TABLES (Continued)

LIST OF TABLES (Continued)

LIST OF FIGURES

LIST OF FIGURES (Continued)

LIST OF SYMBOLS

L	-	Radiance
P	-	Pressure
T	-	Temperature
θ	-	Zenith angle, potential temperature
B_ν	-	Planck Function
τ	-	Transmittance
ε	-	Emittance
LWC	-	Liquid water or ice content
K	-	Mass absorption coefficient
Q_R	-	Radiative energy flux convergence
IR	-	Infrared
SW	-	Shortwave
E	-	Irradiance
σ	-	Stefan-Boltzman constant
ρ	-	Reflectance
TTC	-	Total tropospheric convergence
ITCZ	-	Intertropical Convergence Zone
mb	-	Millibars (1 mb = 1 dyne cm^{-2})
ω	-	Vertical velocity in pressure coordinates ($\omega = dP/dt$)
g	-	Acceleration due to gravity
C_p	-	Specific heat of dry air at constant pressure
F_n	-	Net radiative flux
R	-	Gas constant for dry air
λ	-	Wavelength
ν	-	Wave number

I. INTRODUCTION

A primary objective of the GARP[1] Atlantic Tropical Experiment (GATE) radiation subprogram is the determination of the radiative convergence profiles on the time and space scales of the A/B, B and C arrays. This analysis has recently been reported by Cox and Griffith (1979a,b).

To understand the interaction between radiative forcing and large-scale dynamics it is necessary to specify the radiative convergence profiles for an area larger than the scales considered by Cox and Griffith (1979a,b). To date, most diagnostic numerical models designed to study the interaction between synoptic-scale disturbances and the associated cumulus feedback incorporate a climatological mean radiative profile (e.g. Dopplick, 1972). Recent work by Johnson (1979) indicates that the use of a uniform radiative profile in a diagnostic model with spatially varying cloud amounts can lead to significant errors in the determination of convective fluxes.

The purpose of the present study is to (1) investigate possible radiative induced mechanisms which contribute to the observed diurnal cycle in mass convergence and (2) quantify the tropospheric radiative convergence profiles of an easterly wave composite. The tropospheric radiative convergence profiles are calculated for an easterly wave composite during Phase III of the GATE. The area of study is depicted in Figure 1. The easterly waves observed during Phase III (Julian Days 242-262, 1974) of GATE were generally well developed. Therefore, the

---

[1]Global Atmospheric Research Program

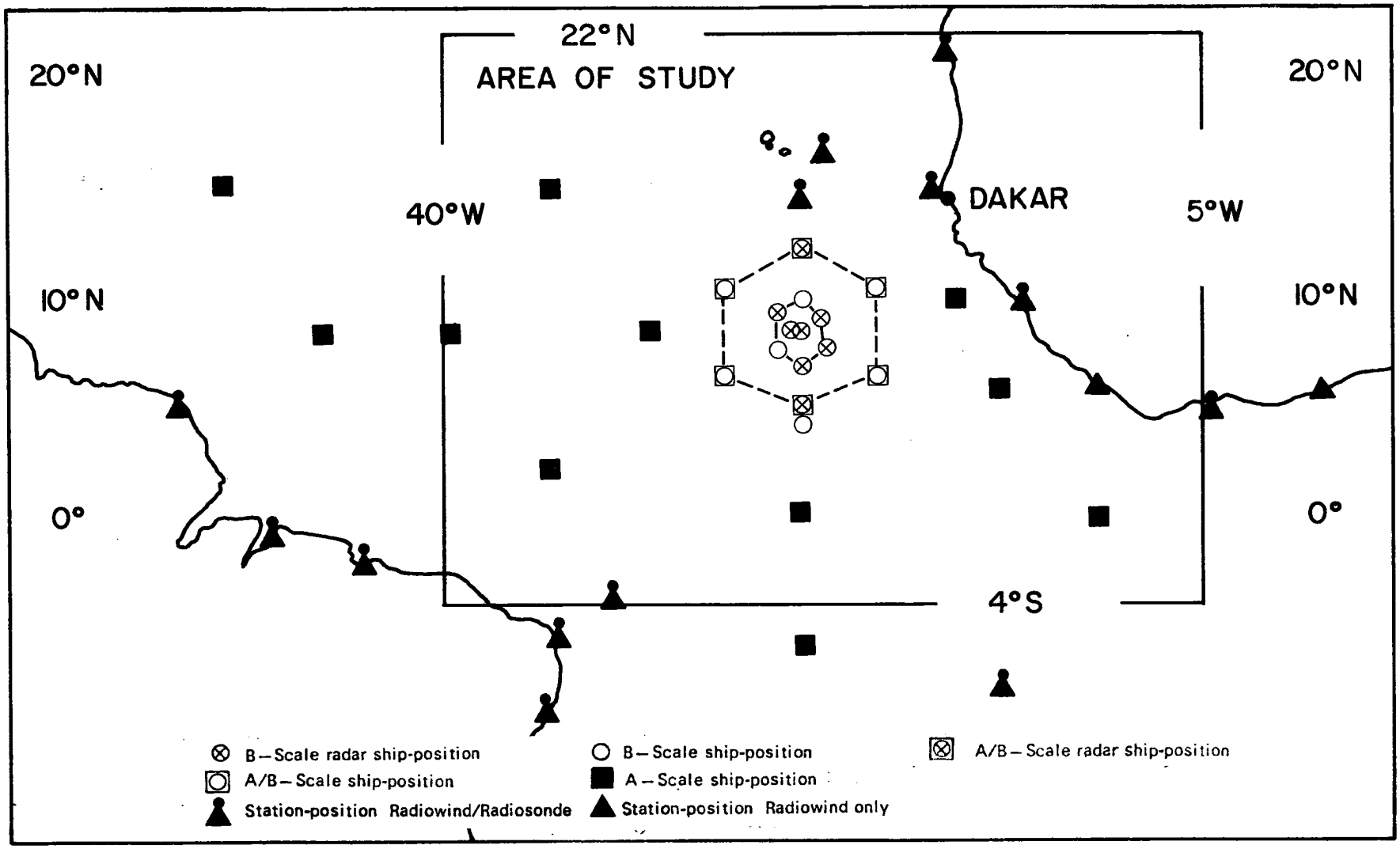

Figure 1. Ship positions during Phase III of GATE.

composite radiative profiles may not be representative of a developing wave. Nor do the results represent the radiative profiles of an easterly wave in other oceanic regions where the cloud structure may differ substantially (e.g. western Atlantic trade wind region). The results are compared with the profiles generated by Dopplick (1972) and Cox and Griffith (1979b).

The wave composite is divided into 56 boxes following the methodology of Reed et al. (1977). The radiative profiles are calculated from broadband radiative transfer routines incorporating the mean horizontal and vertical distributions of temperature, specific humidity, carbon dioxide, ozone and clouds for each of the 56 boxes. A discussion of the possible effects on the radiative profiles due to Saharan aerosols is included. A positive convergence in a layer refers to the layer warming, and negative values always refer to cooling.

A composite cloud top distribution as a function of wave box and pressure is also derived and compared with results of other researchers. The composite cloud top distribution and radiative profiles for the 12 hour daytime and nighttime means are presented separately and the differences are discussed. Possible radiative induced mechanisms which might contribute to the observed day vs. night differences in mass convergence and cloudiness are presented.

II. COMPOSITE SCHEME

The computation of radiative flux convergence profiles requires a knowledge of the vertical and horizontal distributions of temperature, water vapor, clouds, ozone, carbon dioxide and aerosols. In this section the vertical and horizontal distributions of these parameters used in a model to calculate the radiative flux convergence profiles of an easterly wave are discussed. Reed et al. (1977) have composited easterly wave disturbances during Phase III of GATE, dividing the disturbances into fifty-six boxes, (eight columns and seven rows). The horizontal and vertical (up to 100 mb) distributions of temperature and specific humidity for the present study are taken from the composite wave structure given by Reed et al. (1977). Above 100 mb, temperature and moisture distributions of the Standard Tropical Atmosphere are assumed. Carbon dioxide is assumed constant at .486 g/kg. The vertical distribution of ozone is that of a Standard Tropical Atmosphere. In assessing the aerosol contribution, knowledge of the vertical and horizontal distribution of aerosols is essential for latitudes north of 10°N, where most of the Saharan dust out-breaks occur (Carlson and Prospero, 1972; Prospero and Carlson, 1972). Carlson and Prospero (1972) have shown that the greatest dust concentrations occur to the east of an easterly wave trough, with small concentrations at and west of the trough. Maximum dust concentrations in the vertical occur generally between 1.5 - 3.7 km. From the researches of Minnis and Cox (1978), Paltridge and Platt (1973) and Liou and Sasamori (1975) it appears that the Saharan dust layer primarily affects the shortwave spectral region. Kondratyev et al. (1976) imply that longwave cooling

is small except perhaps near the top of the dust layer. Assumed horizontal and vertical distributions of the Saharan aerosols are discussed in Section 4.2.2.

The vertical and horizontal distribution of clouds is a difficult parameter to asses and the most critical since clouds have the largest effect on radiative energy fluxes. To date, there have been no adequate cloud distribution studies for such a large synoptic feature. Payne and McGarry (1977) have used satellite infrared (IR) images to study spatial and temporal relationships between convective activity and the easterly wave. Reed et al. (1977) composited high, middle and low cloud top amounts as a function of wave category. Although useful for comparisons, these studies do not provide adequate vertical resolution which is needed for the calculation of the vertical convergence profiles. The remaining part of this section deals with the method employed to determine the vertical and horizontal distributions of clouds.

2.1 Cloud Top Distribution

During Phase III of GATE eight easterly waves moved across the A/B-scale array. Rather than deal with eight wave disturbances at each observation hour, we began the study by limiting ourselves to four different hours when the 700 mb streamlines were approximately sinusoidal. These hours of well-developed wave disturbances (Figures 2-5) are Julian days 244 0000 GMT, 244 1200 GMT, 246 1800 GMT and 254 0000 GMT. To include and investigate diurnal variations, periods $\pm$ 6 and $\pm$ 12 hours about the original four disturbances were included in the composite making a total of 17 observational periods. It is

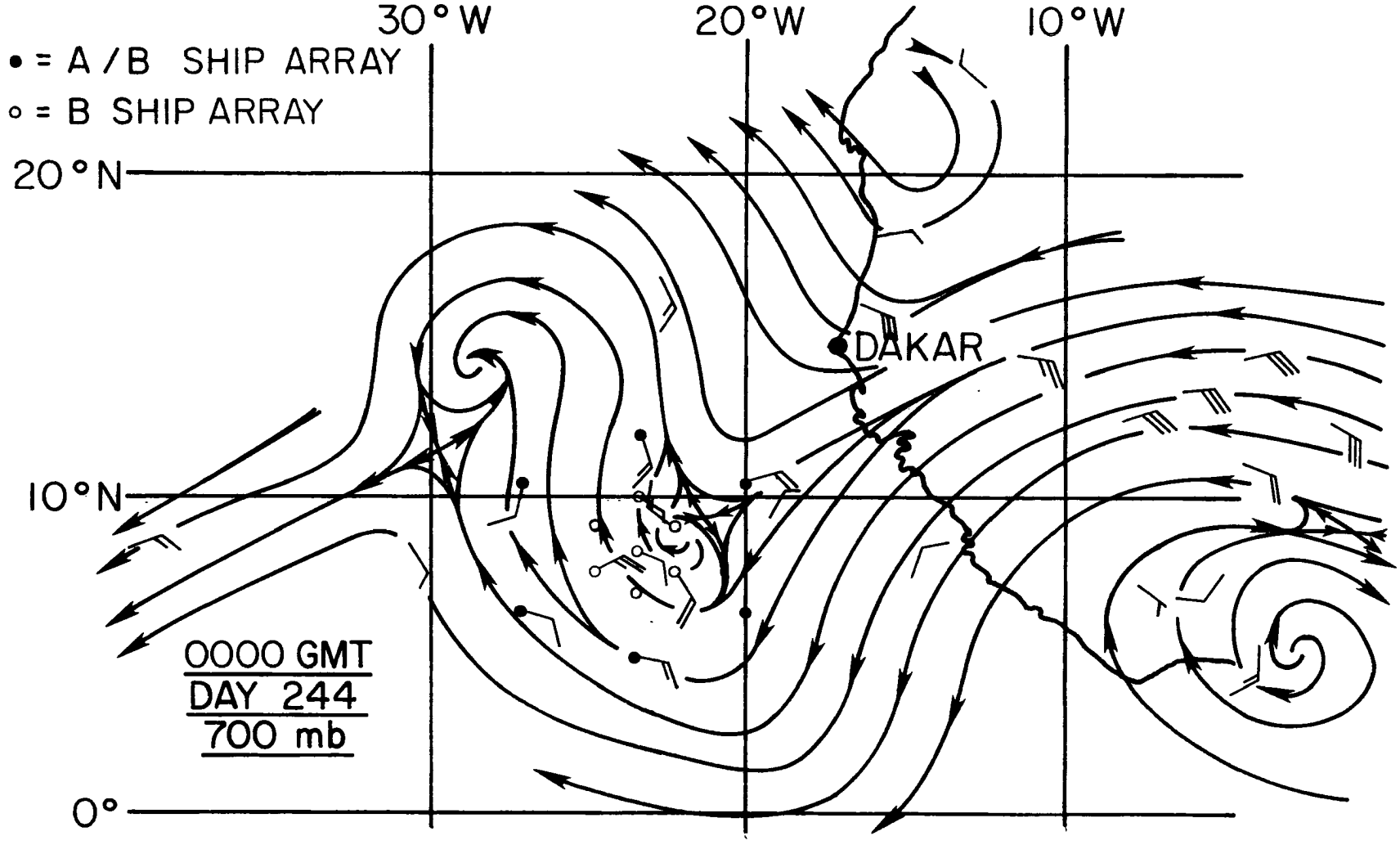

Figure 2. 700 mb streamline analysis for Day 244 at 0000 GMT.

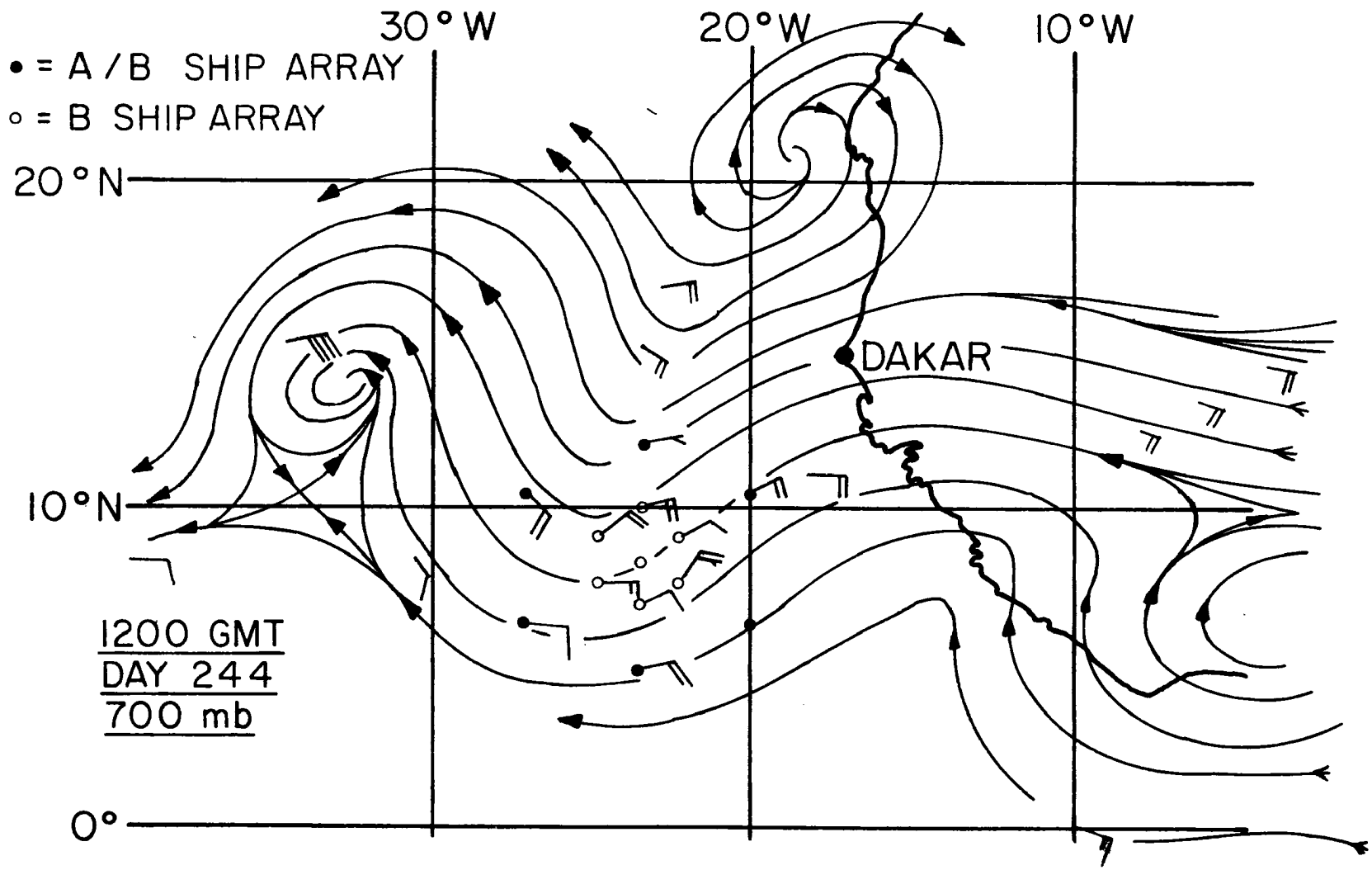

Figure 3. 700 mb streamline analysis for Day 244 at 1200 GMT.

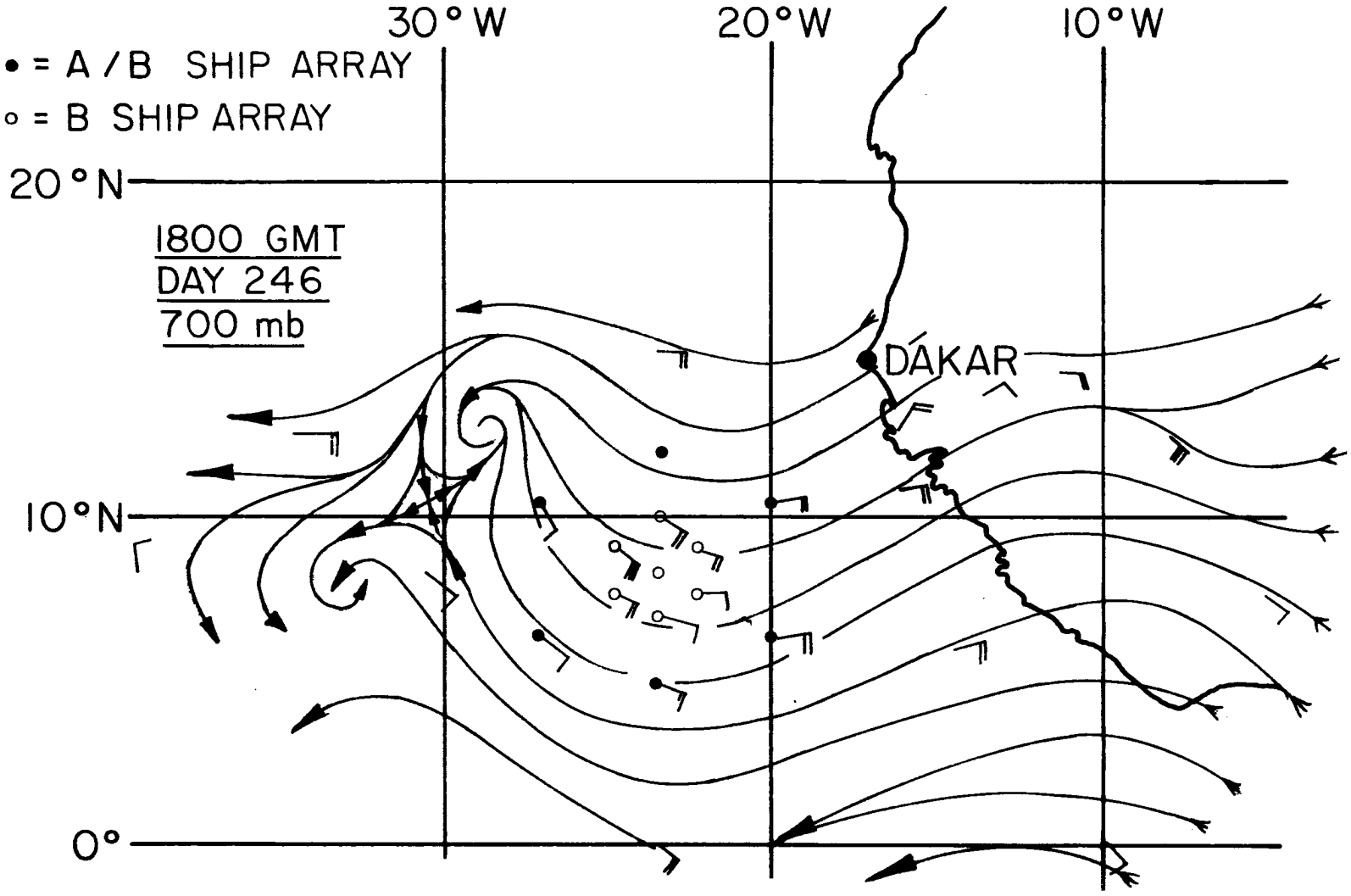

Figure 4. 700 mb streamline analysis for Day 246 at 1800 GMT.

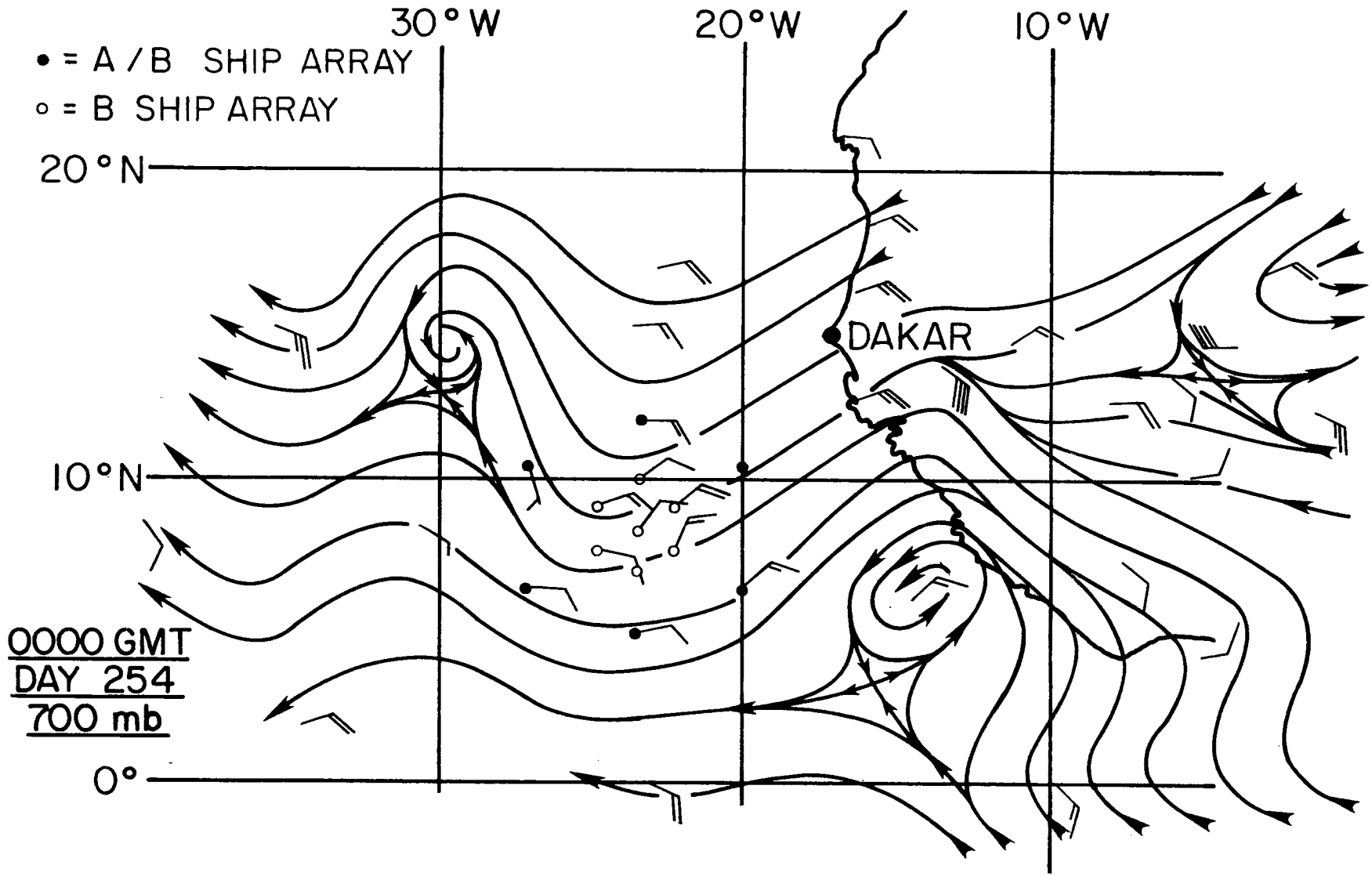

Figure 5. 700 mb streamline analysis for Day 254 at 0000 GMT.

interesting to note that the 17 case studies tended to be fixed geographically. Recently, Johnson (1979) showed a tendency for a preferred geographic location of the easterly wave with respect to time of day for the entire Phase III period. This suggests a possible land-sea interaction coupled with the wave dynamics.

Following Reed et al. (1977), the waves were spatially divided into 56 boxes or categories, producing a matrix of seven rows and eight columns. Column 2 is centered on the region of the maximum northerly wind component, column 4 on the trough, column 6 on the region of maximum southerly wind component and column 8 the ridge. Columns 1, 3, 5 and 7 occupy intermediate positions. Δ latitude 0 (Row 4) is the path of the 700 mb disturbance, defined as the point of maximum vorticity. Other rows are then placed 4° apart, starting from Δ latitude 0 for a total meridional extent of 28°. The ITCZ (Intertropical Convergence Zone) and the A/B-scale array lie between Δ latitude 0 and Δ latitude -4.

Cloud top determination is analogous to that reported by Cox and Griffith (1979a) [hereafter referred to as CG]. An equivalent black body cloud top temperature is calculated from the GOES Synchronous Meteorological Satellite (SMS-1) IR brightness data using an algorithm developed by Smith (1977). Using the black body temperature an apparent cloud top pressure is obtained from the composite temperature profiles. To better estimate the apparent cloud top pressure two corrections are applied to the cloud top black body temperature (T_{EBB}). The first accounts for the water vapor emission ($\Delta T_{WATER\ VAPOR}$) in the "window" region (10.5 μm to 12.5 μm) that the satellite senses. The second is the penetration distance into the cloud before radiative

"blackness" is achieved ($\Delta T_{PENETRATION}$). With these correction terms the apparent cloud top temperature is written as:

$$T_{APPARENT} = T_{EBB} - \Delta T_{WATER\ VAPOR} + \Delta T_{PENETRATION}. \qquad (2.1)$$

This $T_{APPARENT}$ is converted to an IR brightness value using the previously mentioned algorithm devloped by Smith (1977). Thus, each cloud top level may be associated with an IR brightness value. The two cloud top temperature corrections are determined at 50 mb intervals for each of the 56 wave categories.

First let us address the water vapor emission correction, which is primarily of concern below 500 mb. The concept used is to place a "black slab" at a known pressure level and compute the spectral radiance (905 - 915 cm^{-1}) at the top of the atmosphere. Assuming Planck emission the computed radiance (assumed to be the satellite measured radiance) is converted to a black body temperature. The difference between the black body temperature and the observed temperature at the pressure level of the "black slab" is the correction term ($\Delta T_{WATER\ VAPOR}$) for that pressure level. This type of computation was performed for each 100 mb layer below 500 mb using a spectral infrared band model of Cox et al. (1976) hereafter referred to as RADLON. The model numerically integrates the radiative transfer equation;

$$L_\nu(0,P) = -\int_P^{P_o} B_\nu(0,T)\,\frac{\partial \tau_\nu}{\partial P}\,dP + B_\nu(0,T_o)\int_P^{P_o}\frac{\partial \tau_\nu}{\partial P}\,dP \qquad (2.2)$$

where L_ν - spectral radiance

P - pressure

T - temperature

θ - zenith angle

B_ν - spectral Planck function

τ_ν - spectral transmittance = $\pi \tau_{\nu i}$ (index i refers to different absorbers).

Values at each 50 mb layer are linearly interpolated.

Next we consider the problem of penetration distance into the cloud top before radiative blackness is seen by the satellite. Assuming a cloud liquid water (ice) content (LWC), a mass absorption coefficient (k) and a cloud emittance (ε) the penetration distance (Δz) is calculated from

$$\varepsilon = 1 - \exp -(LWC * k * \Delta z). \qquad (2.3)$$

Clouds are assumed to have the liquid water (ice) contents of Cox and Griffith (1979a). All clouds are assumed to have a mass absorption coefficient of .045 $m^2\ g^{-1}$. The penetration distance is converted to a temperature correction ($\Delta T_{PENETRATION}$) using the temperature profile of the box in question. The cloud and environment are assumed to have the same temperature profile.

In determining cloud top levels we have assumed all clouds to be optically thick. In the case of thin cirrus, the satellite will measure an equivalent black body temperature that is a combination of the cold cirrus and warmer background temperature. Application of the

method described above results in a middle level cloud top. Similar errors also occur with clouds with emittances less than 1.0, broken cloud fields and variable cloud tops within the satellite resolution.

The area of interest (22°N to 4°S and 40°W to 5°W; see Fig. 1) was divided into 1° longitude by 1° latitude squares. Each square was assigned a box number from 1-56, depending on its position within the wave. Cloud top distributions were determined for each square and composited with respect to wave position for each of the 17 time periods. The 17 individual periods were then combined to obtain a total composite of cloud top pressure distribution as a function of wave position.

The method described and discussed above is a compositing technique for determining the horizontal and vertical distribution of cloud top pressure levels. We next address the problem of assigning cloud base distribution.

2.2 Cloud Base Distribution

A simple parameterization scheme to deduce cloud base height is to allow only "thin" and "thick" clouds with no overlapping. Thin clouds are defined as having cloud base within the same 100 mb layer as the cloud top. For the "thick" clouds, cloud base is assumed at 950 mb. In an attempt to determine the percentage of thick clouds, radar echo composites compiled by R. Arkell and M. Hudlow (1977) were used. It is assumed that precipitating areas have a low cloud base (e.g. 950 mb) and nonprecipitating regions are composed of thin clouds. The C-band radars aboard Gillis, Quadra, Oceanographer and Researcher were used to delineate precipitating regions.

The radar composites are overlaid by a 1/2° x 1/2° grid and bright areas that are nonprecipitating (e.g. "sea clutter") are darkened. The pictures are then digitized using the All Digital Imaging System for Atmospheric Research (ADVISAR) camera system and displayed on a video screen. By use of the cursor, a digital brightness threshold corresponding to precipitating regions is determined. Percent areas of precipitation for each 1/2° square can then be objectively determined by comparing the number of digital counts above the specified threshold to the total number of counts. Areas of precipitation are then correlated with the box mean satellite derived IR brightness. The 1/2° box mean IR brightnesses are assumed representative of an individual brightness value.

Another possible method of determining vertical cloud base distribution is by using some of the tabulated data given by Holle et al. (1977). Using all-sky cameras, Holle et al. (1977) correlated a convective code (see GATE Information Bulletin #8) with four categories of observed cloud base: low, middle, upper undifferentiable, and high. It is a difficult task to correlate convective activity with convective satellite imagery. However, once such a relationship is established, the method described below can be used to determine the vertical structure of clouds, again assuming no multilayered clouds. Figure 6 shows the type of cloud structure assumed and the notation used. The first capital letter denotes cloud top and the subscript denotes cloud base. Thus, H_H represents a high cloud top with high cloud base.

From satellite data, one can obtain the percent of low cloud tops (L^T), middle cloud tops (M^T), and high cloud tops (H^T). From the all-sky camera data of Holle et al. (1977) the percent areal coverage of

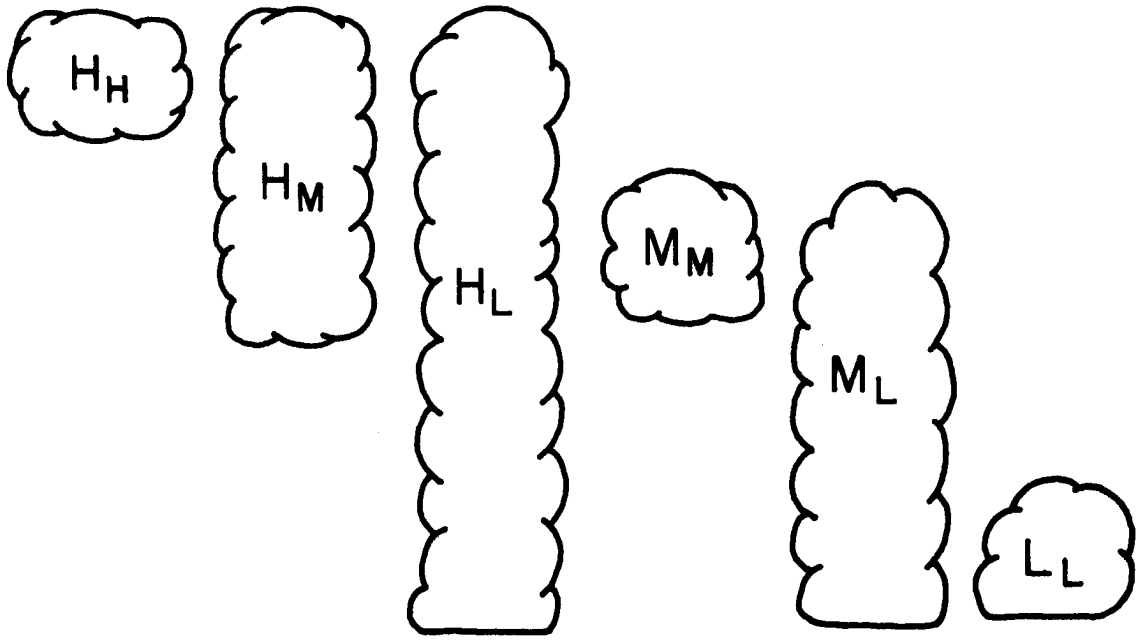

Figure 6. Schematic view of assumed cloud structure; for explanation of notation see text.

low cloud bases (L^B), middle cloud bases (M^B) and high cloud bases (H^B) as a function of convective code is known.

The percentage of low cloud tops with low cloud bases (L_L) is simply the percent of low cloud tops determined from the satellite images (L^T). Similarly the amount of high cloud tops with high cloud bases (H_H) is the percentage of high cloud bases (H^B) determined from the all-sky camera. That is,

$$L_L = L^T \quad \text{and} \quad H_H = H^B. \tag{2.4}$$

Thus,
$$L^{B'} = L^B - L^T \quad \text{and} \quad H^{T'} = H^T - H^B \tag{2.5}$$

where $L^{B'}$ denotes the total percentage of low cloud base that is to be distributed among M_L and H_L, and $H^{T'}$ is the percent of high cloud tops to be distributed among H_L and H_M. One can derive a set of three equations (Eq. 2.6-2.8) with four unknowns: M_L, M_M, H_L, and H_M

$$M_L = M^T - M_M \tag{2.6}$$

$$H_L + H_M = H^{T'} \tag{2.7}$$

$$M_M - H_L = M^T - L^{B'}. \tag{2.8}$$

From the radar-satellite analysis described above, we assign the percent coverage of H_L and solve the set of equations for the rest of the unknowns. Section 3.1.1 compares the differences in the computed

radiative energy flux convergence profiles using the two methods described above to obtain vertical cloud structure.

III. METHOD OF COMPUTING FLUX CONVERGENCE PROFILES

The radiative energy flux convergence profiles are calculated from the vertical distribution of temperature, specific humidity, clouds, ozone, aerosol, and carbon dioxide. The radiative energy flux convergence profiles, Q_R, may be partitioned into a longwave or infrared component (λ = 3.0 μm → 55 μm) and a shortwave or solar component (λ = .3 μm → 3.0 μm). Thus,

$$Q_R = Q_{IR} + Q_{SW}. \tag{3.1}$$

The models used in computing Q_{IR} and Q_{SW}, for each of the 56 wave boxes, have been discussed by CG (1979a,b) and are, where appropriate, briefly outlined below.

3.1 Longwave Profiles

From the vertical distributions of temperature, specific humidity, ozone, clouds and carbon dioxide, Q_{IR} is calculated by solving the radiative transfer equation in its finite difference form:

$$E(p) = E_o \left[1 - \sum_{i=1}^{n} \Delta\varepsilon_{iH_2O} - \sum_{i=1}^{n} \Delta\varepsilon_{iCO_2} - \sum_{i=1}^{n} \Delta\varepsilon_{iO_3} - \sum_{i=1}^{n} \Delta\varepsilon i_{CLOUD}\right.$$

$$\left. + \sum_{i=1}^{n} \Delta\varepsilon_{iOVERLAP}\right] + \sum_{i=1}^{n} E_i \left[\Delta\varepsilon_{iH_2O} + \Delta\varepsilon_{iCO_2} + \Delta\varepsilon_{iCLOUD}\right. \tag{3.2}$$

$$\left. - \Delta\varepsilon_{iOVERLAP}\right]$$

where E(p) is the upward or downward irradiance of pressure level P. E_o is equal to σT_i^4, where T_i is the average absolute temperature of the layer i, $\Delta\varepsilon_{iH_2O}$, $\Delta\varepsilon_{iCO_2}$, $\Delta\varepsilon_{iO_3}$, and $\Delta\varepsilon_{iCLOUD}$ are the emittance increments in the layer from each of the constituents H_2O vapor, CO_2, O_3, and clouds. Both the H_2O - CO_2 gaseous overlap region and the H_2O - CO_2 vs. cloud overlap region are presented by $\Delta\varepsilon_{iOVERLAP}$. The computational technique, referred to as IRADLON-2, in solving Eq. 3.2 is discussed by Cox et al. (1976) and Griffith et al. (1980).

It is appropriate here to review the assumed cloud properties in computing Q_{IR}. The reader is referred to Starr (1976) where the sensitivity of these assumptions on Q_{IR} is discussed.

1. Specific humidity and temperature profiles within the cloud are equal to the enviornmental profiles.
2. All clouds are assumed to have an emittance of 1.0. The effects of thin cirrus have, therefore, been ignored. The resulting errors are discussed in later sections.
3. Cloud liquid water (ice) contents correspond to those of CG.
4. Cloud mass absorption coefficient is assumed to be $0.045\ m^2 g^{-1}$.
5. Clouds are assumed to be "thin" or "thick". Multilayered clouds are treated as single layer clouds or as thick clouds.
6. Cloud tops for "thick" clouds are placed in the middle of the layer they occupy. Cloud top placement for thin clouds is the same except for high

clouds. For high clouds above 400 mb, the tops are placed at a level such that cloud emittance is greater than .95.

7. The vertical distribution of cloud base is based on a statistical correlation between satellite IR brightness and radar echo. The following section explores the sensitivity of cloud base assignment on the radiative convergence profiles.

3.1.1 Sensitivity of Cloud Base Distribution and Cirrus Contamination to Radiative Convergence Profiles

Section 2.2 discussed two possible methods for assigning cloud base distribution. The present study uses the statistical distribution obtained from the radar-satellite analysis (RSA). In this section the radiative convergence profiles resulting from the RSA cloud base distribution are compared with the radiative profiles computed using two other methods of assigning cloud base distributions. The method using all-sky cameras (ASC) was discussed previously. The third method (EVEN) partitions the cloud base distribution evenly among the predetermined cloud top amounts. For example, if the satellite determines a 20% areal coverage of cloud top between 200 mb and 100 mb, 1/3 of the 20% is distributed among 200-100 mb cloud tops with high cloud base, 1/3 to 200-100 mb cloud top with middle cloud base and 1/3 to 200-100 mb cloud top with low cloud base.

Two cloud top distributions are applied. One representative of a convectively active cloud cluster, the other of the cloud cluster environment. These cloud top distributions were computed from data

tabulated by CG. The cluster and environment are assumed to have the same vertical distribution of temperature and specific humidity as category 4-4 (Δ latitude 0 at the trough position) of the Reed et al. (1977) easterly wave composite.

The results of the three methods of cloud base assignment are shown in Figure 7 and Figure 8. Total tropospheric convergence (TTC) is given in parentheses. We first note that the maximum TTC difference between the three methods is less than 10%. For any given 100 mb layer, the largest discrepancy occurs in the 100-200 mb layer of the active cluster (Fig. 7). This difference being approximately 10 W m^{-2} $(100\ mb)^{-1}$. There is little difference between the three methods when applied to the environment cloud distribution (Fig. 8). The largest difference is approximately 5 W m^{-2} $(100\ mb)^{-1}$.

As previously mentioned, the algorithm of cloud top assignment misinterprets clouds with emittacnes less than 1.0, placing them at a lower height. Let us consider a thin cirrus cloud at 200 mb overlying an otherwise clear regime. The algorithm placement of cloud top height is a function of the cirrus emittance. This apparent cloud top height as a function of cirrus emittance may be calculated in the following manner:

1) assume a cirrus spectral emittance, ε_ν

2) calculate the radiance at the top of the atmosphere from

$$L\uparrow = (1 - \varepsilon_\nu)\, B_{\nu \text{Surface Temp.}} + B_{\nu \text{Cloud Temp.}} \qquad (3.3)$$

where $B_\nu \equiv$ Planck's function.

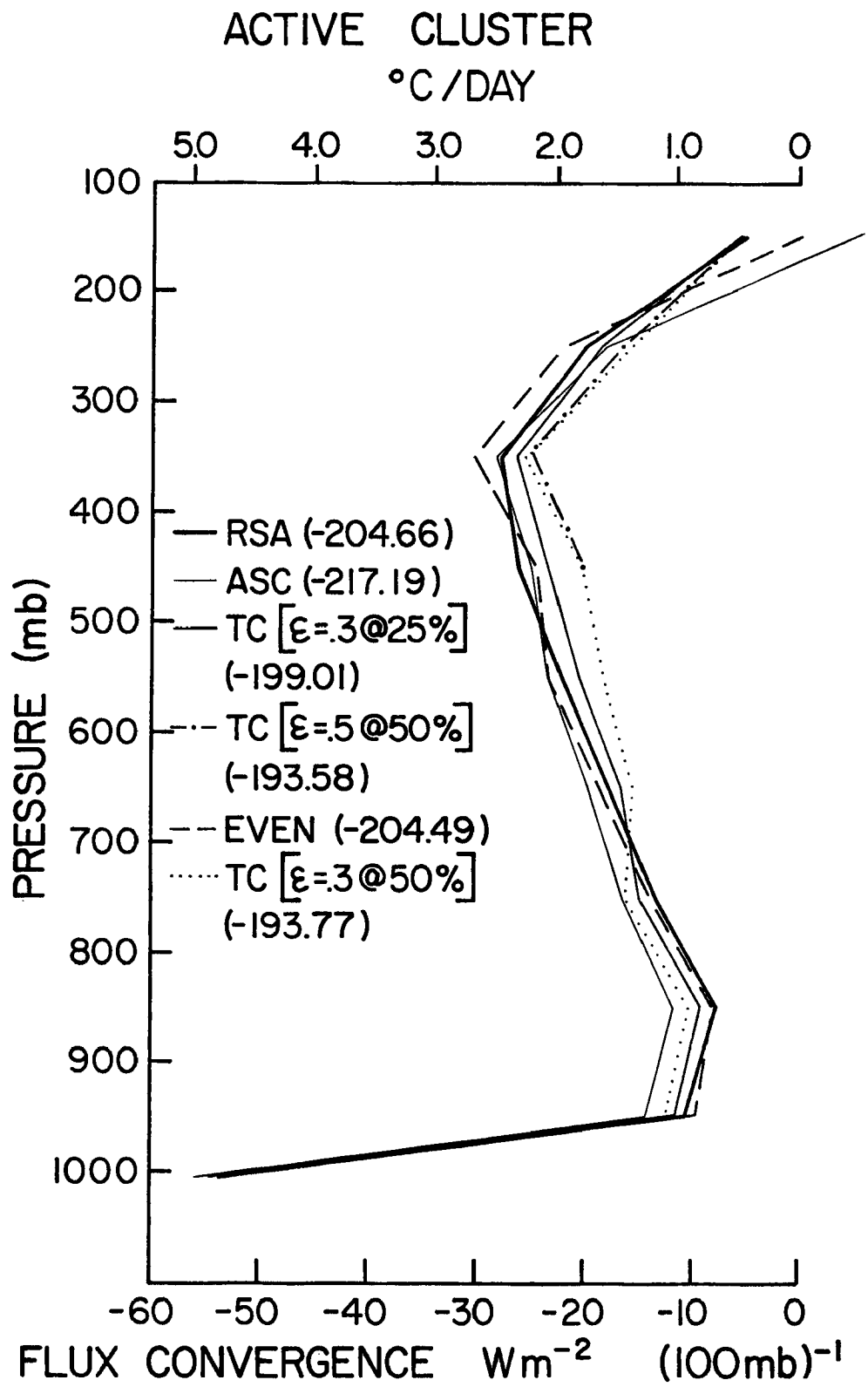

Figure 7. Radiative convergence profiles for an active cluster assuming varying distributions of cloud base and thin cirrus. Values in parentheses denote total tropospheric convergence. RSA: radar-satellite analysis; ASC: all-sky camera; EVEN: even distribution; TC: thin cirrus, brackets contain cirrus emittance and assumed areal coverage.

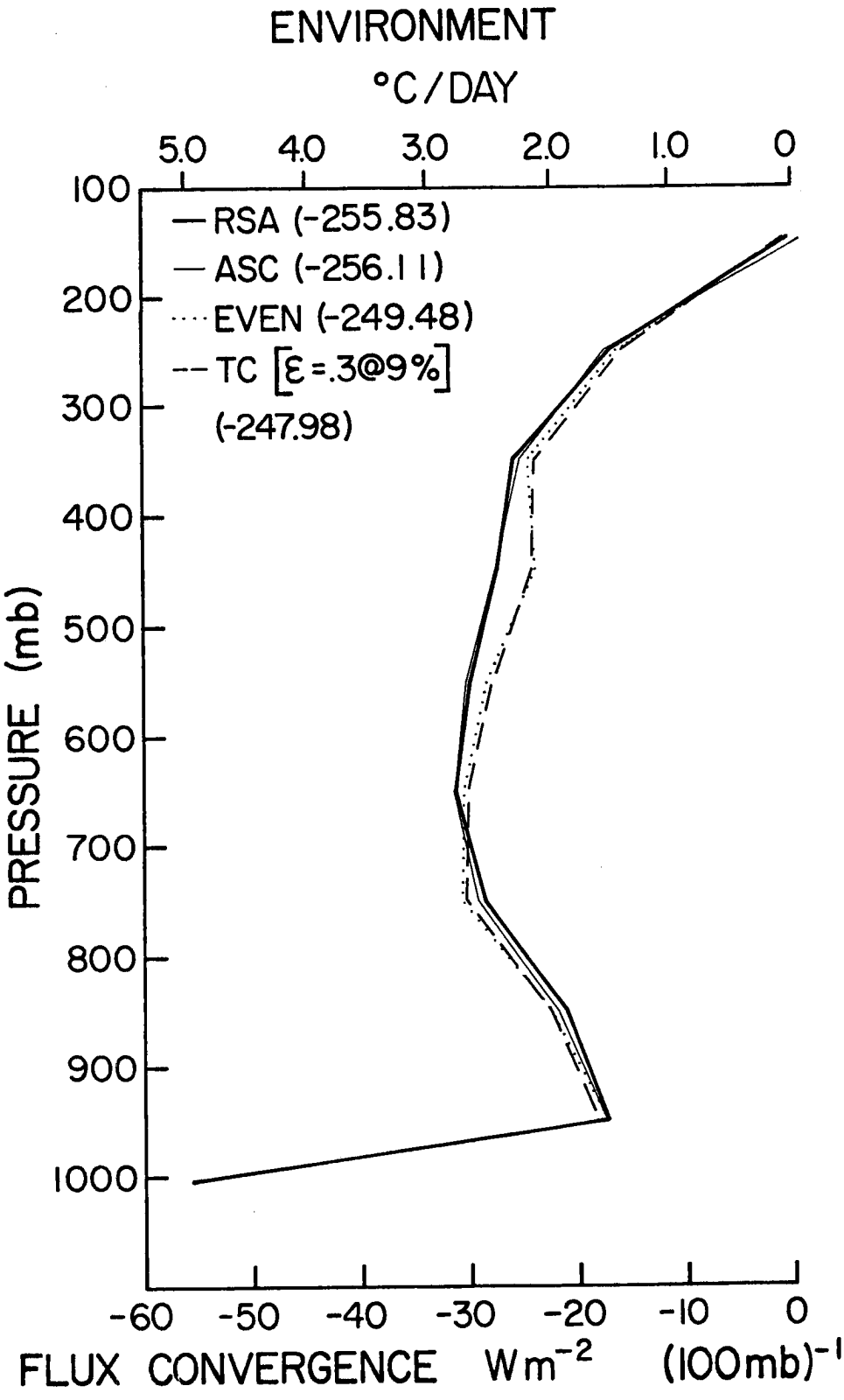

Figure 8. Radiative convergence profiles for the cluster environment assuming varying distributions of cloud base and thin cirrus. See Fig. 7 for explanation of acronyms.

3) Using Planck's function, calculate an equivalent black body temperature. From the assumed temperature profile locate the cloud top pressure.

Figure 9 is a plot of apparent cloud top height as a function of cloud emittance for a cloud top at 200 mb. One notes that a cloud top at 200 mb with an emittance between .3 and .6 will be misinterpreted as a middle level cloud top.

Let us assume that 9% of the total area of the environment is covered with thin cirrus with emittance between .3 and .6. To account for this contamination, 9% of the middle cloud tops, 400-600 mb, is evenly subtracted from each of the three levels. This 9% is assumed to be the percent coverage of thin cirrus. The resulting radiative divergence profiles are shown in Fig. 8. The difference in the TTC is less than 5%. The maximum layer difference is only 5 W m^{-2} (100 mb)$^{-1}$.

In the case of a convectively active cluster, one might expect some thin cirrus outflow. To test the sensitivity of thin cirrus in the active cloud cluster model, it is assumed that the thin cirrus has an emittance of .3 or .5 and an areal extent that is 25% (and 50%) of the total percentage of cloud tops above 400 mb. To conserve the total cloud top amount, this percentage of thin cirrus is subtracted from the 400-600 mb cloud tops. The results are shown in Fig. 7. Maximum TTC difference is approximately 11%. As expected, the largest difference occurs in the 400-600 mb layer.

The two cloud top distributions used in the above sensitivity study represent time and spacial averages. As one investigates smaller space and time scales, one would expect the errors discussed above to become larger. However, for the present study, the simple

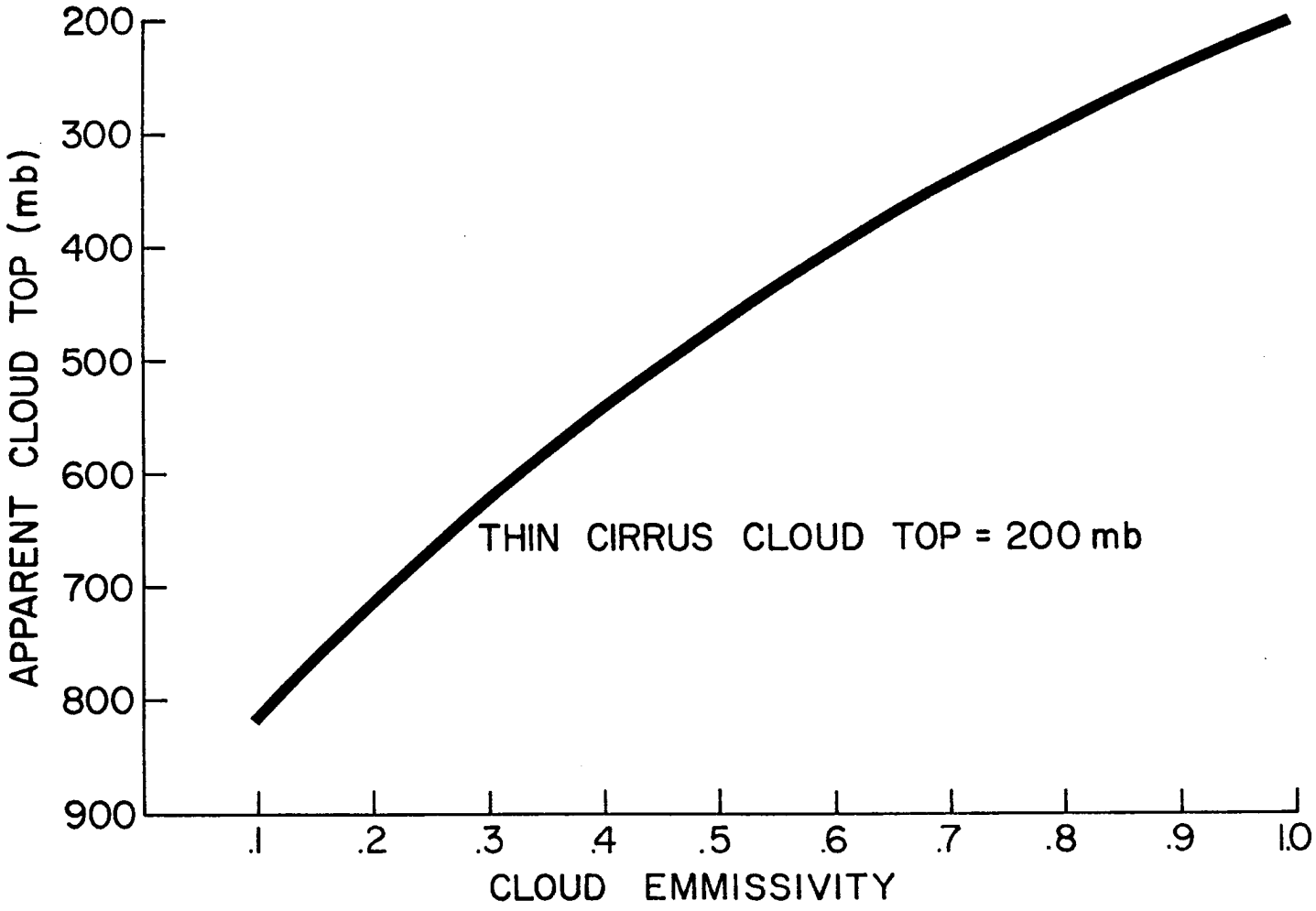

Figure 9. Apparent cloud top height as a function of cloud emittance.

parameterization of cloud base and thin cirrus distribution is an adequate first order approximation.

3.2 Shortwave Profiles

The shortwave profiles used in deriving the energy flux convergence profiles are based on a broadband shortwave model described by Cox et al. (1976), and is referred to as IRADS02. The irradiance at a level n, in the atmosphere is computed from the finite difference form of Beer's Law, i.e.

$$E_n = E_o \exp -\left(\sum_{i=0}^{N} \Delta\tau_n\right) \tag{3.4}$$

where $E_n \equiv$ is the irradiance at level n

$E_o \equiv$ is the incident irradiance at the top of the atmosphere

$\Delta\tau_n \equiv$ is the optical thickness of the n-i layer.

The absorption coefficients used to compute the optical thickness are taken from Manabe and Strickler (1964).

Absorption in clouds is based on the theoretical calculations of Welch et al. (1980) and the GATE aircraft observations of Griffith et al. (1980). All clouds are assumed to be 1 km in depth so that absorption below cloud base is neglected (Welch et al. 1980).

Minnis and Cox (1978) have shown a significant amount of solar absorption in the Saharan dust layer. An estimate of the effects of aerosols on the shortwave convergence profiles will be discussed in Section 4.2.2. Unless otherwise specified, daytime and 24 hour radiative convergence profiles include both the shortwave and longwave components.

IV. RESULTS

4.1 Cloud Top Distribution

A total cloud top distribution composite was derived from the 17 individual composites, representing a time and space average over both land and ocean areas.

To compare our results with those of Reed et al. (1977), an analysis of cloud top pressure above 400 mb is shown in Figure 10. An analysis of Reed's category "2" type clouds (bright - presumably of convective origin) is also shown. We first note that maximum high cloud percentage occurs in the category slightly west of the disturbance center. The main discrepancy between Reed's and the present results is the magnitude of areal coverage. However, the magnitudes should not necessarily be identical since the two compositing techniques are somewhat different. In Reed's composite, 46% of the 1° squares that comprise the maximum area of bright clouds were assigned a brightness value of 2. That is 46% of the boxes appeared to be at least 50% covered with high cloud. The maximum magnitudes of the present study are interpreted as the maximum area of bright clouds which has 40% of its area covered with cloud tops above 400 mb.

Figure 11 is a comparison between the present study's clear and low clouds (below 800 mb) and Reed's category "0" clouds (clear areas and low clouds). Both studies have a minimum near the center of the disturbance. The present study shows a larger minimum (31%) in this region than that of Reed (25%). There is also a large discrepancy in the northern and southern section of the wave due to the middle-level clouds observed in the present composite (Table 1). The IR satellite

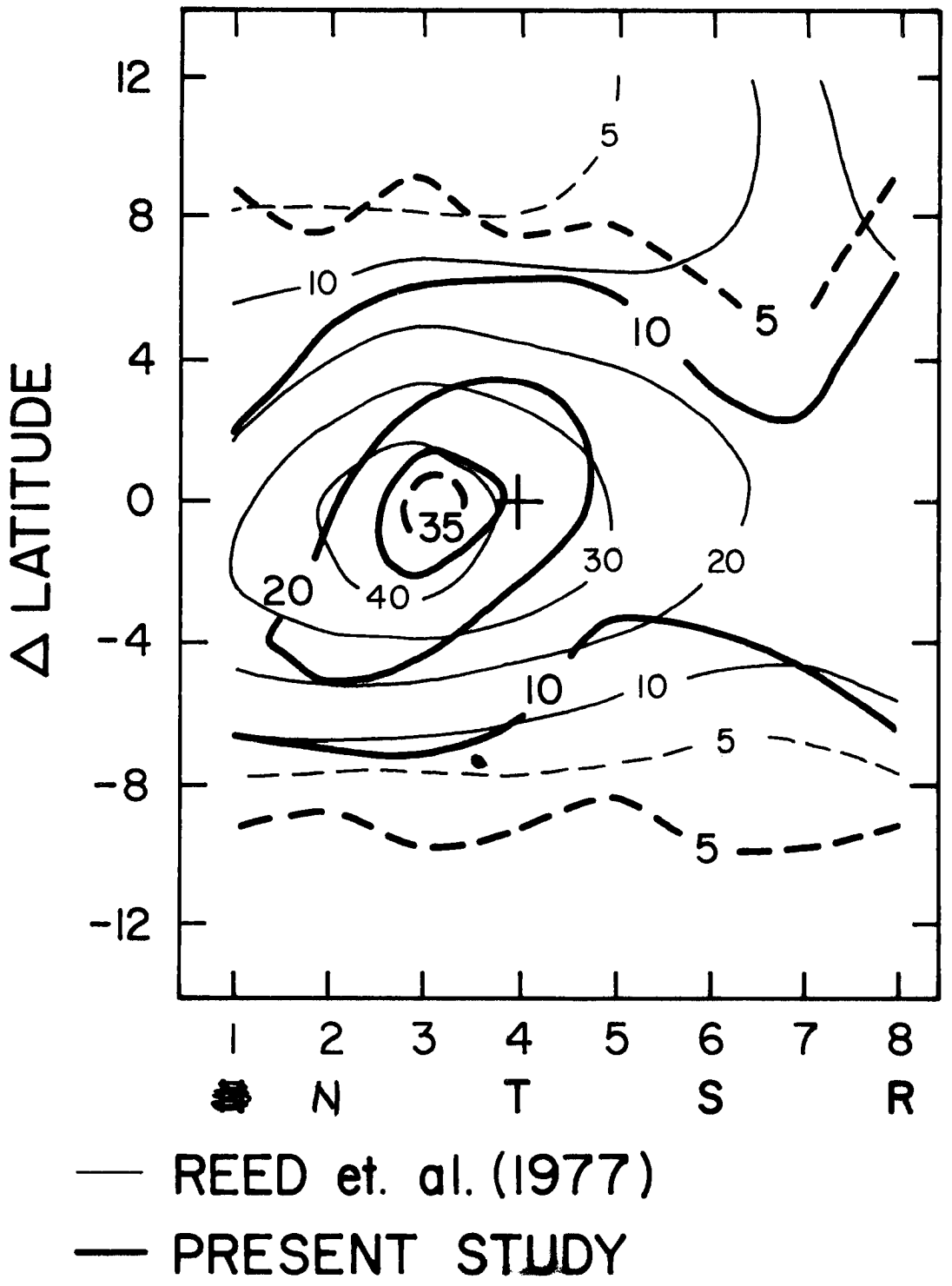

Figure 10. Percent coverage of high cloud as a function of wave position. Δ latitude 0 is the path of the 700 mb disturbance center. N - region of maximum northerly winds; T - trough; S - region of maximum southerly winds; R - ridge. Cross marks the center of the wave. [redacted]

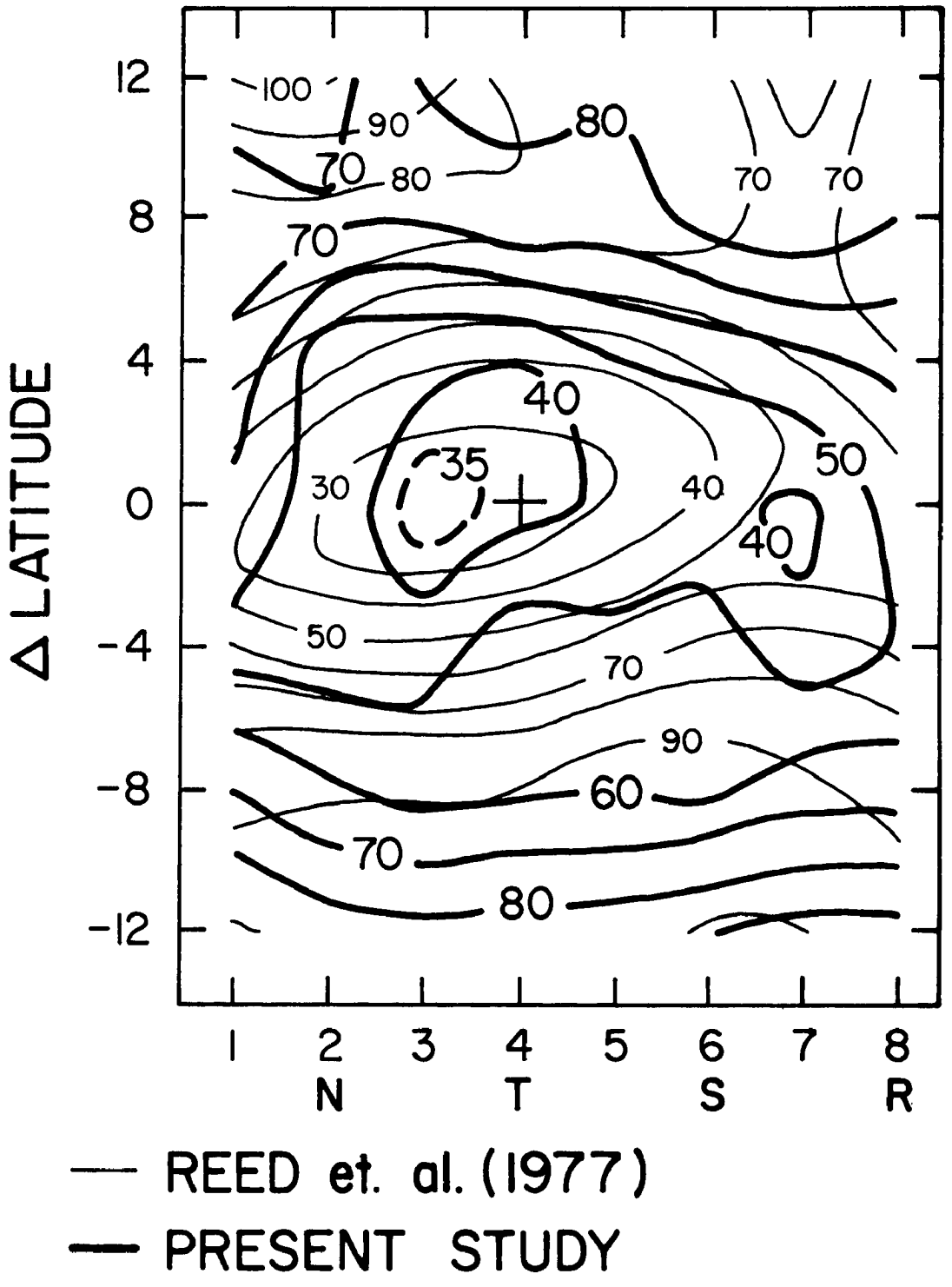

Figure 11. Percentage of clear areas and low clouds as a function of wave position. For explanation of axis labels see Figure 10.

WAVE CATEGORY	CLEAR	900-950	800-900	700-800	600-700	500-600	400-500	300-400	200-300	100-200	NUMBER OF BOXES
1-1	9.0	7.6	28.8	30.5	12.7	7.5	3.9	0.0	0.0	0.0	12
1-2	0.0	.5	34.1	36.4	18.6	9.1	1.4	0.0	0.0	0.0	5
1-3	0.0	0.0	29.5	44.6	12.8	11.1	2.0	0.0	0.0	0.0	6
1-4	0.0	0.0	13.0	56.1	10.6	7.5	12.8	0.0	0.0	0.0	7
1-5	.8	1.5	31.1	36.5	15.5	12.1	2.2	.3	0.0	0.0	10
1-6	47.9	12.3	22.5	6.6	5.8	4.8	0.0	0.0	0.0	0.0	10
1-7	62.7	7.7	12.7	10.1	5.3	1.6	.1	0.0	0.0	0.0	31
1-8	32.9	8.6	26.2	19.9	6.7	3.9	1.9	0.0	0.0	0.0	14
2-1	66.6	8.7	12.2	2.7	3.3	4.2	2.1	.1	.1	.1	127
2-2	42.8	11.8	24.5	9.4	4.4	4.0	2.6	.4	.2	.1	93
2-3	31.1	11.9	28.7	11.3	5.6	5.5	5.6	.0	.1	.2	104
2-4	45.9	10.6	23.4	4.4	5.0	7.0	3.2	.5	.0	0.0	93
2-5	56.9	9.5	8.2	2.4	5.6	9.9	6.5	.8	.2	0.0	79
2-6	68.1	9.3	8.5	4.2	3.6	3.5	1.8	.8	.2	.0	81
2-7	72.3	9.5	7.1	3.6	2.6	3.2	1.4	.4	0.0	0.0	149
2-8	76.8	4.9	8.1	3.9	2.6	2.4	.8	.5	.1	0.0	70
3-1	22.7	10.9	40.7	15.9	4.2	2.3	1.9	1.1	.3	0.0	214
3-2	14.4	9.2	31.3	29.5	6.6	5.2	2.1	1.4	.3	0.0	146
3-3	16.1	5.5	29.7	30.1	8.0	6.5	2.6	.8	.8	0.0	147
3-4	16.6	4.4	23.6	20.5	10.8	10.2	7.1	3.4	2.1	1.4	147
3-5	19.6	6.2	21.6	13.2	9.6	12.2	9.9	5.0	1.8	.8	116
3-6	26.6	8.0	15.5	11.7	9.8	12.4	11.4	4.1	.6	.1	127
3-7	25.1	10.1	23.6	11.6	8.2	7.9	6.2	4.1	2.6	.7	167
3-8	24.6	10.9	31.4	8.9	4.6	4.4	4.1	6.1	4.8	.2	107
4-1	27.6	13.2	19.5	9.8	6.5	6.0	4.3	4.2	4.5	4.5	251
4-2	11.5	13.7	23.3	12.2	7.5	8.3	5.6	5.9	6.9	5.1	193
4-3	10.4	8.3	17.8	11.5	7.8	9.5	6.9	7.4	9.2	11.3	124
4-4	19.9	10.9	15.5	9.2	6.8	7.8	9.2	9.7	7.1	4.0	143
4-5	25.2	11.3	12.0	8.1	6.3	10.0	14.2	8.0	3.6	1.4	98
4-6	25.7	8.7	11.1	8.1	7.2	11.9	15.5	7.1	3.2	1.6	166
4-7	16.6	10.8	13.7	9.0	8.3	13.0	18.0	7.6	1.9	1.2	158
4-8	29.4	13.9	12.3	9.7	7.2	8.7	5.4	4.6	4.1	4.8	157

(Table 1)

WAVE CATEGORY	CLEAR	900-950	800-900	700-800	600-700	500-600	400-500	300-400	200-300	100-200	NUMBER OF BOXES
5-1	21.6	8.5	17.4	12.1	7.6	8.3	7.7	6.9	6.1	3.8	303
5-2	25.5	7.5	12.5	9.0	5.6	7.0	7.5	8.0	10.2	7.2	238
5-3	27.2	7.5	14.4	8.8	6.4	7.9	7.1	6.2	7.5	7.1	162
5-4	42.5	11.0	10.5	7.3	5.9	6.6	4.8	3.8	4.0	3.6	163
5-5	31.6	11.0	12.6	8.2	7.9	12.4	8.1	5.1	1.9	1.2	117
5-6	37.0	10.1	11.5	8.5	6.2	9.3	9.4	4.3	3.3	.4	192
5-7	25.8	8.7	12.2	10.8	8.6	11.7	12.9	4.5	3.9	1.1	166
5-8	20.2	15.5	14.6	10.8	7.4	7.8	8.4	6.3	5.2	3.9	172
6-1	39.4	13.5	16.8	8.9	4.8	5.9	4.4	3.1	2.5	.7	287
6-2	27.7	13.7	19.9	11.1	6.2	9.5	6.3	3.1	1.9	.7	247
6-3	27.0	12.9	14.7	9.3	6.9	10.2	10.8	3.1	3.8	1.2	160
6-4	29.2	14.0	16.0	11.1	7.2	8.7	6.9	3.3	2.0	1.6	176
6-5	32.4	12.9	14.9	9.2	8.1	10.0	7.3	2.8	1.8	.6	148
6-6	27.1	10.8	18.8	11.8	7.7	7.5	7.6	4.8	3.5	.4	164
6-7	33.2	13.1	20.3	11.4	5.2	5.4	3.1	3.2	3.7	1.3	196
6-8	34.3	14.0	17.4	9.0	6.1	7.2	5.3	3.1	2.6	1.0	198
7-1	45.1	29.5	17.5	3.8	1.3	1.1	.9	.3	.4	.1	248
7-2	42.6	26.4	15.7	5.9	3.2	2.6	1.7	1.7	.2	.0	216
7-3	46.9	23.4	12.2	5.4	3.6	3.7	3.4	.6	.5	.1	129
7-4	50.7	21.2	13.6	5.9	3.8	2.6	1.1	.7	.3	.1	168
7-5	48.8	21.6	14.8	6.8	3.2	2.1	.5	.7	1.0	.4	141
7-6	47.4	28.2	14.7	4.5	2.1	1.6	.6	.3	.4	.2	135
7-7	52.2	21.3	20.7	3.4	.5	.5	.4	.2	.4	.3	200
7-8	41.1	25.5	27.0	3.4	1.1	.9	.5	.3	.3	.0	179

Table 1. 24 hour mean cloud top distribution as a function of wave position. Column 1 is the wave category or position. The first number corresponds to the row, the second represents the wave column. Columns 2-19 represent the areal percent coverage of cloud tops between the pressure intervals listed at the head of the column. The last column lists the number of 1° boxes that comprised the wave category composite.

images would depict these low- and middle-level clouds as dark gray areas, thus, by the method used by Reed, categorizing them in Category 0.

Table 1 presents the average percentage area covered by clouds with tops in a given height regime for each composite category over the ocean area. Column 1 is the wave category or position. The first number corresponds to the row (Δ latitude 0 is row 4), the second represents the column. Thus wave category 4-4 corresponds to Δ latitude 0 at the trough position. Columns 2-19 represent the areal percent coverage of cloud tops between the corresponding pressure intervals listed at the head of the column. The last column lists the number of 1° boxes that comprise the wave category composite. Note the small number of 1° squares that represent the first row of the wave. Row 1 (Δ latitude + 12) was usually above 22°N latitude, which is the northern limit of the SMS-1 brightness data used in this study.

Table 1 and Figures 10 and 11 reveal latitudinal and longitudinal variations in cloud cover as a function of pressure. To examine the latitudinal variations, mean cloud top distributions for four pressure levels, 1) clear (cloud top $\leq$ 950 mb), 2) low cloud tops (950 mb < CT $\leq$ 700 mb, 3) middle cloud tops (700 mb < CT < 400 mb) and 4) high cloud tops (CT > 400 mb), are composited latitudinally for four regions; 1) Δ latitude 12, 2) the region north of the ITCZ (Δ latitude 8 and 4), 3) the ITCZ region (Δ latitude 0 and -4) and 4) the region south of the ITCZ (Δ latitude -8 and -12). The mean cloud cover as a function of pressure and associated standard deviations are computed from 1° x 1° box cloud top mean distributions, thus allowing a large sample size (approximately 10,000 1° boxes). The mean cloud amounts and standard

deviations are given in Table 2. The standard deviations represent the variability of the 17 cases as well as the E-W differences.

From Table 2 one notes the symmetry in cloud distribution about the ITCZ region. This table also shows the small diurnal variability in the cloud top distribution. This small diurnal difference is a result of the 12 h averaging period. Diurnal variations will be discussed in the next section.

Longitudinal variations were investigated in a similar manner using the four latitudinal regions and four cloud top pressure levels. However, rather than averaging over all eight wave columns, the wave is divided into a ridge position (columns 2, 3, 4 and 5) and a trough position (columns 1, 6, 7 and 8). The mean cloud cover and standard deviations are given in Table 3. The largest diurnal difference in the ridge section of the wave occurs in the ITCZ region, whereas the maximum diurnal difference in the trough position occurs to the south of the ITCZ.

From Tables 1, 2 and 3, one notes that Row 1, or Δ latitude +12 is comprised of middle- and low-level clouds, leading one to suspect some thin cirrus contamination. Analysis of each individual hour reveals that Julian Day 246, hours 0600, 1200 and 1800 and Julian Day 247, hours 0000 and 0600 GMT contribute most of the boxes in Row 1. The SMS-1 visible images reveal clouds in the area of question. If thin low emittance cirrus were in the area, this region would appear as dark gray or black areas in the visible spectrum of the satellite. Analysis of the visible satellite images for the remaining hours reveals that low- and middle-level clouds in Row 1 are typical. One also notes that Rows 1 and 2 (average latitudes of 24°N and 20°N respectively)

		CLEAR CT < 950 mb	LOW CLOUD TOP 950 mb < CT ≤ 700 mb	MIDDLE CLOUD TOP 700 mb < CT ≤ 400 mb	HIGH CLOUD TOP CT > 400 mb
Δ latitude + 12	Mean	29.28	52.75	17.94	.03
	S.D.	29.26	43.24	14.27	.14
Region north of the ITCZ	Mean	34.42	44.41	17.48	3.69
	S.D.	21.73	19.34	7.76	5.37
ITCZ	Mean	25.11	34.07	24.78	16.04
	S.D.	18.19	11.03	9.49	9.02
Region south of the ITCZ	Mean	36.20	42.17	15.54	6.10
	S.D.	21.07	14.55	6.76	4.88

Table 2a. Day and night cloud top distributions. Latitudinal mean percentage of cloud top (CT) areal coverage and standard deviations (S.D.) at four pressure levels for four regions of the wave composite.

		CLEAR CT < 950 mb	LOW CLOUD TOP 950 mb < CT ≤ 700 mb	MIDDLE CLOUD TOP 700 mb < CT ≤ 400 mb	HIGH CLOUD TOP CT > 400 mb
Δ latitude + 12	Mean	43.77	48.68	7.55	0
	S.D.	46.16	71.51	23.19	.2
Region north of the ITCZ	Mean	35.6	48.81	15.11	3.49
	S.D.	24.27	21.79	7.91	4.7
ITCZ	Mean	26.42	36.51	23.25	13.82
	S.D.	18.38	12.01	9.54	8.05
Region south of the ITCZ	Mean	38.51	41.95	13.54	6.01
	S.D.	23.94	15.84	5.63	4.75

Table 2b. Day cloud top distribution. Latitudinal mean percentage of cloud top (CT) areal coverage and standard deviations (S.D.) at four pressure levels for four regions of the wave composite.

		CLEAR CT < 950 mb	LOW CLOUD TOP 950 mb < CT ≤ 700 mb	MIDDLE CLOUD TOP 700 mb < CT ≤ 400 mb	HIGH CLOUD TOP CT > 400 mb
Δ latitude + 12	Mean	20.83	55.12	24.00	.05
	S.D.	37.25	54.28	17.92	.16
Region north of the ITCZ	Mean	33.21	42.96	19.93	3.90
	S.D.	25.66	20.74	8.78	6.16
ITCZ	Mean	23.74	31.51	26.39	18.36
	S.D.	20.04	12.32	10.68	10.5
Region south of the ITCZ	Mean	33.74	42.40	17.66	6.19
	S.D.	21.54	16.29	8.41	5.23

Table 2c. Night cloud top distribution. Latitudinal mean percentage of cloud top (CT) areal coverage and standard deviations (S.D.) at four pressure levels for four regions of the wave composite.

		CLEAR CT < 950 mb		LOW CLOUD TOP 950 mb < CT ≤ 700 mb		MIDDLE CLOUD TOP 700 mb < CT ≤ 400 mb		HIGH CLOUD TOP CT > 400 mb	
		R	T	R	T	R	T	R	T
Δ latitude + 12	MEAN	41.39	.29	45.70	69.61	12.90	30.00	0.0	.10
	S.D.	34.84	.71	27.62	67.23	8.73	22.55	0.0	.26
Region north of the ITCZ	MEAN	41.08	26.81	39.83	49.63	15.25	20.04	3.85	3.52
	S.D.	23.27	19.81	18.39	20.38	6.73	8.79	6.16	4.31
ITCZ REGION	MEAN	26.27	23.63	34.34	33.71	26.69	22.35	12.70	20.31
	S.D.	19.05	17.01	11.11	10.94	10.41	8.16	8.01	10.17
Region south of the ITCZ	MEAN	37.01	35.24	43.63	40.45	13.22	18.26	6.15	6.04
	S.D.	21.71	20.29	15.66	13.12	5.75	7.78	4.85	4.91

DAY and NIGHT cloud top distributions for the ridge and trough regions.

Table 3a. Ridge (R) and trough (T) mean percentage of cloud top (CT) areal coverage and standard deviations (SD) at four pressure levels for four regions of the wave.

		CLEAR CT < 950 mb		LOW CLOUD TOPS 950 mb < CT ≤ 700 mb		MIDDLE CLOUD TOPS 700 mb < CT ≤ 400 mb		HIGH CLOUD TOPS CT > 400 mb	
		R	T	R	T	R	T	R	T
Δ latitude + 12	MEAN	63.83	0.00	31.08	87.09	5.09	12.91	0.0	0.00
	S.D.	55.75	.96	46.46	107.53	14.07	35.77	0.0	.35
Region north of the ITCZ	MEAN	45.32	26.31	39.74	51.60	11.77	18.29	3.16	3.80
	S.D.	27.88	20.23	21.68	21.89	6.92	8.76	5.57	3.68
ITCZ Region	MEAN	26.94	25.81	40.22	32.09	24.41	21.88	8.44	20.22
	S.D.	18.13	18.63	13.13	10.53	10.94	7.53	5.56	10.24
Region south of the ITCZ	MEAN	37.68	39.56	43.48	40.00	12.06	15.41	6.78	5.03
	S.D.	22.99	25.12	16.47	15.01	4.81	6.52	4.96	4.45

DAY cloud top distributions for the ridge and trough regions.

Table 3b. Ridge (R) and trough (T) mean percentage of cloud top (CT) areal coverage and standard deviations (SD) at four pressure levels for four regions of the wave.

		CLEAR CT < 950 mb		LOW CLOUD TOP 950 mb < CT ≤ 700 mb		MIDDLE CLOUD TOP 700 mb < CT ≤ 400 mb		HIGH CLOUD TOP CT > 400 mb	
		R	T	R	T	R	T	R	T
Δ latitude + 12	MEAN	28.87	.48	53.87	58.30	17.26	41.05	0.00	.17
	S.D.	44.00	.84	34.38	86.09	11.03	28.74	0.00	.31
Region north of the ITCZ	MEAN	37.41	27.44	39.90	47.17	18.26	22.22	4.44	3.17
	S.D.	26.66	24.22	18.13	23.88	7.52	10.27	6.79	5.17
ITCZ Region	MEAN	25.63	21.13	28.58	35.58	28.92	22.89	16.88	20.41
	S.D.	21.52	17.80	11.04	13.90	11.09	10.08	10.13	10.99
Region south of the ITCZ	MEAN	36.24	31.06	43.80	40.89	14.54	21.02	5.42	7.02
	S.D.	23.91	18.67	17.83	14.47	7.20	9.54	4.95	5.51

NIGHT cloud top distributions for the ridge and trough regions

Table 3c. Ridge (R) and trough (T) mean percentage of cloud top (CT) areal coverage and standard deviations (SD) at four pressure levels for four regions of the wave.

occupy regions of persistent active marine stratocumulus convection (Schubert et al. 1977). Carlson and Prospero (1972) have noted a discontinuity in cloudiness at the leading edge of a Saharan dust outbreak. This pattern of stratocumulus cells to the west of the leading edge of the dust outbreak (Rows 2, 3, 4 and 5) and smooth, small-celled stratocumulus and clear regions to the east (Rows 1, 6, 7 and 8) is apparent in the cloud top distribution (Table 1 and Table 3).

As a final test to determine the quality of the data, 1° boxes were composited around the B array for the 17 individual hours and cloud top distributions were compared with the results of Cox and Griffith (1979b). The comparison was acceptable in all but a few cases. Differences may be attributed to two factors: 1) the two methods did not derive cloud top distribution for the exact same area and 2) the two methods used different temperature profiles, and different moisture profiles. It is important to note that the specific humidity profiles reported by Reed et al. (1977) and used in the present study were composited from both ocean and land stations and tend to be less than the total precipitable water calculated by Cox and Griffith (1979a). Consequently, this study will slightly underestimate the water vapor correction term previously discussed resulting in cloud top location errors. This error predominates in the clear and low-level cloud regions, in the Δ latitude +12 and +8 regions of the wave.

4.1.1 Comparison of Cloud Cover Estimates

Four U.S. ships were equipped with whole sky cameras during GATE. Holle et al. (1979) (HSL) analyzed the 617,280 panoramic photographs and derived cloud cover amounts for each day of the experiment. They

went on to display phase averages of high, low and total cloudiness. In the present study cloud cover amounts were generated from SMS-1 satellite data in a manner described by Cox and Griffith (1979). From the phase average cloud amounts derived in HSL and Cox and Griffith (1978) it is possible to compare two different techniques (i.e. ground and satellite based observations) for determining cloud amounts. Figure 12 shows the contoured phase-average total cloud cover amount maps derived as a by-product from the radiative divergence profiles produced by Cox and Griffith (1978). The left-hand portions of the figure are reproductions of the maps produced by HSL and are shown for ease of comparison. The area that we show in the right-hand portion of the figure was scanned by the satellite-borne radiometer and is obviously larger in areal extent that the HSL maps. It is plain to see that the satellite data provide more information in terms of gradients and contours than the smaller area mapped by HSL which is shown as a box in the Cox and Griffith analysis. HSL use data only from the four ships shown in the figure and subjectively interpolate between them to produce their contours. The satellite data grid has many more point sources, 225 in all, and consequently contouring can be performed much more reliably.

Agreement between the two techniques is expected in comparing total cloudiness since each cloud base has a cloud top and vice versa. Differences between the techniques should be a result of the different spatial and temporal resolutions as well as the "cloud-no cloud" defnition. The agreement during Phase I between the data provided by the two platforms is quite striking. However, agreement in Phase II is not quite as good. Although the total cloud cover determined in the

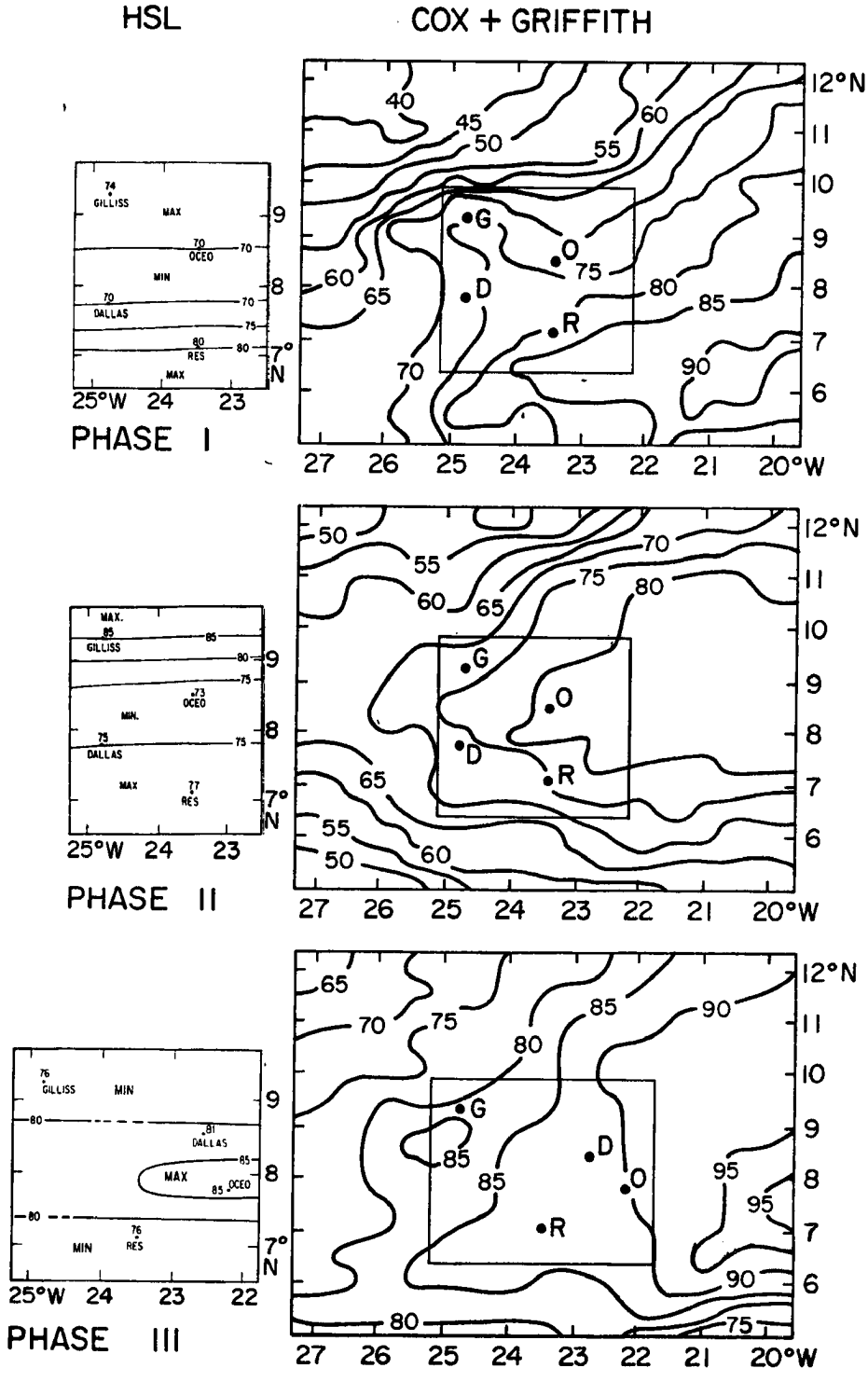

Figure 12. A comparison of total cloud amount (%) during each phase of GATE derived from HSL and Cox and Griffith (1978).

vicinity of the Dallas and the Researcher for the two data sets agrees well, the disagreement between the Oceanographer and Gillis cloud cover results in a relative minimum in the HSL analysis where there is a relative maximum in the Cox and Griffith data. Phase III spatial gradients in total cloud cover agree in the two studies, with the absolute values of total cloudiness being consistently larger by 5 - 10% in the Cox and Griffith data set.

HSL vertically stratified the clouds as low, middle or high depending on the cloud base location. Observations from the top of the atmosphere classify low middle or high cloud as a function of cloud top. Figure 13 presents a comparison between the maps produced from the two data sources for Phase III. The top portion of the figure shows the maps for the clouds that Cox and Griffith characterize as low, the lower portion shows the "high" clouds. Becuase of obscuration of low clouds by higher clouds one would expect the amount of low clouds deduced from satellite data to be less.than the low cloud amounts generated from surface observations. In the case of the high cloud classification the satellite determined amounts hould be larger than that of the ground based platform. Figure 13 agrees with these expectations.

Comparisons of the HSL and Cox and Griffith data sets indicate that ground and satellite based observations give similar estimates of total daytime cloud amount. However, the vertical stratification of the total cloud amount to low middle and high clouds results in two different, yet dependent, data samples, thereby limiting any intercomparisons. The different method of vertical stratification has the

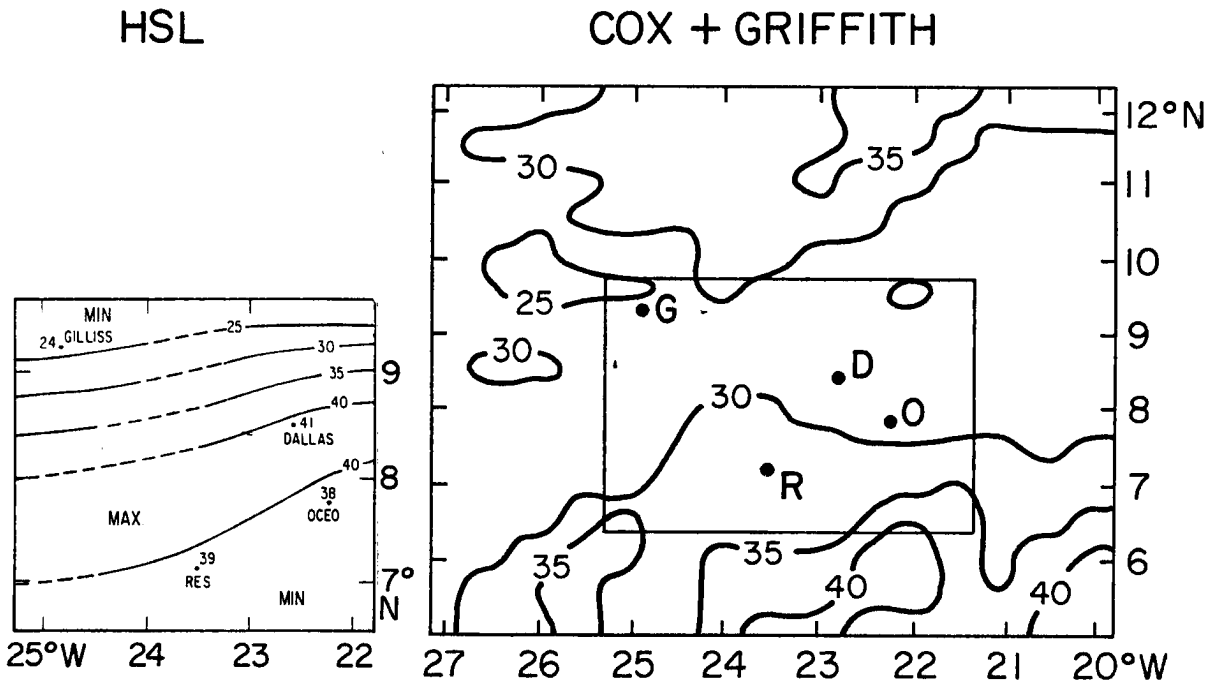

A. LOW CLOUD AMOUNT (%)

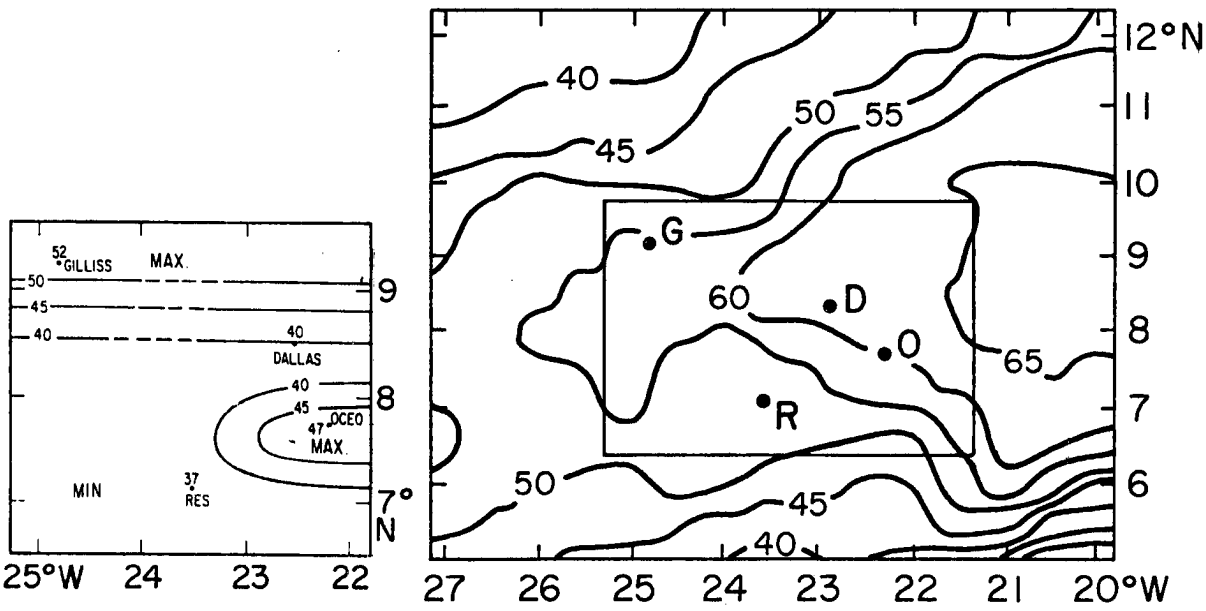

B. HIGH CLOUD AMOUNT (%)

Figure 13. GATE Phase III low and high cloud amounts (%) for 0600 - 1800 GMT.

advantage of enabling one to estimate cloud structure as is discussed in Section 2.2.

One obvious limitation of using all-sky camera photography to assess cloud cover amounts is that between dusk and dawn no data are collected. For this reason the foregoing comparisons have been restricted to the daytime hours i.e. 0600 - 1800 GMT. Cox and Griffith (1978) and this study use infrared satellite data to generate cloud cover information, consequently daily (24 hour) cloud cover amounts can be calculated and the diurnal variability in cloudiness can be monitored.

Figure 14 shows the mean nighttime (1800 - 0600 GMT) total cloud cover amounts for Phase III of the GATE derived from the Cox and Griffith data set and the complementary daytime map. The figure shows that in the mean the Phase III total cloud cover for the A/B array is greater during the nighttime period, and that the horizontal gradients are slightly less at night. As a result of the small difference between the daytime and the nighttime cloud cover, the effect of including the latter in determining a 24 hour time average composite over the GATE region appears to be small. In this study, cloud amounts are composited with respect to an easterly wave. This type of compositing scheme differs from the "geographical" scheme in that it tends to separate convectively active and suppressed regions. The diurnal variability of the cloud cover embedded in this synoptic scale feature is discussed in the following section.

4.1.2 Diurnal Variation of Cloud Top Amount

The diurnal variability of the tropical atmosphere is well documented (Ruprecht and Gray, 1976b; Foltz, 1976; Gruber, 1976; Gray and

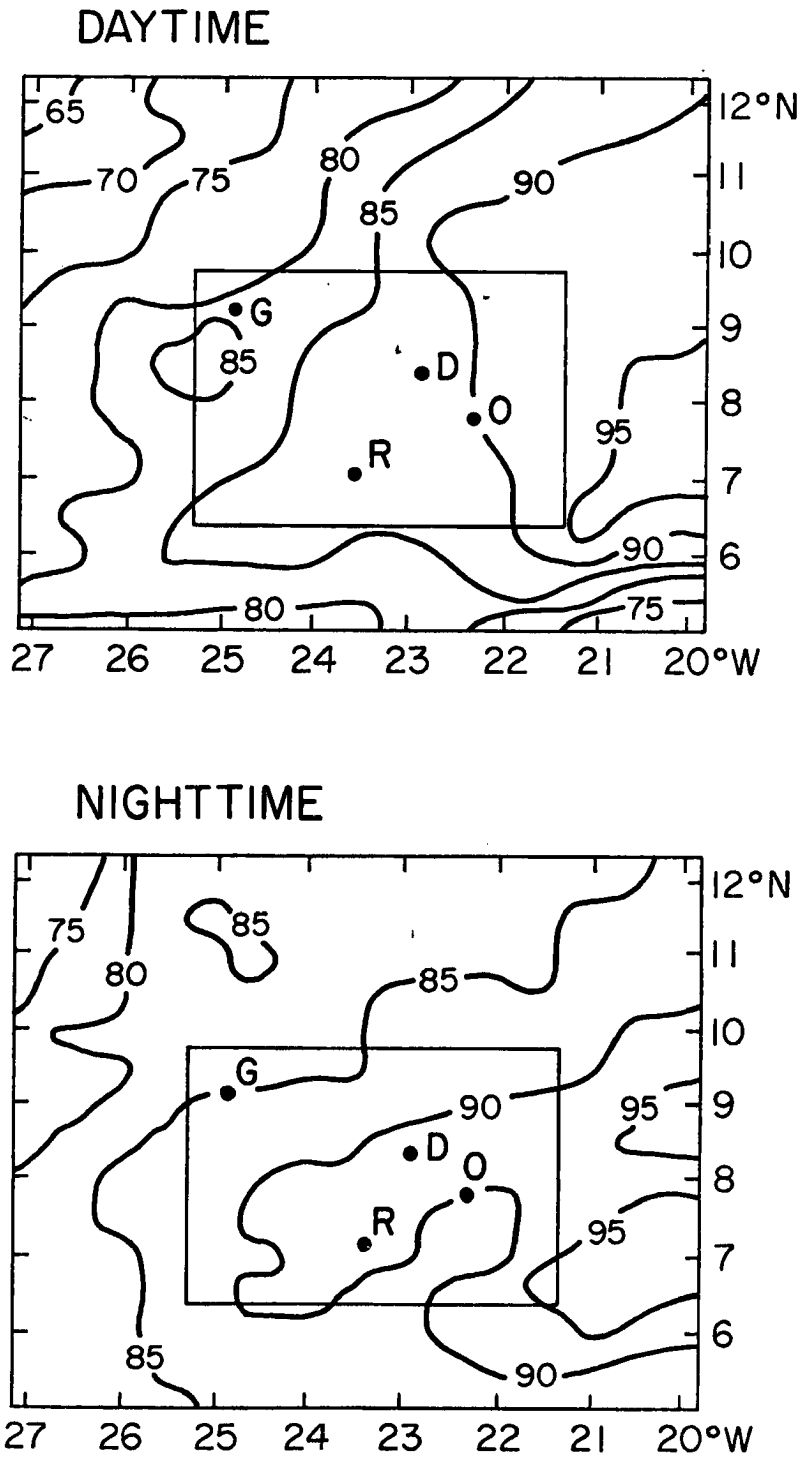

Figure 14. Daytime (0600 - 1800 GMT) and nighttime (1800 - 0600 GMT) mean total cloud cover.

Jacobson, 1977; McGarry and Reed, 1978). An understanding of this diurnal variability is an important step in comprehending the dynamic-radiative interaction and feedback mechanisms of the tropical atmosphere. The results of the present study allow us to investigate the synoptic scale diurnal variability in areal cloud amounts as a function of pressure. To obtain the diurnal difference, the mean cloud top distribution at 0000 and 0600 GMT is assumed to be representative of the mean nocturnal cloudiness. Daytime cloud distributions are represented by the 1200 and 1800 GMT mean distributions. To validate these assumptions, the resulting mean distributions were compared to the results of Smith and Vonder Haar (1976). Smith and Vonder Haar have studied the diurnal variability of cloud cover percentage for different sectors of the A array for the three phases of GATE. A comparison of their mean nighttime (daytime) Phase III cloudiness with the 0000 GMT and 0600 GMT (1200 GMT and 1800 GMT) mean revealed that in most cases both upper and lower cloud amounts differed by less than $\pm$ 5%.

Figure 15 is the percent difference, as a function of wave position, between the mean daytime and the mean nighttime clear regions. The shaded regions represent areas where the nighttime values are greater than the daytime values. Hence, unshaded regions represent regions of maximum nighttime total cloudiness. Remembering the few boxes that comprised Row 1 (Δ latitude + 12), one should be cautious in drawing conclusions about cloud distribution differences from this row. One first notes that cloud cover is generally slightly greater during the night. This agrees with the results of Smith and Vonder Haar (1976). Cox and Griffith (1979a,b) (CG) showed that the GATE Phase III mean percent areal coverage of clear regions is only

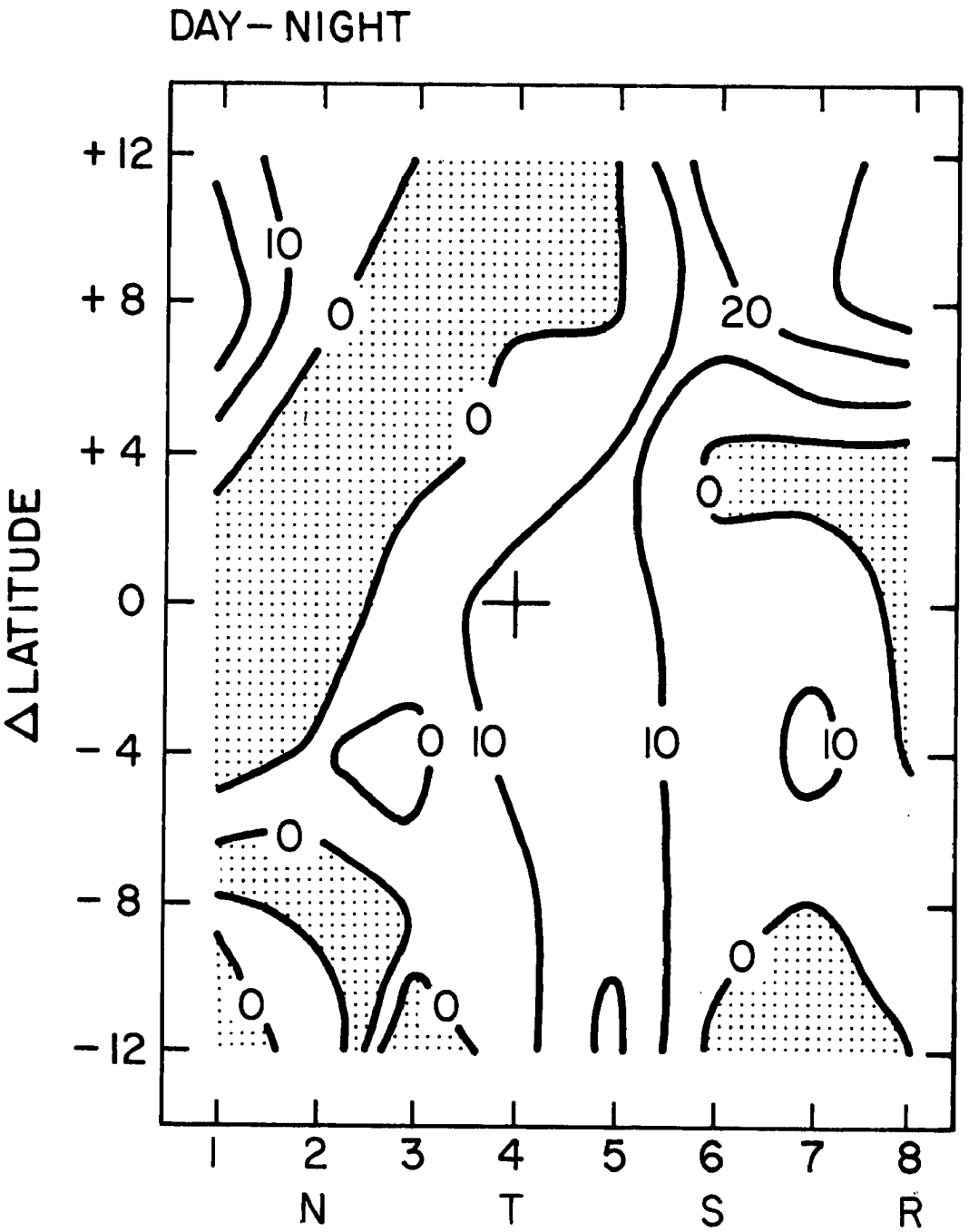

Figure 15. Percent difference between mean daytime and mean nighttime clear regions. Shaded areas represent regions of larger nighttime clear regions. For explanation of axes see Figure 10.

slightly larger during the day (0600 to 1800 LST) than during the night (1800 to 0600 LST). When broken down into 6 hour intervals, minimum cloudiness occurred between 0600 and 1200 LST (0730 to 1300 GMT). Maximum cloud cover occurred during the time interval 1200 to 2400 LST (1330 to 0130 GMT). Gruber (1976) found a small 12 hour nighttime maximum in total cloudiness for the A/B region for the three phases of GATE. When total cloudiness in divided into convectively enhanced and suppressed cases, Gruber finds that nighttime maximum is primarily a result of a nighttime maximum in the convectively suppressed cases. Largest differences in cloudiness in the present study are near the region of minimum convective activity.

Figure 16 is the percent difference, as a function of wave position, between the mean daytime and the mean nighttime areal coverage of cloud tops between 100 and 300 mb. Again, the shaded regions represent areas where the nighttime distributions are greater than the daytime distributions. The differences are small north and south of the ITCZ regime (Δ latitude 0 and -4). In the ITCZ regime we note that the 100 - 300 mb cloud cover is slightly larger at night in columns 6, 7 and 8, the dynamically unfavorable convective regimes. It is possible that in these regions of the wave the smaller daytime coverage is a result of the SW absorption in the clouds. Gruber (1976) and McGarry and Reed (1977) conclude that convective cloudiness in the A/B array is greatest in the late afternoon. Inspection of the daytime and nighttime 100 - 300 mb cloud cover separately, reveals that both periods have a maximum W-SW of the wave center (Δ latitude 0 at the trough position), the daytime value being larger. However, during the night this maximum tends to be elongated east-west. This stretching

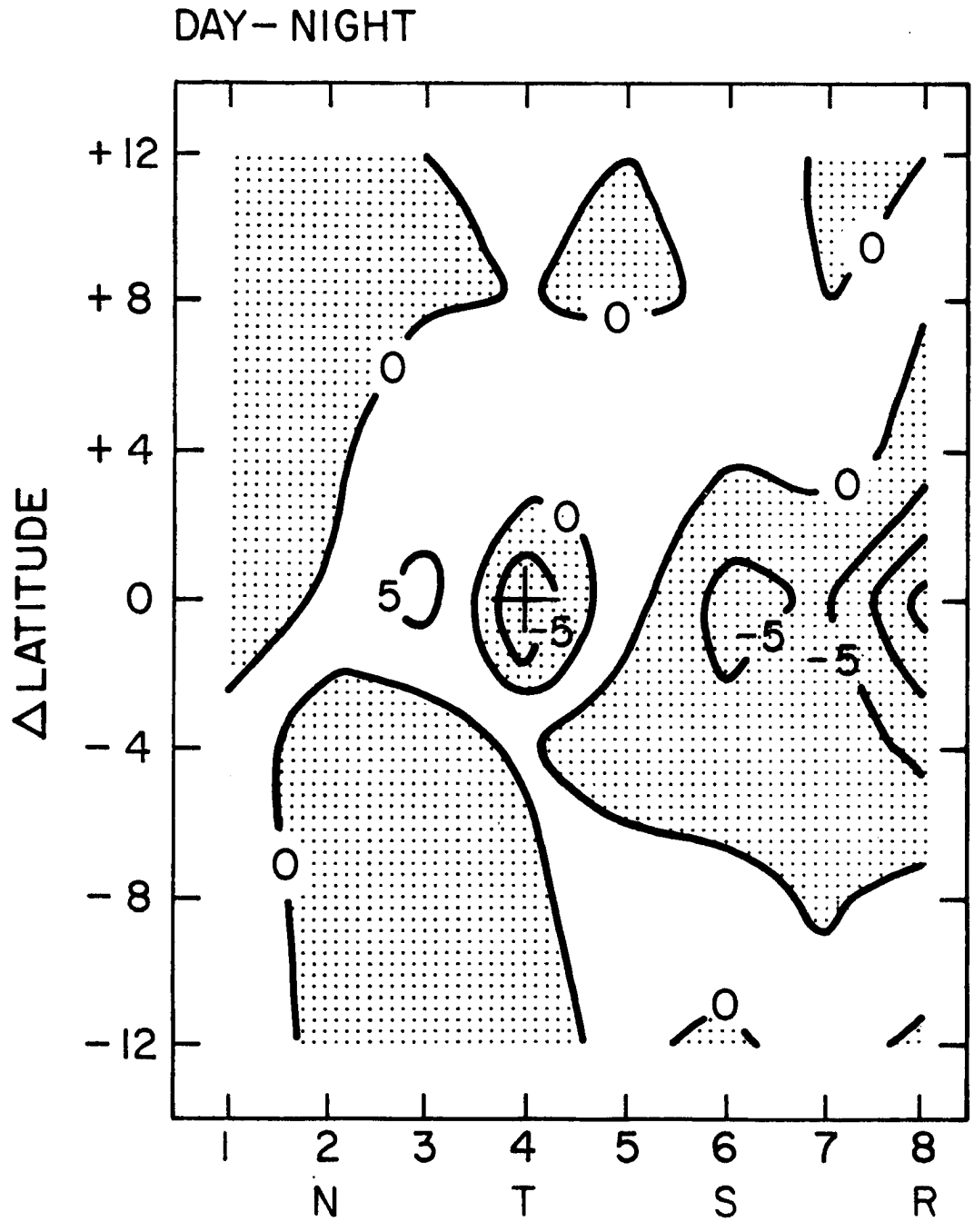

Figure 16. Percent difference between mean daytime and mean nighttime 100-300 mb cloud tops. Shaded areas represent regions of larger nighttime values. For explanation of axes see Figure 10.

does not occur in the day composite and results in a greater nighttime value at the wave center. The possibility exists that there is a north-south forcing which results in the nighttime east-west elongation of the high clouds, as well as the nighttime maximum in the non-convective regions of the wave.

A large area diurnal variability appears at 300, 400, and 500 mb, the largest difference occurs between 500 and 400 mb. The day-night difference in the 300-600 mb cloud tops is depicted in Figure 17. The differences at these levels appears largest in the regions of the wave that are dynamically unfavorable for convection (Reed et al. 1977).

Descending through the atmosphere to 900 mb, the daytime cloudiness tends to progressively become greater than the mean cloudiness observed at night. However, this may be an artifact of the increased higher level cloud cover during the night, obscuring the low-level tops from the satellite view.

4.2 Tropospheric Radiative Convergence Profiles

This section discusses the radiative convergence profiles resulting from the nighttime and daytime cloud top distributions. Comparisons between the day and night profiles are made where appropriate. Negative energy fluxes represent an energy loss (divergence), positive energy fluxes represent an energy gain (convergence). The derived radiative profiles are listed in Appendix B. The figures presented in this section are shown to demonstrate heating gradients, numerical values should not be interpolated from these figures.

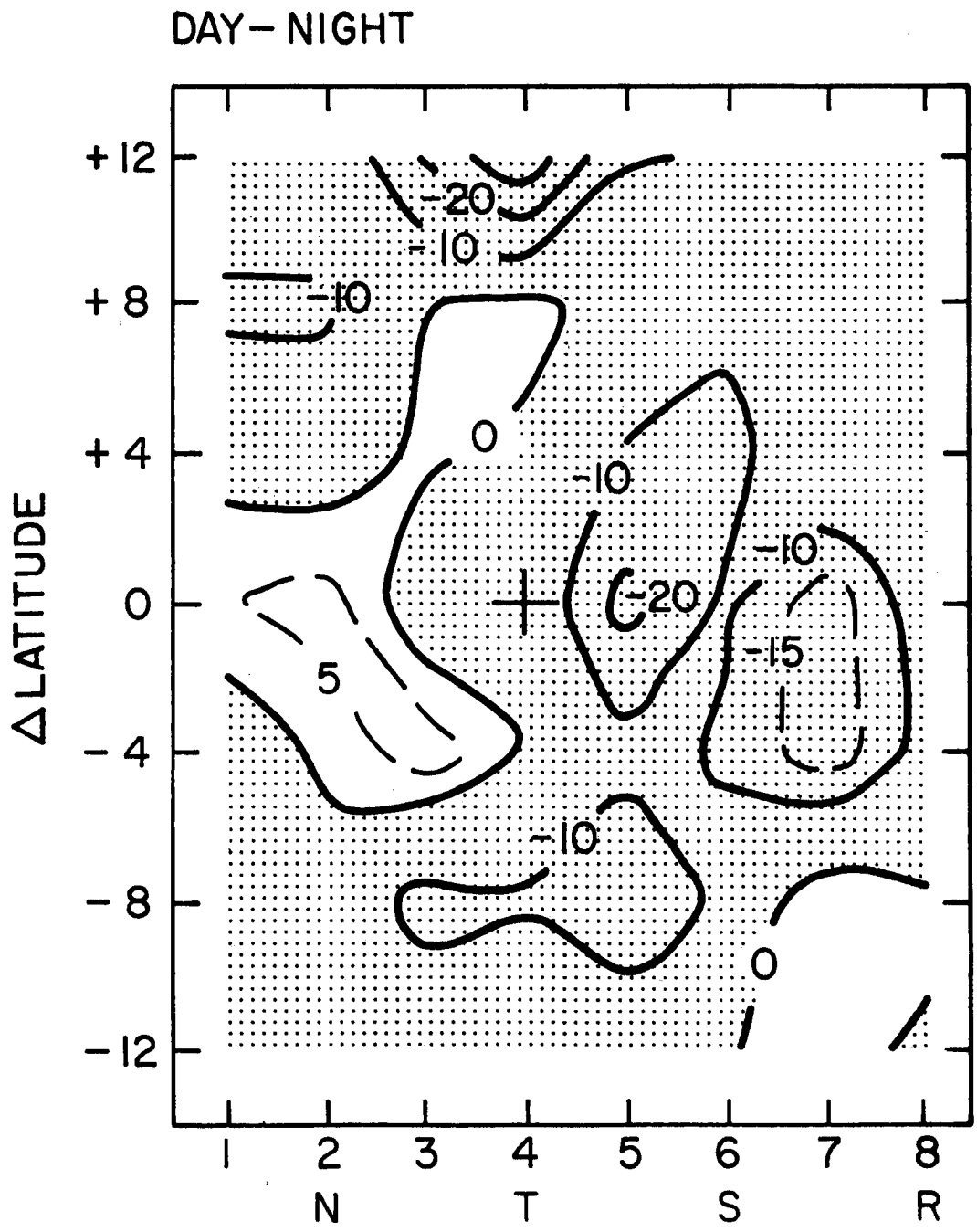

Figure 17. Percent difference between mean daytime and mean nighttime 300-600 mb cloud tops. Shaded areas represent regions of larger nighttime values. For explanation of axes see Figure 10.

4.2.1 Nighttime Profiles

Figure 18 is a plot of total tropospheric convergence (TTC) as a function of wave position for the night cloud distribution. There appears to be a small zonal gradient in TTC in agreement with the derived cloud top distribution. A north-south gradient is evident. A mean spacial and temporal gradient of approximately 32 W m^{-2} (912 mb)$^{-1}$ ($\sim$ .3°C/day) exists between the center of the disturbance path and approximately 4° north of the disturbance path. The meridional gradient south of the disturbance path is less, 19 W m^{-2} ($\sim$ .19°C/day) between Δ latitude +4 and Δ latitude +12. Figure 19 is a plot of the IR component of total tropospheric convergence assuming that no clouds were present. Comparison of Figures 18 and 19 reveals that the cloud distribution suppresses radiative cooling at the ITCZ region (Δ latitude 0 and -4) while enhancing the cooling north and south of the ITCZ. The large decrease in TTC in Δ latitudes +12 and +8 is a result of the large amounts of low level clouds, and the dry, warm air above 900 mb. The magnitude of the suppression and enhancement of TTC due to the presence of the clouds is large enough to reverse the meridional gradient.

A large lower tropospheric gradient exists between Δ latitude 0 and -4 (ITCZ) and north of the disturbance center. A smaller lower tropospheric heating gradient exists between Δ latitudes 0 and -4 and the more southerly rows. This type of heating gradient could possibly induce low level pressure gradients that result in convergence into the ITCZ. Figure 20 is a plot of the radiative convergence for the easterly wave night composite between 1000 and 700 mb, units are W m^{-2} (300 mb)$^{-1}$. A mean gradient of 41 W m^{-2} (300 mb)$^{-1}$ ($\sim$ 1.2°C/day)

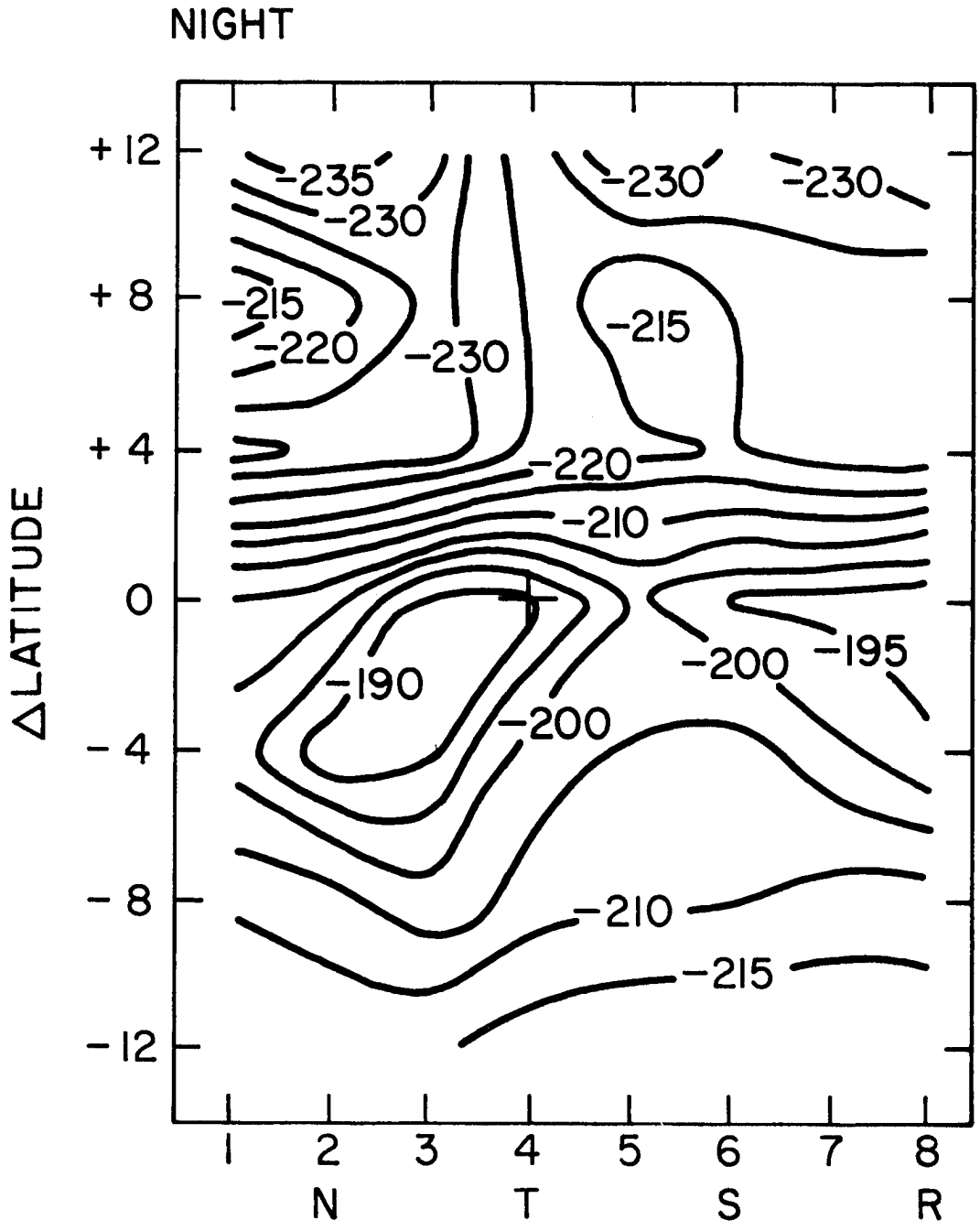

Figure 18. Total tropospheric convergence as a function of wave position for the night cloud distribution. For explanation of axes see Figure 10. Values are in W m^{-2} (912 mb)$^{-1}$.

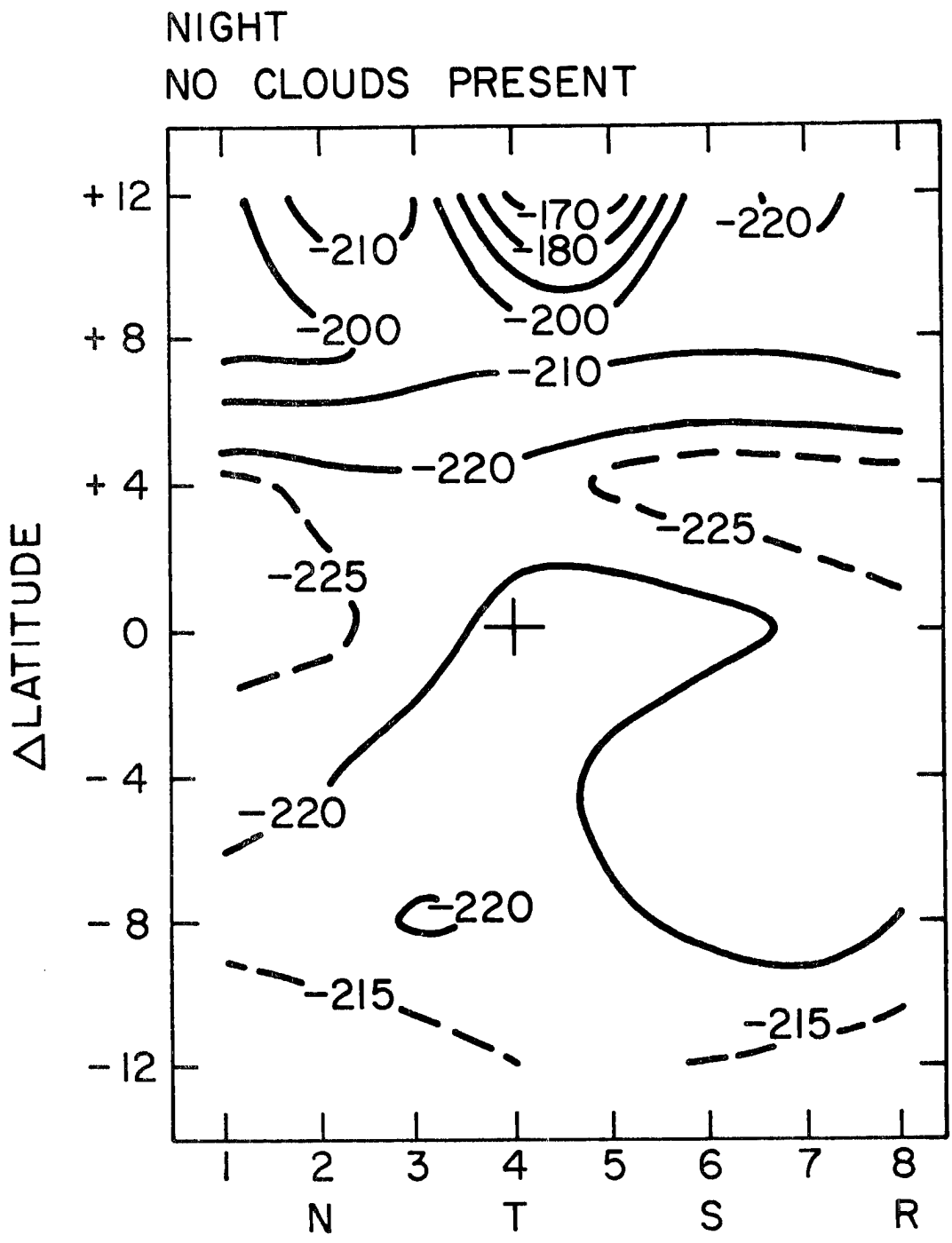

Figure 19. IR component of total tropospheric convergence assuming that no clouds are present. For explanation of axes see Figure 10. Values are in W m^{-2} (912 mb)$^{-1}$.

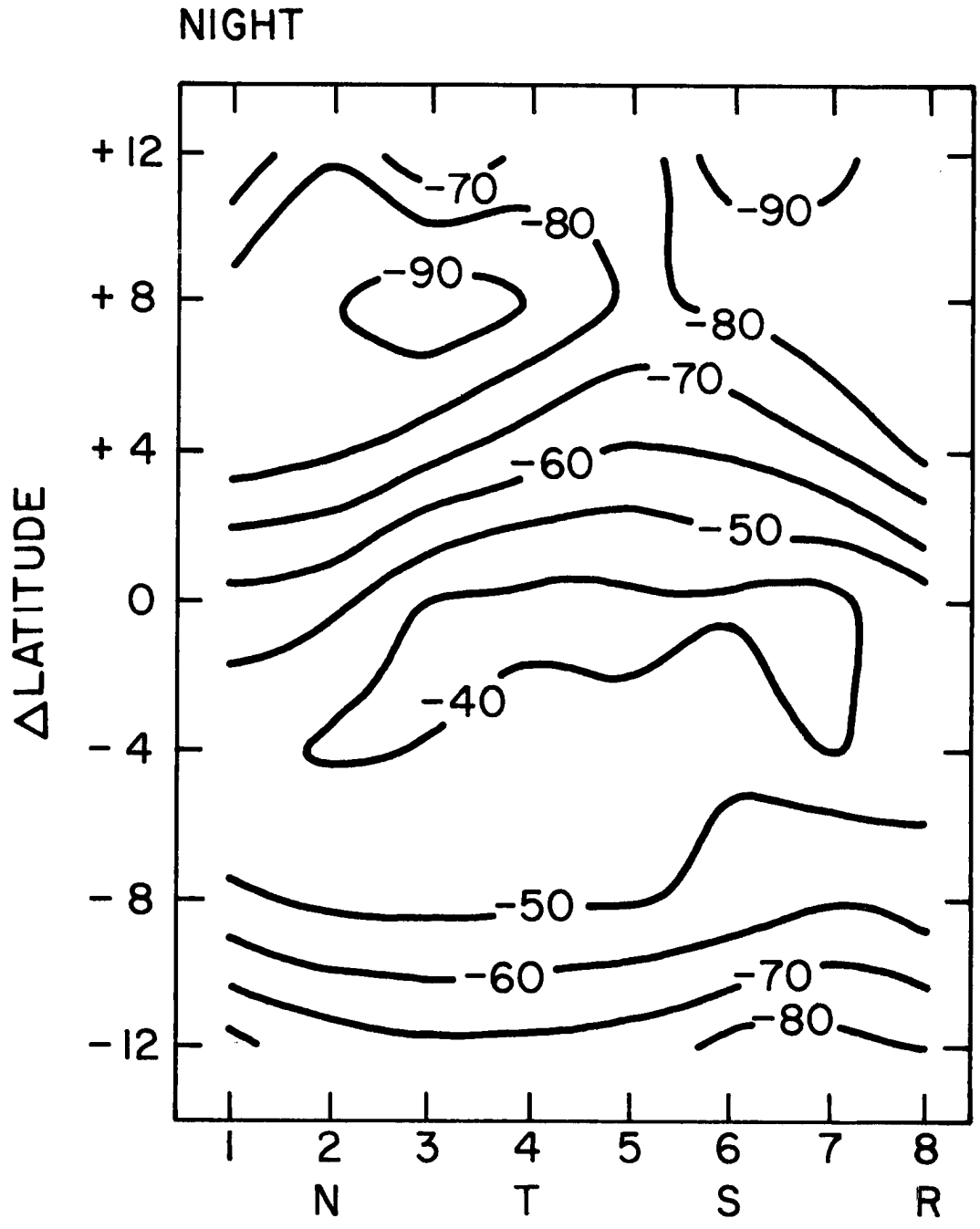

Figure 20. Radiative convergence for the 100-700 mb layer using nighttime cloud distributions. For explanation of axes see Figure 10. Values are in W m^{-2} $(300\ mb)^{-1}$.

exists between the reference latitude and Δ latitude +4. A much smaller gradient of 24 W m^{-2} (300 mb)$^{-1}$ (∿ .7°C/day) exists between Δ latitude -4 and Δ latitude -8. The larger difference to the north (Δ latitude +8 and +12) of the ITCZ is a result of the stratocumulus cloud distribution and the associated warm, dry air of the region. Figure 21 shows the radiative convergence gradient for the 400 - 100 mb layer. The maximum cooling east of the trough is a direct result of the cloud top distribution, and may interact with the wave dynamics as discussed in Section 4.4.

4.2.2 Daytime Profiles

A plot of TTC for day cloud distributions, Figure 22, shows a meridional gradient and a small zonal gradient in TTC. The meridional TTC gradient for the daylight hours is less than the night gradient. The mean spacial and temporal gradient between Δ latitude 0 and Δ latitude +4 is only 20.6 W m^{-2} (912 mb)$^{-1}$ (∿ .2°C/day). As in the night composite, the presence of clouds enhances the cooling north and south of the ITCZ regime and suppresses the cooling at the ITCZ. The affect of the cloud distribution is to reverse the meridional gradient of TTC, which can be seen by comparing Figures 22 and 23. The induced heating gradients between 1000 - 700 mb, Figure 24, are approximately half the nighttime composite values. These heating gradients, excluding all other possible interactions, will induce a pressure gradient resulting in convergence into the ITCZ region. The heating gradients between 100 - 400 mb, Figure 25, are essentially zero.

Outbreaks of Saharan dust affect the radiation budgets of the atmosphere depending on the concentration, size spectra, chemical

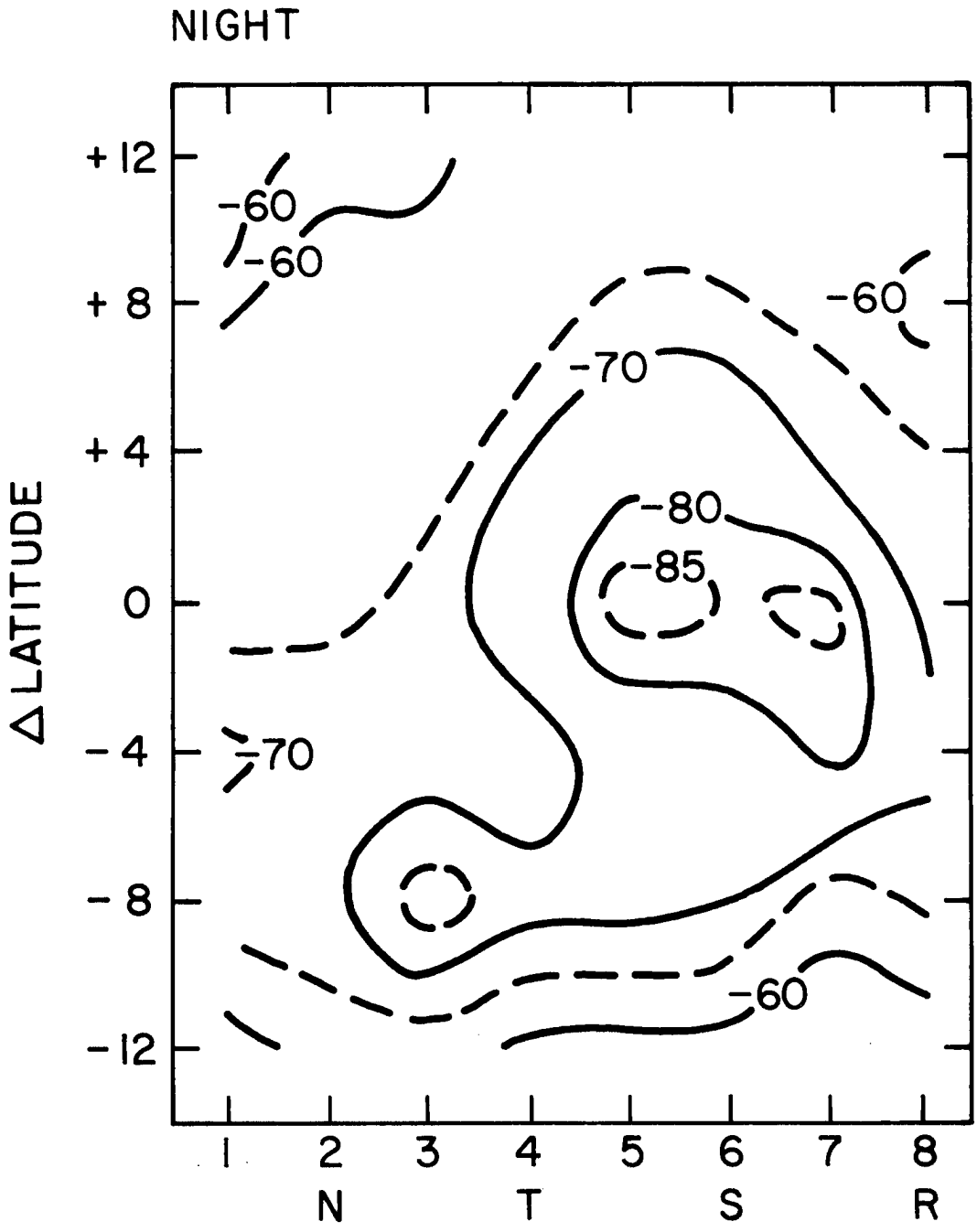

Figure 21. Radiative convergence for the 400-100 mb layer using nighttime cloud distributions. For explanation of axes see Figure 10. Values are in W m^{-2} (300 mb)$^{-1}$.

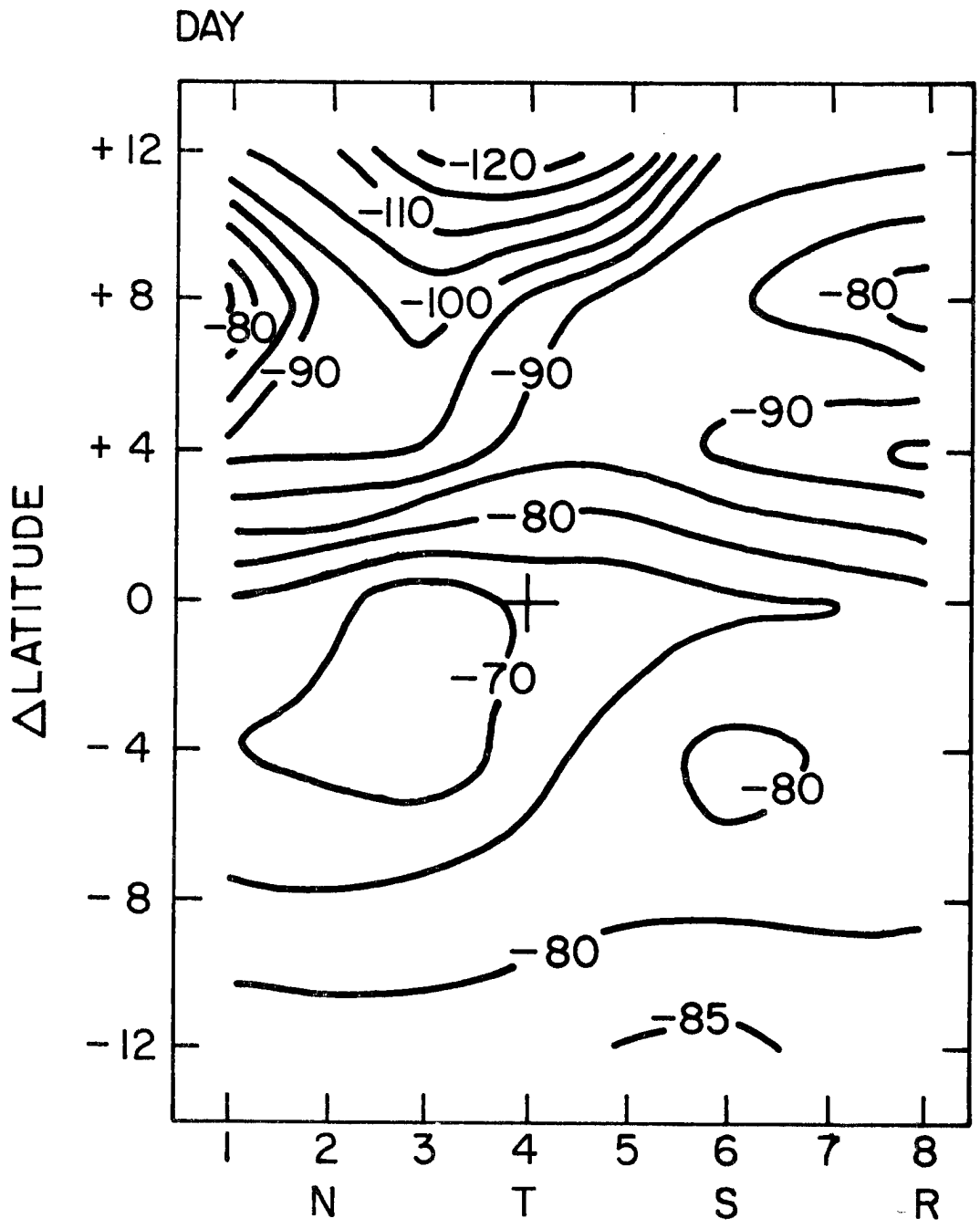

Figure 22. Daytime total tropospheric convergence as a function of wave position. For explanation of axes see Figure 10. Values are in W m^{-2} (912 mb)$^{-1}$.

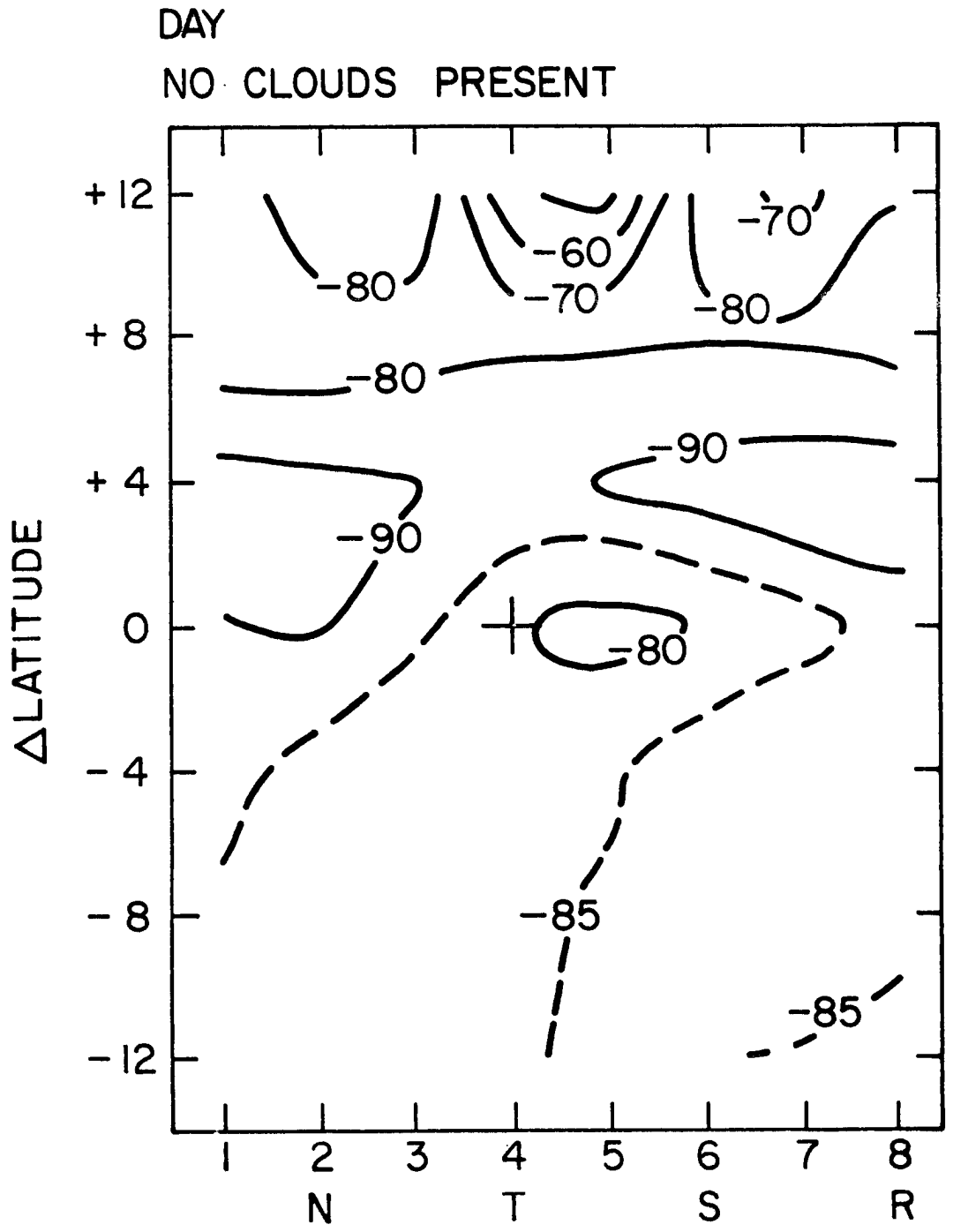

Figure 23. Daytime component of total tropospheric convergence assuming that no clouds are present. For explanation of axes see Figure 10. Values are in W m^{-2} (912 mb)$^{-1}$.

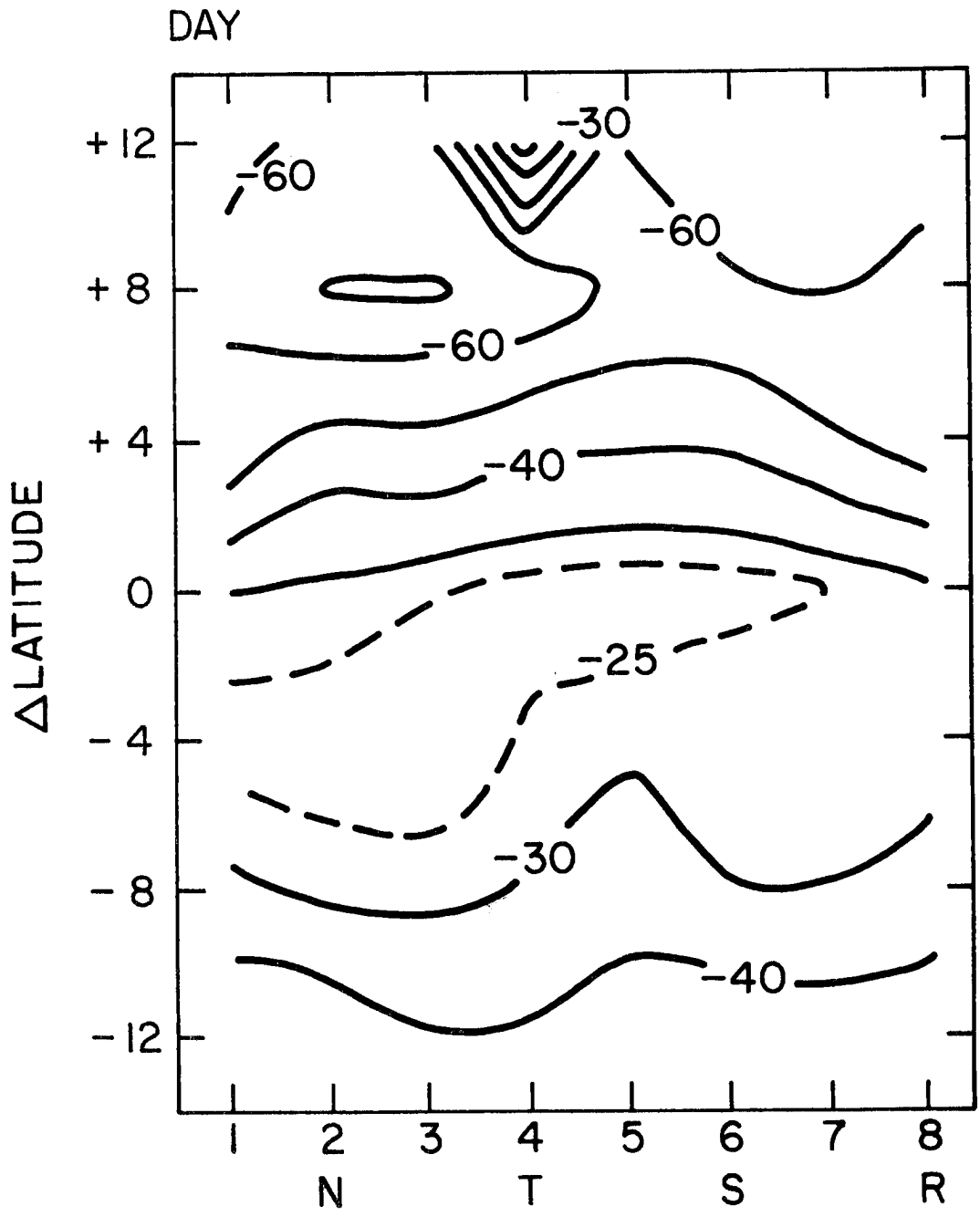

Figure 24. Radiative convergence for the 1000-700 mb layer using daytime cloud distributions. For explanation of axes see Figure 10. Values are in W m^{-2} (300 mb)$^{-1}$.

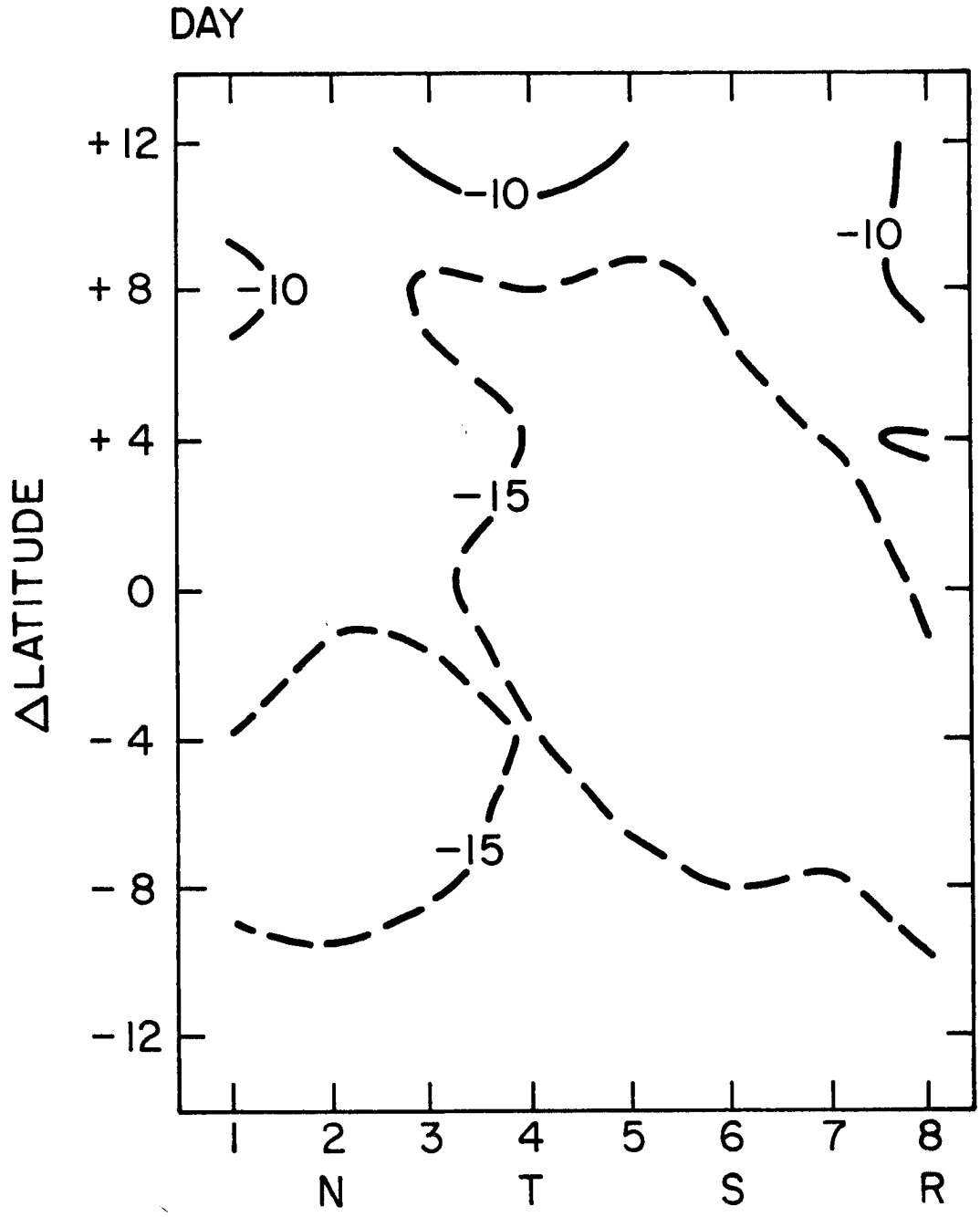

Figure 25. Radiative convergence for the 400-100 mb layer using daytime cloud distributions. For explanation of axes see Figure 10. Values are in W m^{-2} (300 mb)$^{-1}$.

composition and optical properties of the aerosols. Possible interactions between the radiation fields and wave dynamics may result in a modification of the wave circulation. It is, therefore, necessary to include a discussion of the modification of the radiative convergence profiles by the Saharan dust. The possible effects of the dust layer on the IR radiation budget are still largely unknown. Several researchers have found it to be insignificant when compared to the effects on the solar spectrum (Paltridge and Platt, 1972; Mani and Srinivasen, 1972; Liou and Sasamori, 1975; and Fischer and Grassel, 1975). While others (Idso, 1974; Kondratyev et al. 1976; Welch and Zdunkowski, 1974) imply that the Saharan dust may play an important role in modifying the IR radiative profiles. Physically, one might expect a relative cooling (warming) near the top (bottom) of the Saharan air layer (Kondratyev et al. 1976). However, it is generally agreed that aerosols have a significant effect on the solar spectrum; therefore we consider only the aerosols' effects on the solar spectrum.

Several studies have addressed the possible radiative effects of aerosols during the GATE (Kondratyev et al. 1976; Prospero et al. 1976; Minnis and Cox, 1978, etc.). To assess the radiative effects of aerosols (in a composite sense), within an easterly wave, the mean horizontal and vertical concentrations, size spectra, chemical composition and optical properties of the aerosols must be known as a function of wave position, however insufficient data were collected during GATE to make such a composite. An approximate aerosol composite may be constructued from the work of other authors. Such a composite lies within the noise level of our model. Therefore, a complete treatment of aerosol radiative effects, incorporating Mie theory and radiative

transfer routines, seems unjustified. Our assessment of the radiative effects of the Saharan dust shall, therefore, be simple and based on the results of other investigations. No attempt is made to include aerosol - cloud interactions.

It is helpful at this point to briefly summarize some results on aerosol properties reported by other researchers.

1) Horizontal distribution: With respect to an easterly wave dust concentrations tend to be largest east of the wave axis (trough) and north of the ITCZ (Carlson and Prospero, 1972; Savoie and Prospero, 1976) as depicted in Figures 26 and 27 (after Savoie and Prospero, 1976). There appear to be large horizontal gradients between the relatively clear areas and those areas of the Saharan outbreaks (Prospero and Carlson, 1972; Carlson and Prospero, 1972).

2) Vertical distribution: In the vertical, maximum dust concentrations occur near 700 mb, decreasing rapidly toward the top and base of the aerosol layer (Kondratyev et al. 1976; Carlson and Prospero, 1977).

3) Size distribution: Patterson and Gillette (1977) show that soil-derived aerosols of different geographical locations have similar size distributions. The size distribution off the coast of Africa was relatively invariant (Carlson and Prospero, 1977), although aerosol concentration varied considerably. As the outbreak moved across the Atlantic, the large dust particles settled out between the coast of Africa and Barbados (Savoie and Prospero, 1976). There was no significant difference in the size distribution between Barbados and Miami.

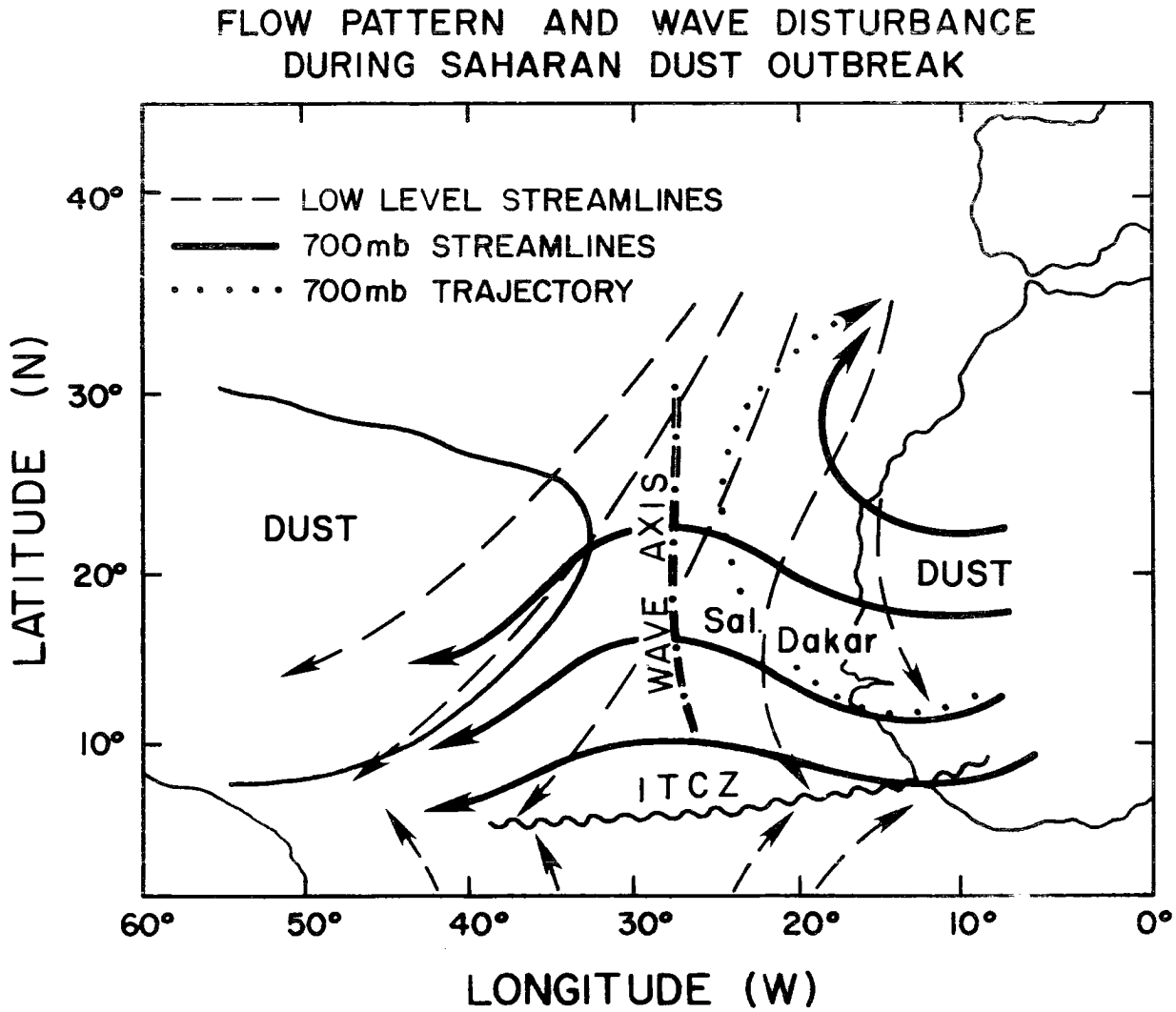

Figure 26. Flow pattern and wave disturbance during a Saharan dust outbreak. (After Savoie and Prospero [1976]).

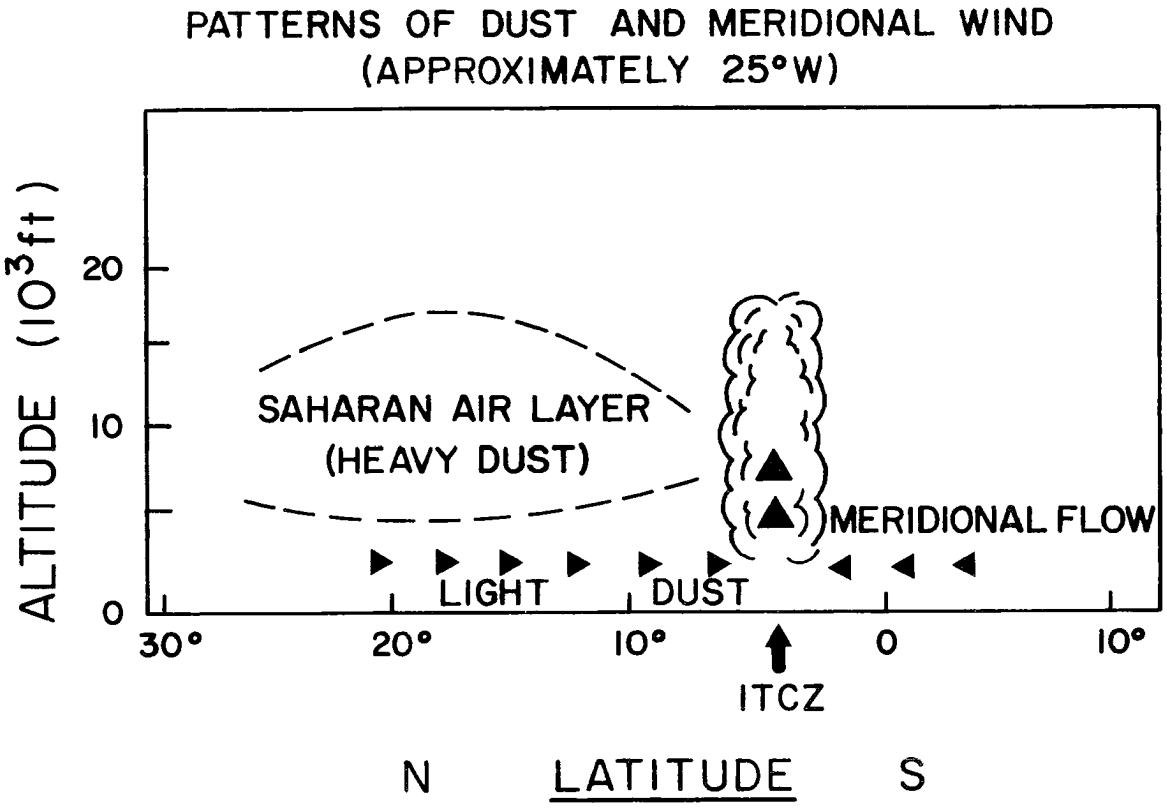

Figure 27. Patterns of dust and meridional wind during a Saharan dust outbreak (after Savoie and Prospero [1976]).

4) Index of refraction: Laboratory measurements (Patterson et al. 1977) of the complex index of refraction for Saharan aerosols showed no significant difference in samples taken on both sides of the Atlantic.

5) Composition: The principal component of the Saharan aerosols is mineral dust originating from the arid regions of NW Africa (Carlson and Prospero, 1972; Prospero and Carlson, 1972; and Kondratyev et al. 1976). The mineral composition of individual outbreaks is essentially invariant and closely resembles that of soil derived aerosols from other regions.

From a consideration of the above summary, the following advice of Carlson and Prospero (1977) seems appropriate:

"For practical purposes, one can consider Saharan dust to be a relatively uniform substance, at least with regard to its effect on the radiation field".

A first order approximation of the SW heating profiles due to Saharan aerosols shall be inferred from the results of Minnis and Cox (1978). The vertical distribution of the aerosol mass concentration is based on the mean aerosol loading measured during the four periods of BOMEX (Prospero and Carlson, 1972). We consider two vertical distributions, a "background" distribution and an "outbreak" distribution (Table 4). Following earlier authors, it is assumed that the Saharan outbreaks occupy the rows north of the reference latitude, or the ITCZ. The "background" distribution is assumed to occupy columns 2 through 5. The "outbreak" vertical distribution of aerosols occurs in Columns 1, 6, 7 and 8.

Pressure	BACKGROUND Concentration $\mu g\ m^{-3}$	BACKGROUND Weighting factor	OUTBREAK Concentration $\mu g\ m^{-3}$	OUTBREAK Weighting factor
500				
	8		10	
550		.33		.125
	8		10	
600				
	8		10	
650		.33		.25
	8		30	
700				
	8		60	
750		.33		.625
	8		40	
800				
	8		40	
850		0		0
	8		20	
900				
	8		16	
950		0		0
	8		16	
1000				
TOTAL	80			

Table 4. Vertical distribution of insoluable aerosol ($\mu g\ m^{-3}$), weighting factor applied to clear area heating rate, and derived aerosol absorption in $W\ m^{-2}$ per pressure interval for the background and outbreak aerosol concentrations.

Minnis and Cox (1978) studied the broadband radiative effects of the Saharan dust layer for seven case studies. Included in their results are fractional increases in atmospheric absorption of solar energy above the calculated clear sky values. This fractional increase ranged from approximately 4% to 20%. One should note that these values represent neither a minimum nor maximum condition. To calculate heating rates applicable to the easterly wave profile we begin by assuming that the "background" aerosol distribution results in a "clear sky" absorption increase of 4%, and the "outbreak" distribution has a fractional increase of 20%. The aerosol effect is confined below 500 mb. Assuming these fractional absorptions, we calculate the SW heating of the aerosol layer by multiplying the assumed fractional absorption by the corresponding clear layer heating rate (Appendix C). This results in a total heating rate for the aerosol layer (500 mb - surface) and is presented in Table C2.

In general, the layers at and above the maximum aerosol mass concentration (approximately 700 mb) have greater heating rates than the corresponding dust-free condition, while the bottom of the dust layer is unaffected or has a lower heating rate when compared to a corresponding dust-free condition (Minnis and Cox, 1978; Kondratyev et al. 1976). To approximate the aerosol effects on heating rates within the aerosol layer the additional absorption as a result of the aerosol is assumed to warm the 500 - 800 mb layer. The assumed total heating rate due to the aerosol is distributed in the vertical according to the weighting factors listed in Table 4. The additional aerosol radiative convergence should be added to the SW convergence profiles listed in Appendix B.

The effects of the aerosols on the daytime TTC profiles is demonstrated by considering the ratio of TTC with no aerosols (Table B4) plus the SW convergence due to aerosols (Table C2), to the TTC with no aerosols (Table B4), i.e.

$$\frac{TTC_{\text{no aerosols}} + CONVERGENCE_{\text{aerosols}}}{TTC_{\text{no aerosols}}} . \qquad (4.1)$$

This ratio is given in Tables 5a and b as a function of wave category for the three northern rows for the daytime period and the 24 hour period. The background distribution is assumed to have a fractional increase in atmospheric absorption over the clear sky absorption of .04. The effects of two "outbreak" distributions are presented, representing a "clear sky" absorption increase of .2 and .5. One notes the spacial homogeneity of the aerosol affect. The additional convergence resulting from the presence of the aerosol layer will reduce the tropospheric radiative convergence profiles below 500 mb, thereby enhancing the difference between the daytime and nighttime heating gradients.

The changes in the vertical radiative convergence profiles due to the presence of aerosols need more theoretical and observational investigation.

4.3 Comparison With Previous Computations

Figure 28 is a comparison of the radiative convergence profiles of the present study's wave mean profile of Δ latitudes 0 and -4, Dopplick's mean climatological computation at 10°N for June, July and

Δ latitude/column	1	2	3	4	5	6	7	8
+12	.86 (.65)	.97	.97	.98	.98	.84 (.59)	.83 (.58)	.84 (.60)
+8	.81 (.53)	.97	.97	.97	.96	.82 (.55)	.82 (.54)	.81 (.52)
+4	.83 (.57)	.97	.97	.96	.96	.82 (.55)	.82 (.55)	.83 (.57)

Table 5a. Daytime

Δ latitute/column	1	2	3	4	5	6	7	8
+12	.92 (.79)	.98	.98	.98	.98	.90 (.76)	.90 (.76)	.91 (.77)
+8	.90 (.75)	.98	.98	.98	.98	.90 (.75)	.90 (.75)	.90 (.75)
+4	.90 (.75)	.98	.98	.98	.98	.89 (.73)	.89 (.74)	.90 (.74)

Table 5b. 24 hour

Tables 5a and b. Fractional increase in the daytime total tropospheric convergence and the 24 hour total tropospheric convergence as a result of including aerosols, as a function of wave column for the three northern rows. Columns 2-5 assume an aerosol fractional increase of .04. Columns 1, 6, 7 and 8 assume an aerosol fractional increase of .2 and in parenthesis, .5.

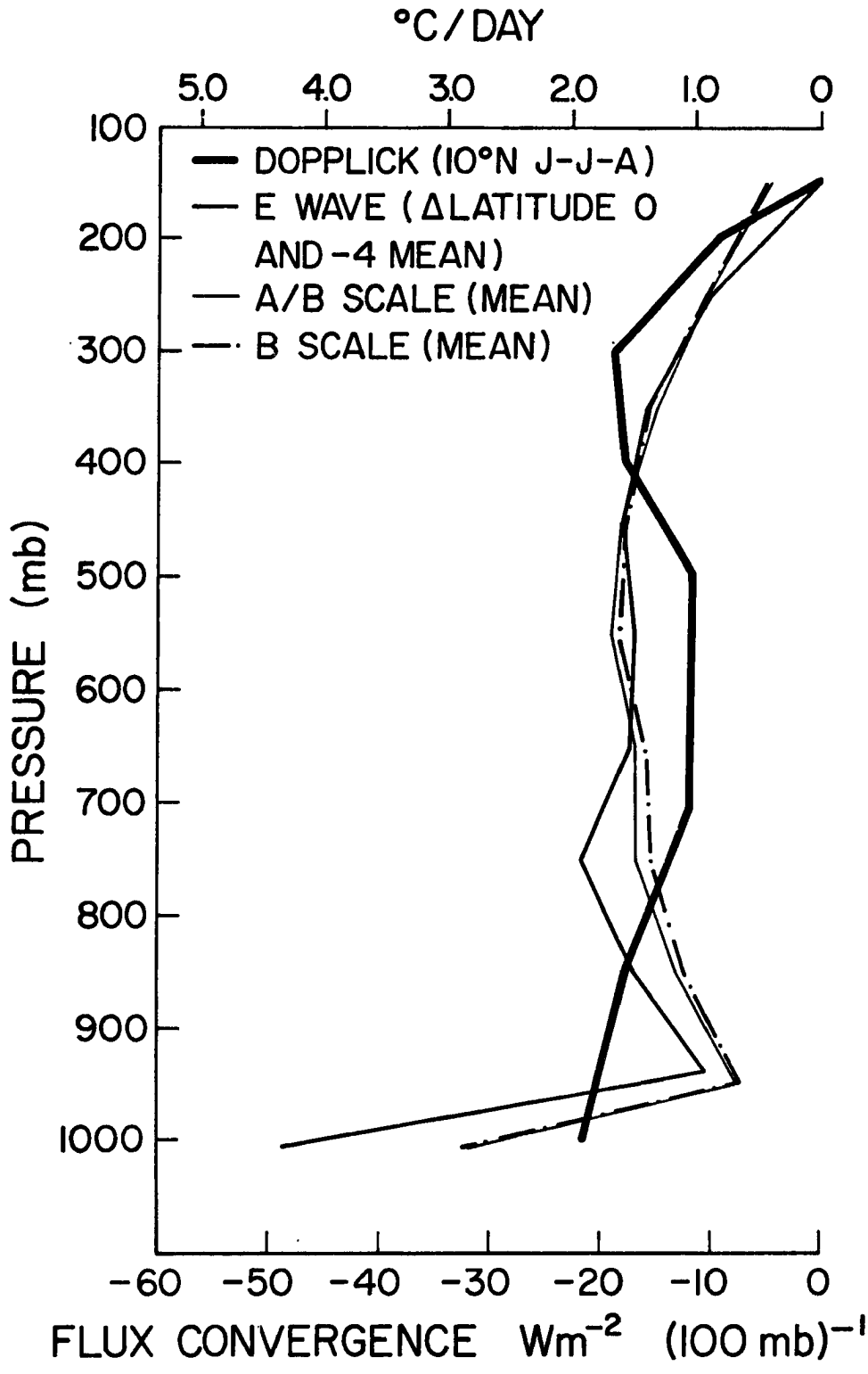

Figure 28. Intercomparison of radiative convergence profiles.

August, and the mean wave radiative convergence profiles for the A/B and B-scale arrays derived from the results of Cox and Griffith (1978).

The differences in the profiles of Dopplick and the present study are related to the different methods of incorporating cloud distribution and the water vapor continuum band. Dopplick has less total cloud amount that the present study and does not include the water vapor pressure dependent absorption in the 8 - 12 μm region. Above 400 mb Dopplick's profile shows a larger cooling than the present study. This result is due to the difference in cloud top assignment. Dopplick consistently places cloud tops at the same height, whereas in the present study cloud tops are distributed within the 300 mb layer according to the satellite-derived areal coverage. Also, we allow two cloud base assignments as opposed to a single cloud base assignment in the Dopplick profile. The larger cooling between 450 and 800 mb is primarily due to the greater amounts of water vapor and the cloud distribution in the present study. The suppressed cooling below 850 mb of the present study as compared to Dopplick is likely a result of the water vapor continuum (Cox, 1973) and our constant assignment of low cloud base at 950 mb.

Thompson et al. (1978) have listed wave category as a function of three hour intervals for each day in Phase III of GATE. From this data set the radiative convergence profiles for the A/B and B-scale arrays as a function of wave category were composited from the results of Cox and Griffith (1978). The results are listed in Appendix D for those interested in budget studies over the A/B and B-scale arrays.

The differences in the profiles determined from the CG data and the present study are due to mean temperature and moisture differences,

and cloud top distribution. The A/B and B-scale arrays tended to have larger amounts of high clouds compared to the large scale composite as can be seen in Appendices A and D of this study and the results of Reed et al. (1977) compared with Thompson et al. (1978). This accounts for the larger upper tropospheric cooling of the A/B and B-scale composite. The present study also has more clear and low cloud amounts than the CG profiles contributing to the larger lower tropospheric cooling. The composite temperature and moisture profiles of Reed et al. (1977) include both land and ocean. This results in a slightly warmer, drier profile than that observed within the ship arrays during Phase III of GATE resulting in a larger cooling in the lower atmosphere. A meridional comparison can be made between the mean radiative convergence profiles of Δ latitude 0 and -4 with the B-scale array easterly wave profiles. These profiles are shown in Figures 29 and 30 respectively. The differences in the latitudinal mean (Figure 28) are reflected in each of the individual column profiles. The deviation about the mean profile is less in the present study. Both profiles indicate a middle tropospheric maximum cooling in the non-convective regions of the wave.

Finally the results of this study can be composited in a manner similar to the method used by Johnson (1979). Using the radiative heating profiles of Cox and Griffith (1979), Johnson derived a wave composite net radiative heating by weighting the radiative profiles of each category according to the frequency of occurrence of each wave category as a function of time of day. The frequency distribution of the wave categories is given in Table 6. By weighting the nighttime and daytime mean Δ latitude 0 and -4 net radiative profiles of the

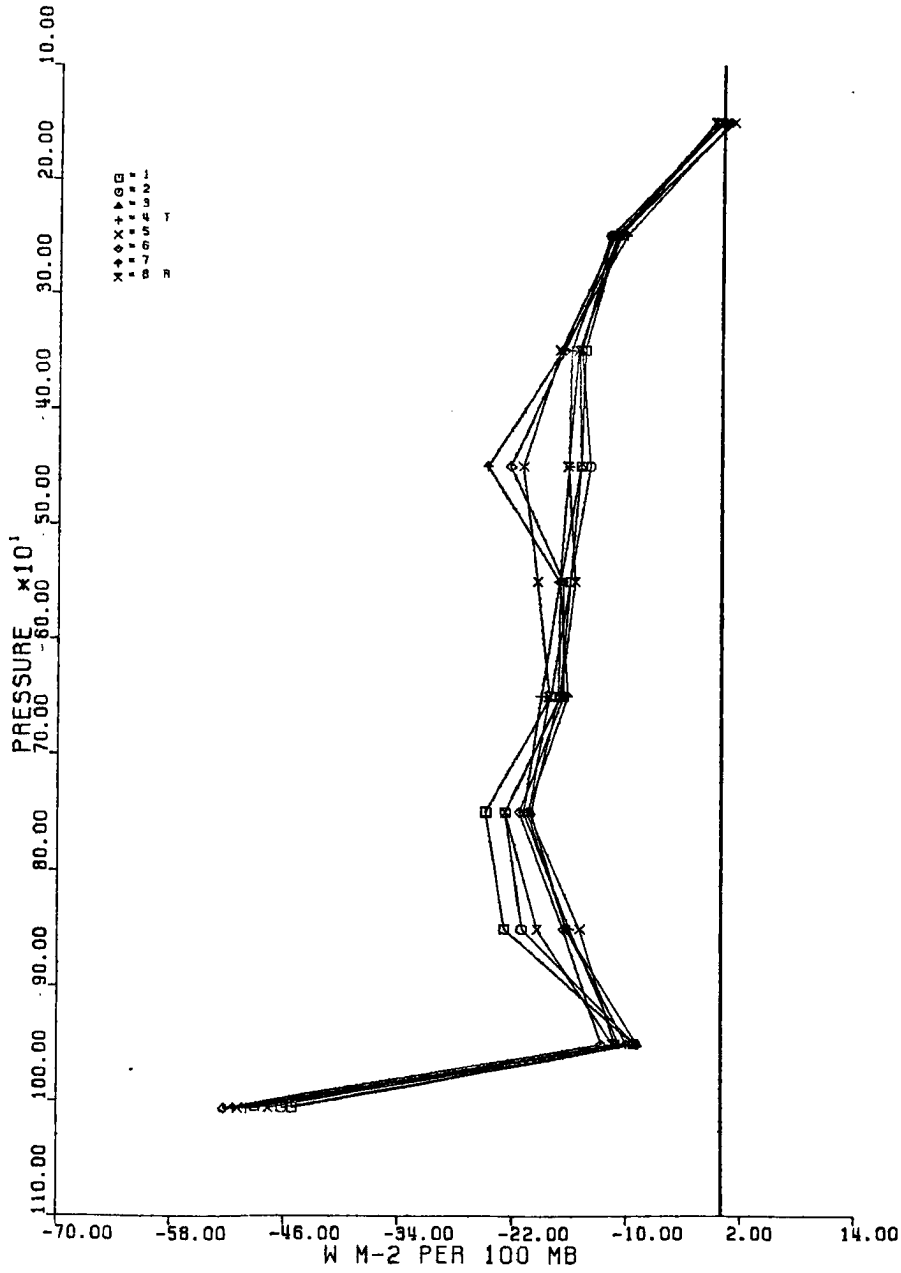

Figure 29. Δ latitude 0 and -4 mean vertical radiative convergence profiles (W m^{-2} per 100 mb) as a function of wave column. The symbol representation of each column is shown in the upper left-hand corner of the figure.

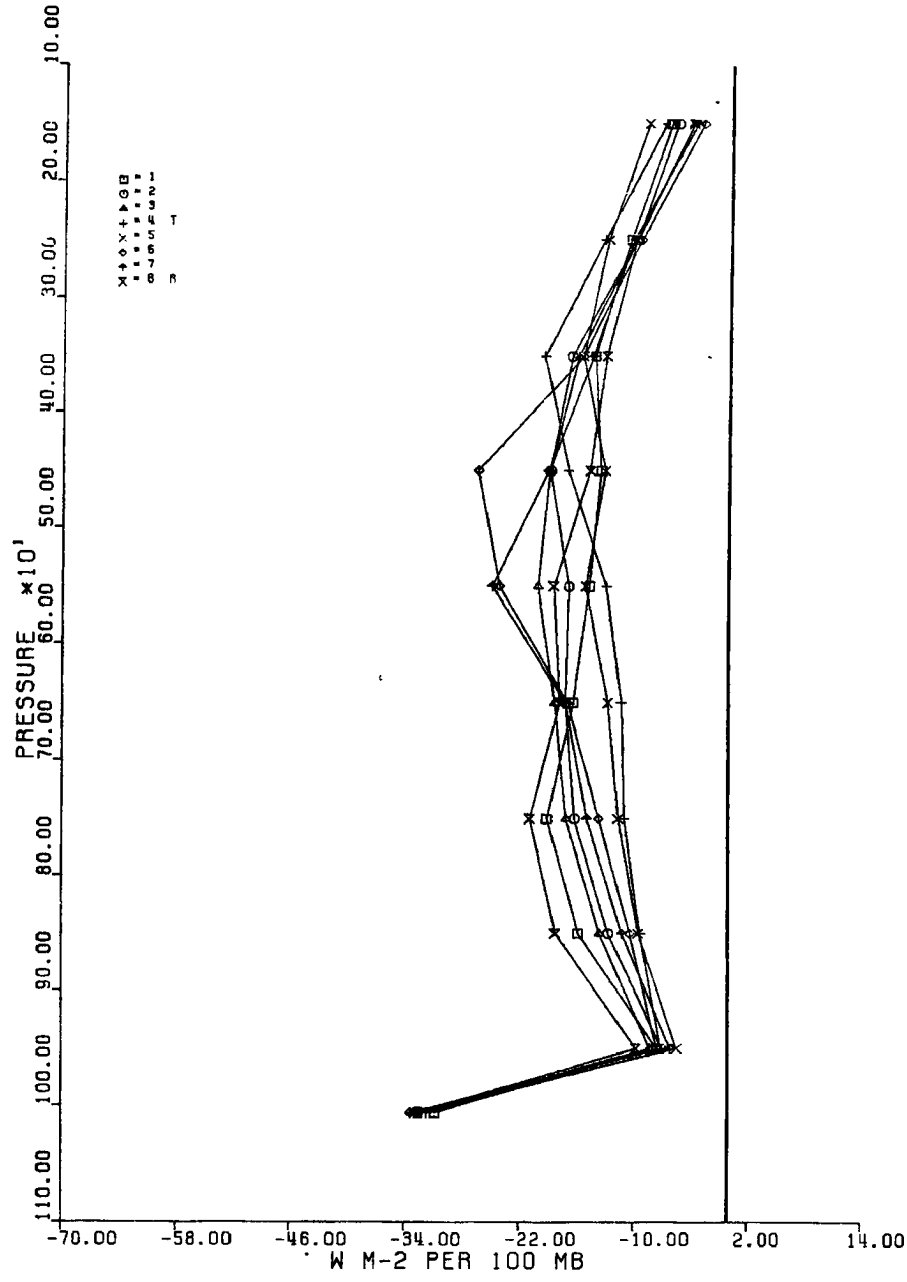

Figure 30. B-scale array vertical radiative convergence profiles (W m^{-2} per 100 mb) as a function of wave column. The symbol representation of each column is shown in the upper left-hand corner of the figure.

WAVE CATEGORY	FREQUENCY OF OCCURRENCE NIGHT (2100 - 0000 GMT)	DAY (0900 - 1000 GMT)
1	1	15
2	18	5
3	7	9
4	10	11
5	10	7
6	12	14
7	7	12
8	15	7

Table 6. Frequency of occurrence of composite wave category.

present study with the frequency distribution of Table 6, a similar composite is derived. This composite and the net radiative heating composite presented by Johnson (1979) are depicted in Figure 31.

Both studies exhibit a minimum cooling in column 1 of the composite. This feature is a result of the large diurnal difference in the occurrence of wave category over the A/B array. A maximum cooling exists in the middle troposphere between columns 4 and 7 in both studies. The tendency for a greater nighttime occurrrence of wave categories 2 and 8 results in a relative maximum cooling in these two columns for both of the studies. The location of the maximum cooling in categories 2 and 8 occurs lower in the atmosphere in the present study.

The results of the comparisons between the radiative convergence profiles and cloud amounts derived in the present work with that of other studies (e.g. Cox and Griffith, 1979; Johnson, 1979; Reed et al. 1977; Thompson et al. 1978) lends to the confidence in the accuracy of the derived profiles of the present study. This confidence, along with the increasing awareness of the importance of radiative heating on cumulus convection, supports the use of the present study's radiative profiles in diagnostic studies of synoptic scale disturbances during Phase III of the GATE.

4.4 Radiative-Dynamic Coupling Mechanisms

A diurnal cycle in vertical velocity has been documented by several authors (Gray and Jacobson, 1977; McBride and Gray, 1978; and Dewart, 1978). These authors hypothesize that this diurnal cycle is a consequence of the difference in the day-night tropospheric radiative

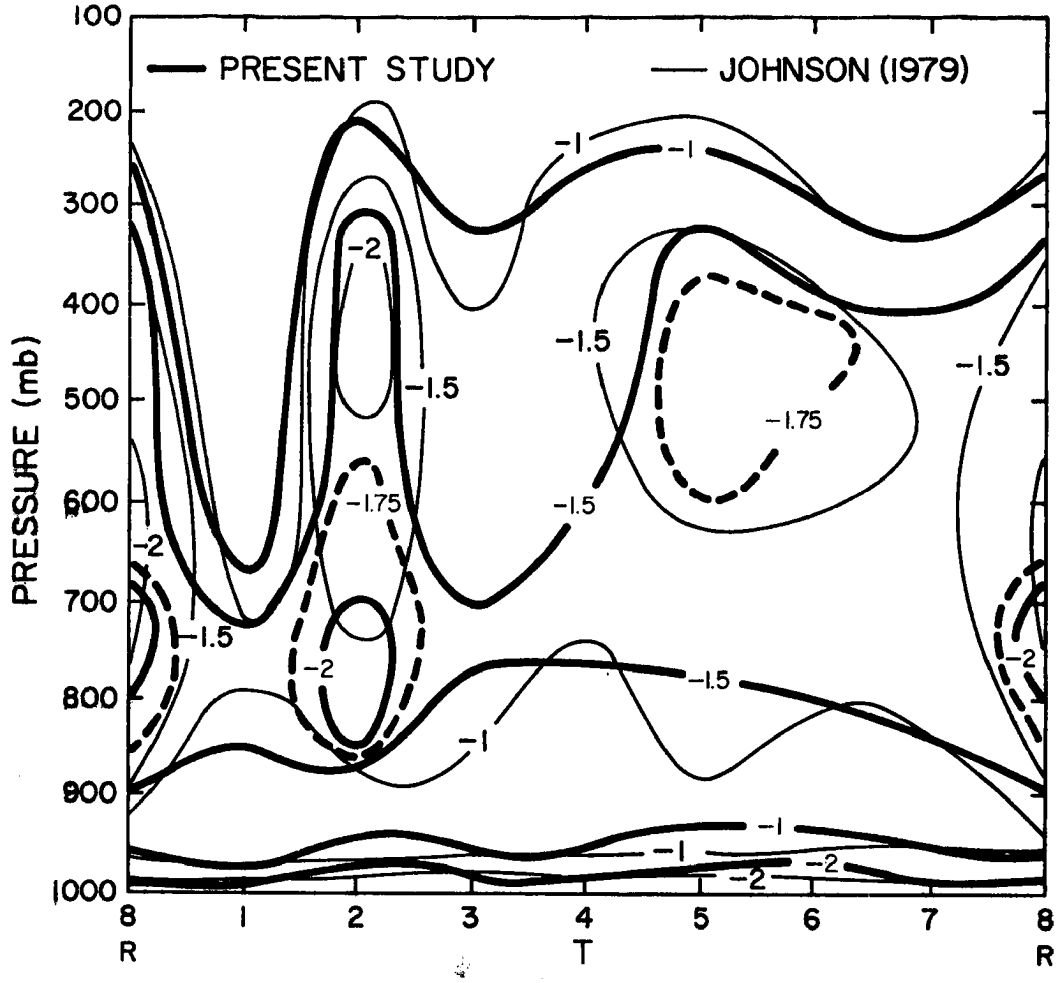

Figure 31. The mean Δ latitude 0 and -4 net radiative heating in °C/day for a wave composite that is weighted according to the diurnal frequency of occurrence of the wave category. Also shown is a similar composite presented by Johnson (1979).

convergence profiles between tropical weather systems and the environment. A synoptic scale control on the diurnal variation of convective activity can be implied from the work of Albrecht and Cox (1975). Using a steady-state model, they demonstrated that the vertical motion in the convective region of a wave is coupled to the location and magnitude of an upper tropospheric radiative energy loss. Although Albrecht and Cox only considered infrared cooling, inclusion of the SW radiative component would reduce the radiative cooling, thereby reducing the vertical motion in the convective region of the wave and increasing the diurnal difference.

An interesting result of the composite profiles is demonstrated in a plot of the zonal cross section through the path of the disturbance center, Figure 32. The predominant feature is the 400 - 500 mb relative maximum cooling between columns 5 and 7. Albrecht and Cox (1975) discussed the sensitivity of the phase difference of the convective and radiative heating to diagnosed motions. They showed that the minimum 200 mb meridional wind perturbations and divergence occurred when a maximum in upper tropospheric cooling was centered over the convective heating, and increased to a maximum as the relative maximum upper tropospheric cooling was centered a half wavelength from the convective heating. Reed et al. (1977) show a maximum in precipitation W-SW of the wave center. Assuming maximum convective heating W-SW of the disturbance center, a maximum upper tropospheric cooling between Δ latitude 0 and Δ latitude -4 and approximately column 7 would result in maximum diabatic forcing. This maximum relative cooling between 400 - 500 mb is larger in the zonal cross section through Δ latitude -4. Other rows do not exhibit this large relative maximum cooling.

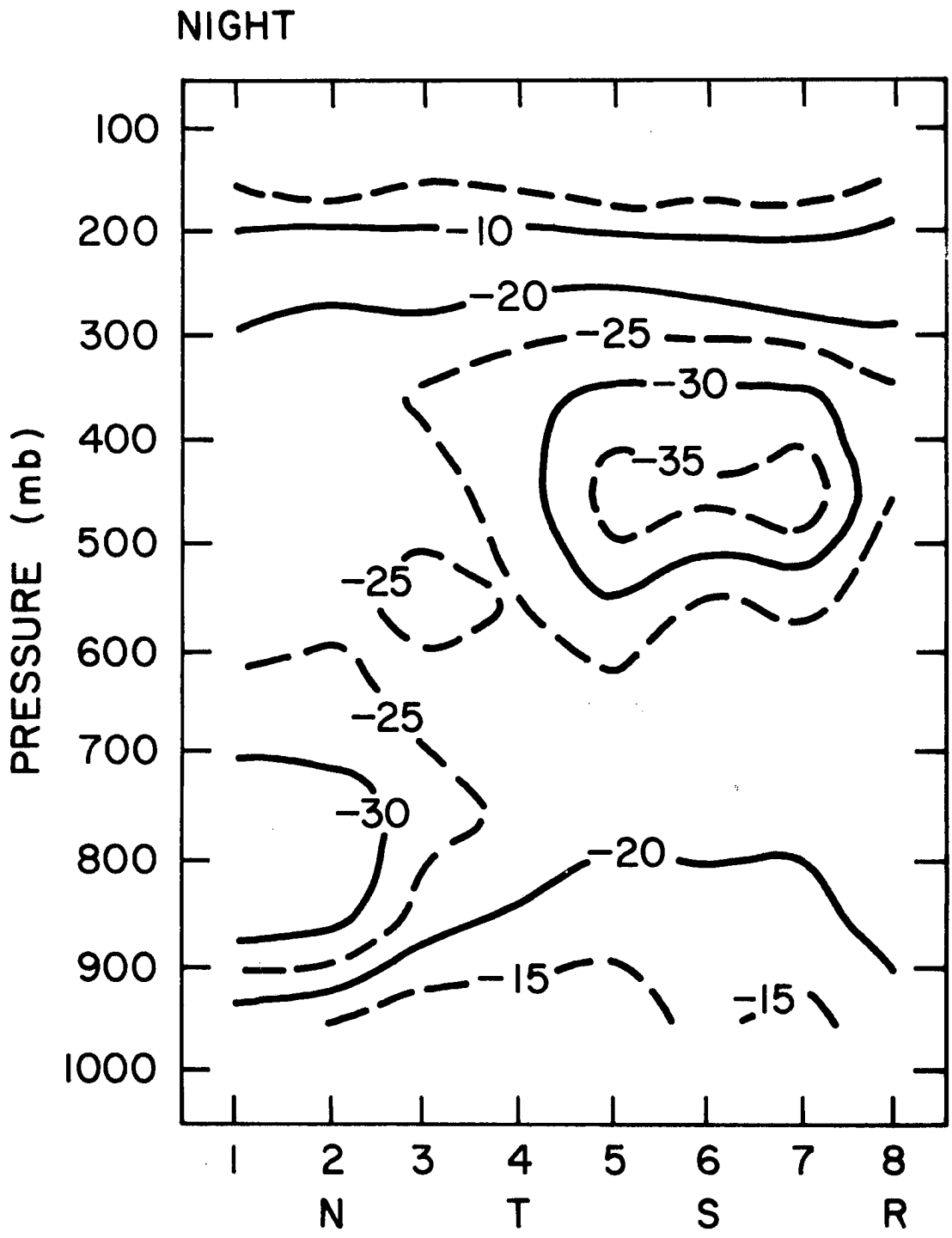

Figure 32. Nighttime radiative convergence profiles of the vertical cross section through the path of the disturbance center (Δ latitude 0). Values are in W m^{-2} (100 mb)$^{-1}$.

This relative maximum cooling is approximately 200 mb lower and 50% less in magnitude than the difference used by Albrecht and Cox (1975). A plot of the daytime zonal cross section through the path of the disturbance center, Figure 33, shows no middle tropospheric maximum cooling as is the case in the nighttime profile. Figure 34 depicts the differences in the radiative convergence profiles of columns 3 and 7 for Δ latitude -4 between the daytime and nighttime composites. Also shown is the difference in the perturbed and unperturbed profiles derived from the Line Island Experiment (LIE) by Albrecht and Cox (1975). The nighttime profile differences are considerably larger than the daytime differences, and yet much smaller than the differences derived by Albrecht and Cox. Since the day-night differences are much smaller than the heating differences used by Albrecht and Cox, it appears as though a radiative induced diurnal modulation of the vertical motion field will be small. However, this conclusion is somewhat speculative since the mean dynamic and thermodynamic fields of the two regions are different.

McBride and Gray (1978) discuss two physical mechanisms that may be responsible for the observed diurnal variation in vertical velocity of tropical weather systems. The first physical mechanism results from the work of Gray and Jacobson (1977) (GJ) and Fingerhut (1978). The mechanism is based on radiational differences between organized mesoscale cloud clusters and surrounding cloud free regions. The radiative cooling of the clear regions surrounding the disturbance are compensated for by subsidence. This subsidence, which is larger at night, results in low level convergence in the adjacent clusters. At upper levels the presence of clouds in the cluster results in a larger

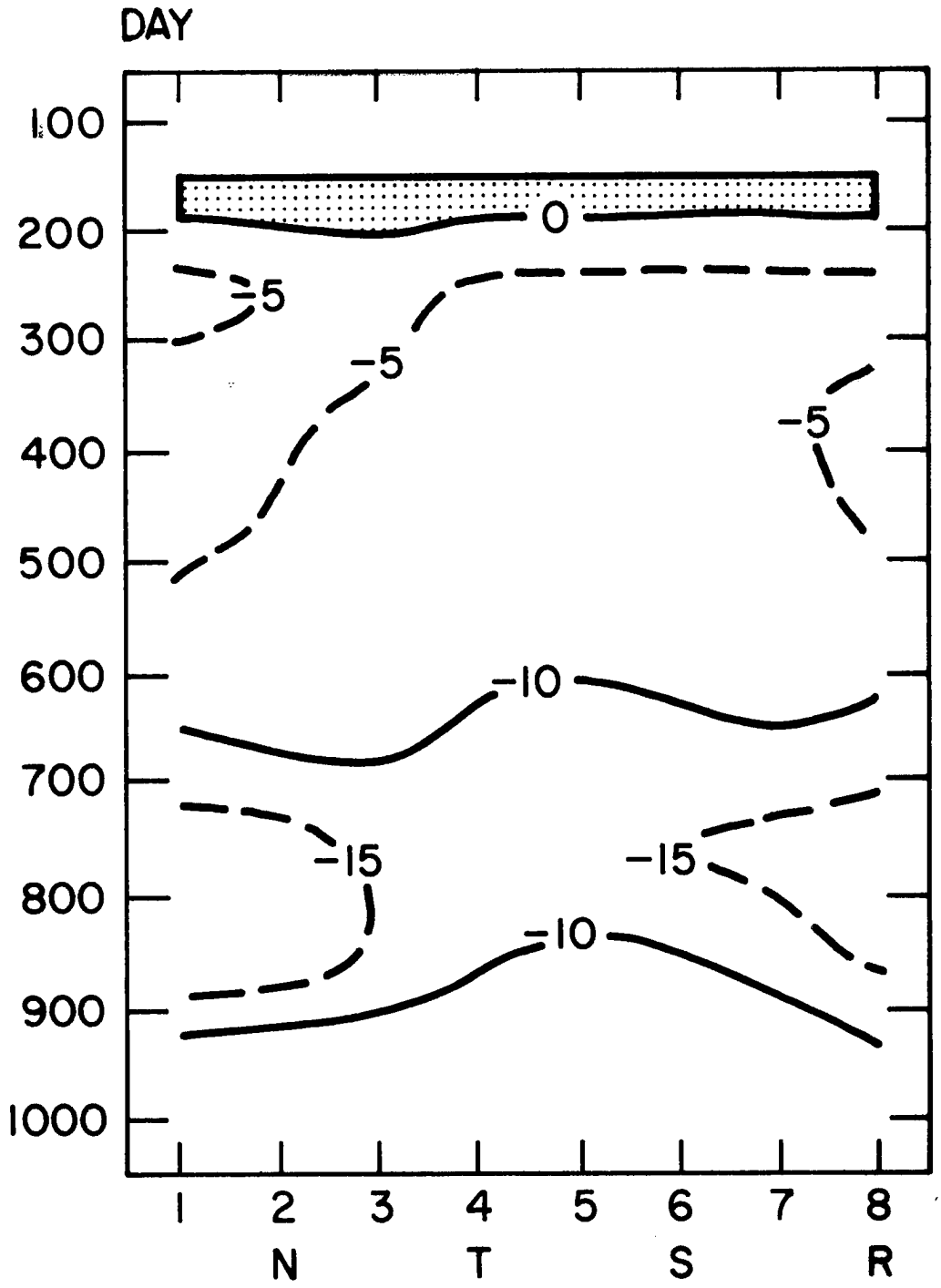

Figure 33. Daytime radiative convergence profiles of the vertical cross section through the path of the disturbance center (Δ latitude 0). Shaded region represents positive convergence. Values are in W m^{-2} (100 mb)$^{-1}$.

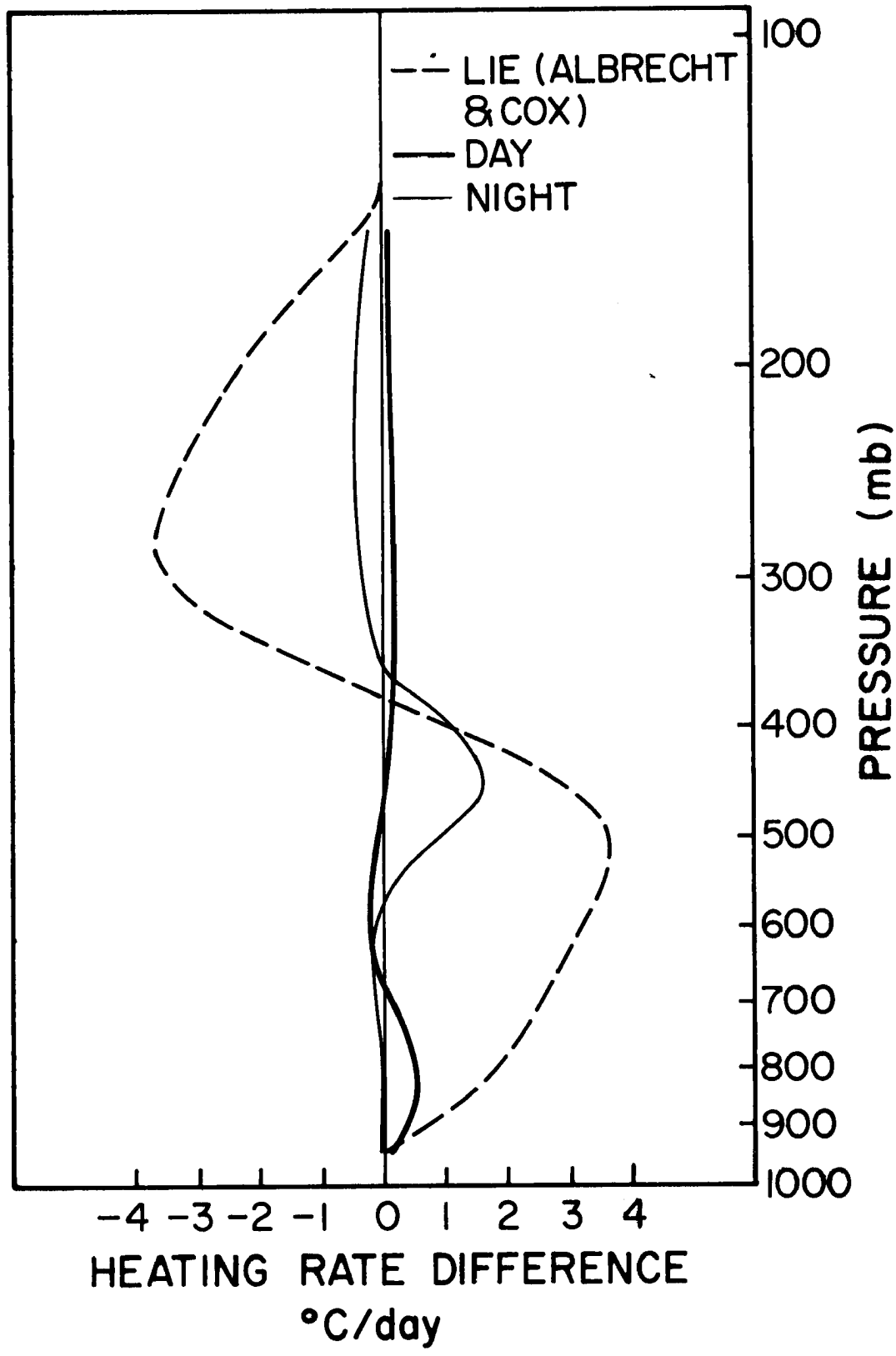

Figure 34. Heating differences in the radiative convergence profiles of columns 3 and 7 for Δ latitude -4 for the day and night composites. Also shown is the difference in the perturbed and unperturbed profiles derived from the Line Island Experiment by Albrecht and Cox (1975).

IR loss than the upper level clear regions. This larger cooling rate induces a larger upper level pressure gradient force directed from the cluster to the clear region. This upper level outward pressure gradient force is larger at night and less during the day due to the SW absorption by the upper level clouds. This radiative forcing tends to produce a larger cluster mass convergence in the early morning than in the afternoon-evening. It is hypothesized that convergence actually lags the radiational forcing by 3-6 hours (McBride and Gray, 1978). Payne and McGarry (1977) have shown a relationship between convective activity and easterly waves off the west coast of Africa during Phase III of GATE. The cloud clusters occupy the region of the wave between Δ latitude 0 and Δ latitude -4, and are generally located slightly ahead of the 700 mb trough. In this region of the wave one might expect a late morning maximum in convective clouds. In the present study, the percentage of high cloud tops (above 400 mb) associated with the maximum convective regions of the wave has a small 12 hour daytime maximum.

To investigate the role of the radiational forcing between cluster and cloud free regions, radiative profiles were composited from the data of Cox and Griffith (1979). Each 1/2° box in the Phase III B array for 3 hour intervals, starting at 0000 GMT, was classified as an environment region or a cloud cluster region. Cloud systems were categorized into two types: those clusters that had a large percentage of total area covered with cloud tops above 300 mb, and those which did not. This partitioning is an attempt to separate the cloud systems into clusters that are (or recently were) convectively active (tops above 300 mb) from those that are not (tops below 300 mb).

Tables 7a and b show the differences between the Phase III clear and cluster radiative energy flux profiles for both day and night. Negative values indicate that the cluster region has a smaller radiative cooling rate than the clear region, which if unbalanced, would establish a pressure gradient force toward the cluster. A positive difference results from the cluster having a larger radiative cooling rate, thus potentially inducing an outward pressure gradient force with respect to the cloud cluster. During the night, the mechanism proposed by GJ is evident, although the magnitude of the radiation difference is less than that assumed by GJ and Fingerhut (1978). In the present study we are considering the entire cluster, GJ considered only the differences between the cloud-free region and the disturbance underneath the cloud shield. As a result of the larger area average, the cloud top distributions outside the shield region reduce the radiative difference between the cluster and the clear regions, explaining the smaller magnitude. We also note that convective heating, which is not included in Table 7, enhances the diabatic heating differences between the cluster and environment (McBride and Gray, 1978). During the day, the pressure gradient forces are less, and the organized two-cell type circulation tends to break into a three-cell forced circulation. It, therefore, appears that although maximum cloudiness and convective activity are observed in the late afternoon over the GATE area, radiative forcing tends to be working towards a morning maximum as hypothesized by GJ. We note here that the cloud systems observed during Phase III of GATE tended to be oriented east-west. Thus, the clear-cluster radiative forcing discussed above is primarily meridional.

CLEAR-CLUSTER FOR DAY PERIODS (0900 - 1800 GMT)

(watts m^{-2} per pressure interval)

PRESSURE	CLEAR MINUS ACTIVE CLUSTER	(°C/Day)	CLEAR MINUS NON-ACTIVE CLUSTER	(°C/Day)
100	3.74	.32	.21	.02
200	-1.67	-.14	-.63	-.05
300	4.31		4.03	
400	6.62	.43	9.21	.47
500	4.51		8.25	
600	-.53		.63	
700	-7.59	-.40	-7.78	
800	-6.15		-7.05	-.62
900	4.6		5.27	
1000	.86	.41	.93	.47
SURFACE				
TOTAL	8.7	.08	13.07	.12

Table 7a. Clear minus cluster difference in tropospheric radiative convergence for the daytime periods during Phase III of GATE.

CLEAR-CLUSTER FOR NIGHT PERIODS (2100 - 0600 GMT)

(watts m^{-2} per pressure interval)

PRESSURE	CLEAR MINUS ACTIVE CLUSTER	(°C/Day)	CLEAR MINUS NON-ACTIVE CLUSTER	(°C/Day)
100				
	11.49		2.49	
200				
	8.89	.66	3.43	
300				
	3.27		5.93	.44
400				
	-3.72		9.12	
500				
	-10.14		5.18	
600				
	-16.61	-1.28	-7.1	
700				
	-25.53		-20.54	1.27
800				
	-24.47		-23.07	
900				
	-10.91		-9.56	
1000				
	.05	.04	.13	.91
SURFACE				
TOTAL	-67.68	-.63	-33.99	-.31

Table 7b. Clear minus cluster difference in tropospheric radiative convergence for the nighttime periods during Phase III of GATE.

The second physical mechanism proposed by McBride and Gray to explain the observed diurnal variations in vertical velocity is based on the radiative differences between the ITCZ and its surrounding regions. McBride and Gray hypothesize that the radiative cooling in the regions to the north and south of the ITCZ are balanced by subsidence warming. They envision this subsidence converging into the ITCZ resulting in a diurnal modulation of the vertical velocity. Following Haltiner and Martin (1957) the diabatic component of the vertical velocity may be written as

$$\omega_R = \frac{-g}{c_p} \frac{\partial F_n}{\partial p} \left[\left(\frac{p}{1000}\right)^{R/c_p} \frac{\partial \theta}{\partial p}\right]^{-1} \qquad (4.2)$$

where $g \equiv$ acceleration due to gravity

$c_p \equiv$ specific heat of dry air at constant pressure

$F_n \equiv$ net radiative energy flux ($W\ m^{-2}$)

$p \equiv$ pressure

$R \equiv$ gas constant of dry air

$\theta \equiv$ potential temperature.

The radiative energy loss from the mean row conditions for each of the seven rows are used in the ω_R equation given above to compute diabatic vertical velocity. Table 8 lists the absolute ratios of the nighttime required compensating vertical motions to the daytime values as a function of wave composite row. The ratios are given at 100 mb intervals and for the total tropospheric subsidence. Except for Δ latitude +12, the required nighttime subsidence is more than twice the subsidence needed to balance the daytime total tropospheric

PRESSURE/ Δ latitude	+12	+8	+4	0	-4	-8	-12
100	1	1	1	1	1	1	1
200	2.4	2.2	2.6	3.4	3.6	3	2.6
300	7	4.8	5.3	5.4	4.1	4.9	4.5
400	25	27	7.8	4.8	4.7	5.7	6.2
500	8.2	00	7.4	3.4	3.6	4.4	6.0
600	32.8	8.7	3.4	2.3	2.4	2.6	3.2
700	1.2	2.4	1.7	1.7	1.7	1.8	2.1
800	1.4	1.5	1.4	1.7	1.7	1.8	1.9
900	1.1	1.3	1.8	2.3	2.1	1.9	1.6
1000							
TOTAL	1.7	2.5	2.3	2.6	2.6	2.6	2.3

Table 8. Nighttime to daytime ratio of the absolute values of required compensating vertical motions.

radiative energy losses. To further investigate this diurnal range, we consider the latitudinal mean subsidence of three regions; one north of the ITCZ (Δ latitude +8 and +4), the ITCZ (Δ latitude 0 and -4) and one south of the ITCZ (Δ latitude -8 and -12). According to the work of McBride and Gray (1978), the radiative cooling of tropical weather systems is closely balanced by a subsynoptic local up- and down circulation. With this subsynoptic convective heating balancing the radiative cooling, the diabatic component of vertical motion is likely to be very small within the ITCZ. Assuming the easterly wave to be mass balanced, the sinking motions north and south of the ITCZ may result in low level convergence into the ITCZ and subsequent upward vertical motions in the ITCZ with return outflow in the upper levels. Table 9 shows the diurnal difference in the latitudinal mean subsidence (mb/day) required to balance the radiative cooling north and south of the ITCZ region. Note that the vertical motions listed in Table 9 are integrated values through the troposphere (1000 mb - 100 mb). The subsidence values presented represent a 12 h mean value. Based upon radiative modulation arguments one would expect the maximum subsidence to occur between 0000-0600 LST, and the minimum subsidence between 1200-1800 LST. The modeling results of Fingerhut (1978) suggest that the convergence cycle actually lags the radiative forcing by 3-6 h.

Also given in Table 9 are the corresponding upward vertical motions in the ITCZ assuming all of the subsidence in the north and south regions converges into the ITCZ region. The N-S convergence into the ITCZ is supported by the work of Gray et al. (1977). From analysis of the GATE rawinsonde data Gray et al. (1977) found that the strong low level convergence in the GATE A/B and B-scale arrays is primarily due

	VERTICAL MOTION (mb/day)		
	DAY	NIGHT	NIGHT-DAY DIFFERENCE
North region (Δ latitude +8 and +4)	37	89	52
ITCZ region (Δ latitude 0 and -4)	-70	-170	-100
South region (Δ latitude -8 and -12)	33	81	48

Table 9. The diurnal differences in the latitudinal mean subsidence, in mb/day, required to balance the tropospheric radiative cooling north and south of the ITCZ region. Also given is the corresponding upward vertical motions assuming this subsidence converges into the ITCZ region.

to the N-S shear of the meridional wind (i.e. $\partial v/\partial y$). The resulting diurnal difference of the integrated tropospheric vertical motions at the ITCZ region is approximately 100 mb/day. This 12 h mean diurnal difference of 100 mb/day is the approximate magnitude of the maximum observed diurnal difference in the vertical velocities of the GATE region (McBride and Gray, 1978; Dewart, 1978). This suggests the reasonable conclusion that not all of the compensating subsidence north and south of the ITCZ region converges into the ITCZ. Note that we have not considered the most northern region of the wave, Δ latitude +12. Inclusion of this region in the model discussed above would result in a diurnal difference of approximately 135 mb/day.

V. CONCLUSIONS

A composite cloud top areal coverage for an eastern Atlantic wave has been derived from satellite data for seventeen time periods during Phase III of GATE. The composite model indicates greater cloud cover during the 12 hour nighttime period than during the daytime period over most of the wave. The nighttime percentage of upper and middle level cloud tops is greater than the daytime coverage in the region of minimum convection. In the region of maximum convection there is a small daytime maximum in upper level cloud tops.

From the composite cloud cover and the mean temperature and moisture profiles of Reed et al. (1977), a wave composite depiction of radiative convergence profiles was calculated. The profiles are representative of a well-developed easterly wave in the GATE region. The results are not necessarily indicative of the radiative profiles of an easterly wave in other oceanic regions where the cloud structure may differ (e.g. western Atlantic tradewind region).

Zonal gradients of total tropospheric radiative convergence (TTC) are much smaller than meridional gradients. However, a plot of the vertical profiles across a zonal section of the wave composite reveals significant differences in the radiative convergence at specific levels, as much as 25 W m^{-2} (100 mb)$^{-1}$ (2.1°C/day). This may have special significance in light of the results of Albrecht and Cox (1975) which imply that zonal differences in radiative convergence between specific layers of the atmosphere affect the wave dynamics.

Meridional and zonal gradients in radiative convergence tend to be larger at night than during the day. The day-night difference in

the TTC meridional gradient north of the ITCZ is approximately 25 W m^{-2} (912 mb)$^{-1}$ (.23°C/day). The day-night difference south of the ITCZ is approximately 8 W m^{-2} (912 mb)$^{-1}$ (.1°C/day). Individual layers may differ by more than 20 W m^{-2} (100 mb)$^{-1}$ (1.7°C/day) between day and night radiative convergence profiles. The inclusion of aerosols reduces the daytime meridional gradient in radiative convergence below 500 mb thereby enhancing the difference between the day and night profiles. The aerosols will also increase the daytime zonal gradient in radiative convergence in specific parts of the composite model.

The results of the present study indicate three possible radiative induced mechanisms which might contribute to the observed cycle in mass convergence. They are:

1) A synoptic scale radiative induced low level pressure gradient at the ITCZ which is larger at night and is due to different radiative convergence profiles between the ITCZ and surrounding regions. Above 400 mb there exists an outward pressure gradient from the ITCZ during the night and a small inward pressure gradient is established during the day.

2) Mesoscale radiative convergence differences between clear and cluster regions as proposed by Gray and Jacobson (1977).

3) The night composite has a relative maximum cooing at approximately 400 mb and half a wavelength from the maximum convective heating. This relative maximum cooling is not shown in the day composite. According to Albrecht and Cox (1975) it is possible that this relative maximum cooling will increase the vertical motion of the cloud cluster during the night.

REFERENCES

Albrecht, B. A., and S. K. Cox, 1975: The large scale response of the tropical atmosphere to cloud modulated infrared heating. Jour. Atmos. Sci., 32, 16-24.

Arkell, R., and Michael Hudlow, 1977: GATE International Meteorological Radar Atlas. National Oceanic and Atmospheric Administration, Environmental Data Service, 222 pp.

Carlson, T. N., and J. M. Prospero, 1972: The large-scale movement of Saharan air outbreaks over the Northern Equatorial Atlantic. Jour. Appl. Meteor., 11, 283-297.

_____, and J. M. Prospero, 1977: Report of the U.S. GATE Central Program Workshop, NCAR, Boulder, CO., July 26 - August 12, 1977.

Cox, S. K., 1973: Infrared heating calculations with a water vapour pressure broadened continuum. Q.J.R.M.S., 99, 669-679.

_____, M. Polifka, K. Griffith, T. Rockwood, and D. Starr, 1976: Radiative transfer computational routines for atmospheric science applications. Colorado State University Atmospheric Science Research Report, 75 pp.

_____, and K. T. Griffith, 1978: Tropospheric radiative divergence during Phase III of the GARP Atlantic Tropical Experiment (GATE). Dept. Atmos. Sci. Paper #291, Colorado State University, Ft. Collins, CO., 166 pp.

_____, and K. T. Griffith, 1979a: Estimates of radiative divergence during Phase III of the GARP Atlantic Tropical Experiment, Part I. Methodology. Jour. Atmos. Sci., 36, 576-585.

_____, and K. T. Griffith, 1979b: Estimates of radiative divergence during Phase III of the GARP Atlantic Tropical Experiment, Part II. Analysis of Phase III results. Jour. Atmos. Sci., 36, 586-601.

Dewart, J. M., 1978: Diurnal variability in the GATE region. Dept. of Atmos. Sci. Paper #298, Colorado State University, Ft. Collins, CO., 80 pp.

Dopplick, T. G., 1972: Radiative heating of the global atmosphere. Jour. Atmos. Sci., 29, 1278-1294.

Fingerhut, W. A., 1978: A numerical model of a diurnally varying tropical cloud cluster disturbance. Mon. Wea. Rev., 106, 255-264.

Fischer, K., and H. Grassel, 1976: Absorption by airborne and deposited particles in the 8-13 micrometer range. Tellus, 5, 522-527.

REFERENCES (Continued)

Foltz, G. S., 1976: Diurnal variation of the tropospheric energy budget. Atmos. Sci. Paper #262, Colo. State Univ., Ft. Collins, CO., 140 pp.

Gray, W. M., and R. W. Jacobson Jr., 1977: Diurnal variation of deep cumulus convection. Mon. Wea. Rev., 105, 1171-1188.

_____, and Associates, 1977: Analysis of GATE rawinsonde and precipitation data and comparison with other tropical regions and weather systems. Report prepared for the GATE Workshop, Boulder, CO., July 25 - August 12.

Griffith, K. T., S. K. Cox and R. G. Knollenberg, 1980: Infrared radiative properties of tropical cirrus clouds inferred from aircraft measurements. Accepted for publication in the Jour. Atmos. Sci.

Gruber, A., 1976: An estimate of the daily variation of cloudiness over the GATE A/B area. Mon. Wea. Rev., 104, 1036-1039.

Haltiner, G. S., and F. L. Martin, 1957: Dynamical and physical meteorology, McGraw-Hill Book Company, Inc.

Holle, R. L., S. W. Leavitt, J. Simpson, R. Biondini, and J. W. Snow, 1977: Cloudiness from whole-sky pictures taken aboard four U.S. B-scale ships. Univ. of Virginia, Department of Environmental Sciences, 110 pp.

_____, Joanne Simpson and S. W. Leavitt, 1979: GATE B-scale cloudiness from whole-sky cameras on four U.S. ships. Mon. Wea. Rev., 197, 874-895.

Idso, S. B., 1974: Thermal blanketing: A case for aerosol-induced climatic interaction. Science, 186, 50-51.

Johnson, R. H., 1980: Diagnosis of convective and mesoscale motions during Phase III of GATE. Jour. Atmos. Sci., 37, April.

Kondratyev, K. Ya., and Associates, 1976: Aerosol in the GATE area and its radiative properties. Atmospheric Science Paper #247, Colorado State University, Ft. Collins, CO.

_____, R. M. Welch, O. B. Vasilyev, V. F. Zhvalev, L. S. Ivelv and V. F. Radionov: Calculations of free atmospheric shortwave spectral characteristics over the desert (from the CAENEX-70 data). Tellus, 31, 13-27.

Liou, K., and T. Sasamori, 1975: On the transfer of solar radiation in aerosol atmospheres. Jour. Atmos. Sci., 32, 2166-2177.

REFERENCES (Continued)

Manabe, S., and R. F. Strickler, 1964: Thermal equilibrium of the atmosphere with a convective adjustment. Jour. Atmos. Sci., 24, 361-385.

Mani, A., and V. Srinivasan, 1972: Airborne radiometer measurements of the effect of clouds and particulates on the terrestrial radiation flux. Proceedings International Radiation Symposium, Sendai, Japan.

McBride, J., and W. M. Gray, 1978: Mass divergence in tropical weather systems, Paper I: Diurnal variation, Paper II. Large-scale controls on convection. Dept. of Atmos. Sci. Paper #299, Colo. State Univ., Ft. Collins, CO.

McGarry, M., and R. J. Reed, 1978: Diurnal variations in convective activity and precipitation during Phases I and II of GATE. Mon. Wea. Rev., 106, 101-113.

Minnis, P., and S. K. Cox, 1978: Magnitude of the radiative effects of the Saharan dust layer. Atmos. Sci. Paper #283, Colo. State Univ., 111 pp, (NTIS #PB 286 835).

Paltridge, G. W., and C.M.R. Platt, 1973: Absorption and scatter of radiation by an aerosol layer in the free atmosphere. Jour. Atmos. Sci., 30, 734-737.

Patterson, E. M., and D. A. Gillette, 1977: Commonalities in measured size distributions for aerosols having a soil derived component. J. Geophys. Res., 82, 2074-2082.

_____, D. A. Gillette, and B. H. Stockton, 1977: Complex index of refraction between 300 and 700 nm for Saharan aerosols. J. Geophys. Res., 82, 3153-3161.

Payne, S., and M. M. McGarry, 1977: The relationship of satellite inferred convective activity to easterly waves over West Africa and the adjacent ocean during Phase III of GATE. Mon. Wea. Rev., 105, 413-420.

Prospero, J. M., and T. N. Carlson, 1972: Vertical and areal distribution of Saharan dust over the western equatorial North Atlantic Ocean. J. Geophys. Res., 77, 5255-5265.

_____, T. N. Carlson, D. Savoie, and R. T. Nees, 1976: Atmospheric turbidity measurements during GATE. Technical Report TR76-6, University of Miami, Florida.

Reed, R., D. C. Norquist, and E. E. Recker, 1977: The structure and properties of African wave disturbances as observed during Phase III of GATE. Mon. Wea. Rev., 105, 334-342.

REFERENCES (Continued)

Ruprecht, E., and W. M. Gray, 1976b: Analysis of satellite observed tropical cloud clusters, Paper II: Thermal, moisture and precipitation. Tellus, 28, 414-426.

Savoie, D., and J. M. Prospero, 1976: Saharan aerosol transport across the Atlantic Ocean: Characteristics of the input and the output. Bull. Am. Meteor. Soc., 57, 145.

Schubert, W. H., J. S. Wakefield, E. J. Steiner and S. K. Cox, 1977: Marine stratocumulus convection. Dept. of Atmos. Sci. Paper #273, Colo. State Univ., Ft. Collins, CO., 140 pp., (NTIS #PB 272 955).

Smith, E. A., and T. H. Vonder Haar, 1976: Hourly synchronous meteorological Satellite-1 (SMS-1) data collected during the GARP Atlantic Tropical Experiment (GATE). Earth located, edited data set. Atmospheric Science Research Report, Colo. State Univ., 180 pp.

_____, and T. H. Vonder Haar, 1976: Quantitative study of cloud conditions over the GATE using satellite data. Tenth Technical Conference on Hurricanes and Tropical Meteorology of the American Meteorological Society, July 6-9, 1976, Charlottesville, VA.

_____, 1977: Personal Communication.

Starr, D. O'C., 1976: The sensitivity of tropical radiative budgets to cloud distribution and the radiative properties of clouds. Atmos. Sci. Paper #254, Colo. State Univ., Ft. Collins, CO., 117 pp., (NTIS #PB 263 227).

Thompson, R. M. Jr., S. W. Payne, E.E. Recker and R. J. Reed, 1978: Structure and properties of synoptic-scale wave disturbances in the intertropical convergence zone of the Eastern Atlantic. Submitted for publication in Jour. Atmos. Sci.

Welch, R. M., and W. Zdunkowski, 1976: A radiation model of the polluted atmospheric bounday layer. Jour. Atmos. Sci., 33, 2170-2184.

_____, S. K. Cox and J. M. Davis, 1980: Solar radiation and clouds. Meteorological Monographs #39, 93 pp.

VI. APPENDICES

Appendix A

The mean cloud top distribution for 100 mb intervals as a function of wave category for night (Table A1) and day (Table A2) are given. Column 1 is the wave category or position. The first number corresponds to the row (Δ latitude 0 is row 4), the second represents the column. Thus, wave category 1-4 corresponds to Δ latitude +12 at the trough position. Columns 2-19 represent the areal percent coverage of cloud tops between the corresponding pressure intervals listed at the head of the column.

Appendix B

Table B1 shows the radiative convergence profiles in W m^{-2} per pressure interval derived from mean nighttime cloud distribution. Tables B2 and B3 list the shortwave and longwave components of the radiative convergence profiles for the daytime composite. The total daytime radiative convergence profiles are given in Table B4. The tables do not include the effects of aerosols (See Section 4.2.2). The first column gives the pressure interval of the corresponding row listed at the top of the column. Row 1 corresponds to latitude +12, Row 2 to latitude +8, and so on. The next eight columns represent the vertical profiles of the wave column listed at the top. Column 4 corresponds to the wave trough, column 8 to the ridge.

Appendix C

In this Appendix the shortwave clear region convergence profiles (W m^{-2} per pressure interval) are given in Table C1. Table C2

presents the SW convergence profiles for the aerosol regions of the wave. The first column gives the pressure interval of the corresponding row listed at the top of the column. Row 1 corresponds to Δ latitude +12, Row 2 to Δ latitude +8, and so on. The next eight columns represent the vertical profiles of the wave column listed at the top. Column 4 corresponds to the wave trough, column 8 to the ridge.

Appendix D

This Appendix lists the cloud top distribution and the longwave and shortwave radiative convergence profiles (W m^{-2} per pressure interval) as a function of wave column for the A/B and B-scale arrays. Tables D1 and D2 are the daytime and nighttime composites for the B-scale array respectively. The A/B-scale array composites are given in Tables D3 and D4. The first column gives the pressure interval of the corresponding row listed at the top of the column. Row 1 corresponds to Δ latitude +12, Row 2 to Δ latitude +8, and so on. The next eight columns represent the vertical profiles of the wave column listed at the top. Column 4 corresponds to the wave trough, column 8 to the ridge.

NIGHTTIME CLOUD TOP DISTRIBUTION

WAVE CATAGORY	CLEAR	900-950	800-900	700-800	600-700	500-600	400-500	300-400	200-300	100-200	NO. OF BOXES
1-1	0.0	0.0	23.3	46.5	17.8	9.9	2.5	0.0	0.0	0.0	11
1-2	0.0	.5	34.1	36.4	18.6	9.1	1.4	0.0	0.0	0.0	5
1-3	0.0	0.0	16.7	39.6	20.2	19.6	4.0	0.0	0.0	0.0	3
1-4	0.0	0.0	25.2	19.0	15.5	14.6	25.7	0.0	0.0	0.0	4
1-5	1.7	3.0	25.1	30.1	20.3	15.5	3.8	.6	0.0	0.0	5
1-6	34.9	11.7	27.2	6.6	10.0	9.6	0.0	0.0	0.0	0.0	4
1-7	51.1	10.8	17.9	11.7	6.0	2.2	.2	0.0	0.0	0.0	19
1-8	14.6	7.3	34.7	24.4	8.9	6.5	3.6	0.0	0.0	0.0	9
2-1	51.8	9.9	15.3	4.5	6.0	8.0	4.1	.3	.1	.1	69
2-2	40.9	10.6	18.7	8.9	7.3	7.1	4.9	.9	.4	.1	52
2-3	35.7	12.0	27.3	8.1	5.5	5.6	5.5	.1	.1	.2	40
2-4	46.2	9.9	20.8	7.2	5.9	7.4	1.6	.8	.0	0.0	38
2-5	57.9	8.1	7.5	2.8	5.4	9.2	7.2	1.5	.5	0.0	41
2-6	60.4	6.1	11.2	6.4	6.1	5.4	3.3	1.1	.0	.0	49
2-7	57.9	10.9	11.1	6.5	4.8	5.5	2.6	.8	0.0	0.0	89
2-8	59.5	7.8	16.2	7.4	4.6	3.9	.6	0.0	0.0	0.0	32
3-1	21.9	14.6	32.8	18.8	5.0	2.8	2.4	1.4	.3	0.0	107
3-2	17.6	11.2	30.9	23.3	5.4	4.8	3.5	2.6	.6	0.0	73
3-3	18.1	5.7	28.1	28.6	9.6	7.1	2.4	.2	0.0	0.0	52
3-4	14.9	5.0	26.7	20.9	10.3	11.3	7.3	2.4	.4	1.0	60
3-5	14.0	3.2	24.3	15.5	10.2	12.6	13.7	6.2	.3	.1	55
3-6	27.6	6.7	13.0	9.2	8.6	13.5	14.8	6.4	.1	.2	67
3-7	26.5	11.2	17.9	13.4	9.3	7.4	7.3	4.7	1.2	1.2	93
3-8	27.1	16.2	22.2	8.3	4.8	5.0	3.8	6.9	5.3	.4	53
4-1	31.2	13.4	16.2	9.0	5.7	5.1	3.1	4.0	4.1	6.3	125
4-2	15.6	14.5	21.6	11.7	8.2	7.0	3.2	6.1	8.0	3.9	88
4-3	7.1	7.7	18.9	13.6	8.7	10.7	7.9	7.9	7.5	9.9	48
4-4	13.1	9.8	18.1	9.4	6.6	7.7	8.8	10.9	9.0	6.6	65
4-5	17.0	6.9	12.8	8.0	6.6	14.3	19.4	9.8	2.7	.5	52
4-6	24.0	6.5	9.5	6.6	5.9	10.6	18.1	10.2	5.2	3.2	79
4-7	14.0	7.2	11.0	6.6	8.2	14.6	22.1	11.0	2.9	2.4	84
4-8	30.3	9.0	9.0	6.6	5.5	8.2	6.6	7.4	7.7	9.6	84
5-1	23.1	7.3	15.5	11.9	7.4	6.8	9.2	7.2	6.1	3.4	152
5-2	25.5	6.6	14.5	8.8	5.2	6.6	6.9	8.2	8.9	8.8	119
5-3	29.1	9.2	15.1	7.8	5.4	6.8	5.3	5.0	7.4	9.0	78
5-4	35.9	12.4	14.0	8.8	6.3	7.5	4.8	2.8	2.7	4.8	78
5-5	22.1	11.6	13.5	9.7	9.5	15.1	8.6	5.3	2.6	2.0	56
5-6	36.1	6.4	9.6	7.3	6.7	12.0	11.9	4.7	4.7	.6	79
5-7	18.7	7.1	10.9	9.9	9.3	13.7	19.7	5.0	4.0	1.9	84
5-8	20.6	13.6	10.9	8.8	7.0	7.9	11.6	7.2	6.6	5.6	91
6-1	34.1	11.4	18.6	11.6	5.7	7.6	5.8	3.2	1.7	.1	129
6-2	23.0	13.1	20.7	13.2	6.5	9.7	7.4	3.0	2.2	1.3	130
6-3	24.6	12.8	12.0	7.7	4.8	10.3	16.4	4.0	5.3	2.3	66
6-4	26.1	11.0	14.9	12.2	7.3	10.6	9.7	3.9	2.1	2.2	99
6-5	23.2	10.4	14.4	11.3	10.3	14.5	11.7	3.1	.8	.3	79
6-6	25.2	10.5	20.2	10.1	7.4	8.8	10.4	4.4	2.8	.3	67
6-7	33.5	12.0	25.2	10.9	4.1	3.6	2.4	2.8	3.4	1.8	87
6-8	29.7	12.6	21.9	11.2	7.0	7.3	5.6	2.2	1.5	1.1	102
7-1	50.6	21.7	19.9	4.4	1.4	.9	.7	.3	.0	0.0	120
7-2	34.1	26.2	18.2	6.7	4.4	4.0	3.0	3.2	.4	.0	111
7-3	51.2	20.6	11.2	3.8	3.4	3.5	5.4	.5	.6	.0	54
7-4	48.1	21.9	14.3	6.1	4.2	2.7	1.3	.6	.7	.3	104
7-5	38.1	22.7	19.9	9.0	5.1	3.1	.5	.5	.5	.7	70
7-6	48.2	27.7	15.0	3.6	1.6	1.7	.5	.5	.5	.4	60
7-7	54.2	19.3	23.4	2.1	.4	.3	.1	.1	.1	.0	92
7-8	41.5	20.5	30.3	3.7	1.5	1.0	.6	.4	.5	.1	92

Table A1. Nighttime mean cloud top distribution as a function of wave position. Column 1 is the wave category or position. The first number corresponds to the row, the second represents the wave column. Columns 2-19 represent the areal percent coverage of cloud tops between the corresponding pressure intervals listed at the head of the column. The last column lists the number of 1° boxes that comprised the wave category composite.

DAYTIME CLOUD TOP DISTRIBUTION

WAVE CATAGORY	CLEAR	900-950	800-900	700-800	600-700	500-600	400-500	300-400	200-300	100-200	NO. OF BOXES
1-1	18.1	15.2	34.2	14.6	7.6	5.1	5.2	0.0	0.0	0.0	1
1-2	0.0	.5	34.1	36.4	18.6	9.1	1.4	0.0	0.0	0.0	0
1-3	0.0	0.0	42.3	49.7	5.5	2.6	0.0	0.0	0.0	0.0	3
1-4	0.0	0.0	.7	93.3	5.6	.4	0.0	0.0	0.0	0.0	3
1-5	0.0	0.0	37.1	43.0	10.6	8.7	.7	0.0	0.0	0.0	5
1-6	61.0	13.0	17.8	6.6	1.6	0.0	0.0	0.0	0.0	0.0	6
1-7	74.3	4.5	7.4	8.4	4.6	1.0	0.0	0.0	0.0	0.0	12
1-8	51.3	9.6	17.7	15.4	4.4	1.2	.1	0.0	0.0	0.0	5
2-1	81.4	7.4	9.1	.9	.5	.5	.0	0.0	.1	.1	58
2-2	44.6	12.7	30.2	9.8	1.4	.9	.2	0.0	.1	.1	41
2-3	26.4	11.8	30.2	14.6	5.8	5.4	5.7	.0	0.0	.2	64
2-4	45.7	11.3	26.0	1.6	4.0	6.6	4.6	.1	.1	0.0	55
2-5	55.9	10.9	9.0	2.0	5.8	10.5	5.9	.0	0.0	0.0	38
2-6	75.8	12.6	5.8	2.0	1.2	1.6	.3	.4	.3	0.0	32
2-7	86.7	8.1	3.0	.7	.4	1.0	.2	0.0	0.0	0.0	60
2-8	94.1	2.1	.1	.4	.6	.8	1.0	.9	.1	0.0	38
3-1	23.5	7.2	48.5	13.1	3.3	1.9	1.5	.8	.3	0.0	107
3-2	11.1	7.2	31.8	35.8	7.9	5.6	.7	.2	0.0	0.0	73
3-3	14.1	5.2	31.2	31.3	6.5	6.0	2.8	1.3	1.5	0.0	95
3-4	18.3	3.9	20.5	20.1	11.2	9.1	6.8	4.5	3.8	1.8	87
3-5	25.2	9.3	18.9	11.0	9.1	11.8	6.1	3.9	3.4	1.5	61
3-6	25.5	9.3	17.9	14.2	11.0	11.3	8.0	1.8	1.0	0.0	60
3-7	23.6	8.9	29.4	9.8	7.1	8.4	5.1	3.5	4.0	.2	74
3-8	22.1	5.6	40.5	9.6	4.4	3.9	4.4	5.3	4.2	.1	54
4-1	24.0	12.9	20.7	10.6	7.3	6.9	5.4	4.4	5.0	2.7	126
4-2	7.5	13.0	24.6	12.6	6.9	9.6	8.0	5.7	5.7	6.3	105
4-3	13.6	8.6	16.7	9.3	6.9	8.2	6.0	6.9	11.0	12.8	76
4-4	26.7	12.0	12.9	9.0	6.9	7.8	9.6	8.6	5.1	1.4	78
4-5	33.3	13.8	11.1	8.2	6.0	5.6	9.0	6.1	4.4	2.3	46
4-6	27.3	10.9	12.7	9.4	8.5	13.2	12.8	4.0	1.3	.0	87
4-7	19.2	14.4	16.3	11.4	8.4	11.4	13.8	4.2	1.0	0.0	74
4-8	28.5	18.8	15.6	12.5	6.9	9.2	4.1	1.7	.6	.0	73
5-1	20.1	9.7	19.3	12.3	7.9	7.7	6.2	6.5	6.0	4.3	151
5-2	25.6	8.4	10.6	9.2	6.0	7.4	8.2	7.7	11.4	5.6	119
5-3	25.4	5.7	13.7	9.8	7.5	9.1	8.9	7.3	7.6	5.2	84
5-4	49.2	9.6	7.1	5.8	5.5	5.7	4.9	4.7	5.2	2.4	85
5-5	41.1	10.5	11.7	6.8	6.4	9.6	7.5	5.0	1.3	.3	61
5-6	37.9	13.9	13.4	9.6	5.7	6.7	6.9	3.9	2.0	.2	113
5-7	32.8	10.4	13.6	11.7	7.9	9.7	6.2	4.0	3.7	.2	82
5-8	19.7	17.4	18.3	12.7	7.8	7.6	5.1	5.4	3.9	2.2	81
6-1	44.7	15.6	15.0	6.2	4.0	4.1	2.9	2.9	3.4	1.3	158
6-2	32.4	14.4	19.1	8.9	6.0	9.3	5.2	3.1	1.7	0.0	117
6-3	29.4	13.0	17.5	11.0	9.0	10.1	5.3	2.2	2.4	.2	94
6-4	32.4	17.0	17.0	10.0	7.1	6.8	4.2	2.7	1.9	1.0	77
6-5	41.6	15.4	15.3	7.2	5.9	5.4	3.0	2.4	2.9	1.0	69
6-6	29.0	11.1	17.3	13.5	7.9	6.3	4.6	5.3	4.3	.6	97
6-7	32.9	14.2	15.3	11.9	6.4	7.0	3.9	3.7	4.0	.8	109
6-8	38.6	15.4	12.9	8.7	5.2	7.1	5.1	4.1	3.7	.9	96
7-1	39.6	37.2	15.2	3.2	1.1	1.3	1.0	.4	.9	.1	128
7-2	51.2	26.7	13.3	5.1	2.0	1.2	.4	.1	.1	0.0	105
7-3	42.7	26.3	13.3	7.0	3.9	4.0	1.4	.8	.5	.1	75
7-4	53.2	20.4	13.0	5.8	3.5	2.5	.9	.7	.0	0.0	64
7-5	59.6	20.5	9.8	4.5	1.2	1.1	.6	1.0	1.5	.2	71
7-6	46.5	26.7	14.3	5.1	2.4	1.6	.6	.2	.2	.1	75
7-7	50.3	23.4	17.9	4.7	.7	.7	.7	.4	.8	.6	108
7-8	40.7	30.6	23.7	3.0	.8	.6	.3	.1	.0	0.0	87

Table A2. Daytime mean cloud top distribution as a function of wave position. Column 1 is the wave category or position. The first number corresponds to the row, the second represents the wave column. Columns 2-19 represent the areal percent coverage of cloud tops between the corresponding pressure intervals listed at the head of the column. The last column lists the number of 1° boxes that comprised the wave category composite.

ROW 1	1	2	3	4	5	6	7	8
100	-1.73	-1.30	-4.14	-5.79	-3.96	-1.95	-3.22	-3.71
200	-19.96	-17.88	-15.96	-15.19	-15.24	-16.25	-17.96	-19.45
300	-22.71	-21.82	-21.63	-21.44	-21.36	-22.66	-24.36	-23.85
400	-18.78	-19.49	-20.01	-30.16	-20.23	-22.74	-21.34	-20.54
500	-19.95	-20.59	-27.73	-19.90	-26.07	-23.16	-17.97	-17.74
600	-25.31	-25.94	-25.09	-18.89	-28.04	-23.49	-23.48	-20.82
700	-68.09	-58.10	-60.38	-34.47	-49.23	-24.27	-32.34	-43.51
800	-55.55	-69.92	-46.95	-61.12	-54.73	-52.11	-45.25	-63.64
900	-9.69	-11.96	-16.03	-14.40	-16.91	-39.14	-41.57	-22.84
1000	2.16	1.91	1.34	.72	-.03	-3.82	-3.87	-3.42
1012 TOTAL	-239.31	-245.10	-236.59	-220.63	-235.41	-229.59	-231.34	-235.67

ROW 2	1	2	3	4	5	6	7	8
100	-3.90	-1.78	-1.08	-1.69	-1.91	-1.49	-2.98	-4.55
200	-18.01	-17.46	-15.27	-14.47	-15.94	-17.39	-18.08	-17.76
300	-22.31	-21.82	-21.90	-24.01	-25.04	-23.76	-22.59	-22.32
400	-19.33	-22.40	-25.98	-22.85	-26.10	-24.10	-22.41	-18.14
500	-22.19	-20.99	-21.21	-24.47	-23.47	-20.38	-20.94	-20.87
600	-22.26	-20.86	-19.50	-23.44	-22.12	-21.65	-19.17	-22.17
700	-20.96	-28.30	-27.29	-24.83	-21.42	-29.54	-27.88	-25.11
800	-35.81	-45.39	-54.81	-40.80	-28.03	-39.77	-41.76	-38.54
900	-43.02	-38.71	-40.52	-42.72	-42.58	-36.32	-41.04	-49.36
1000	-6.87	-4.48	-3.86	-6.38	-7.80	-5.73	-5.01	-6.74
1012 TOTAL	-214.65	-222.19	-231.42	-225.47	-213.99	-220.13	-221.85	-220.55

ROW 3	1	2	3	4	5	6	7	8
100	-.96	-.96	-.92	-1.40	-1.06	-1.23	-1.72	-1.32
200	-16.17	-16.78	-16.77	-17.28	-17.49	-16.39	-15.46	-17.03
300	-22.26	-23.08	-23.88	-26.22	-28.37	-27.81	-25.99	-25.89
400	-23.55	-22.54	-21.26	-25.28	-30.86	-31.88	-25.69	-22.45
500	-21.41	-22.27	-24.10	-25.53	-25.31	-25.87	-22.16	-20.18
600	-24.34	-22.87	-27.08	-26.35	-25.49	-23.85	-26.79	-22.21
700	-42.71	-43.67	-47.11	-38.07	-33.86	-30.48	-36.88	-32.47
800	-50.91	-48.01	-42.06	-36.18	-30.68	-29.49	-36.25	-44.09
900	-28.41	-28.80	-26.16	-22.97	-21.43	-25.76	-26.69	-32.34
1000	-5.91	-5.44	-5.36	-5.63	-6.37	-6.97	-6.47	-6.01
1012 TOTAL	-236.23	-234.39	-234.69	-224.91	-220.91	-219.74	-224.12	-223.99

ROW 4	1	2	3	4	5	6	7	8
100	-3.64	-2.45	-4.95	-3.30	-.48	-1.86	-1.63	-5.24
200	-17.25	-19.28	-18.35	-19.95	-18.65	-18.25	-16.42	-16.97
300	-24.01	-24.44	-25.19	-28.93	-31.62	-30.65	-31.02	-26.00
400	-21.18	-19.53	-23.81	-26.44	-38.47	-35.53	-39.03	-24.19
500	-23.09	-24.08	-26.14	-24.90	-29.77	-24.16	-26.12	-23.46
600	-26.34	-26.68	-23.43	-23.76	-22.64	-21.50	-20.76	-22.27
700	-33.50	-33.10	-27.17	-23.86	-22.13	-23.17	-21.07	-25.80
800	-33.20	-32.89	-22.34	-19.29	-15.91	-17.12	-17.97	-23.20
900	-17.18	-14.80	-10.70	-11.63	-13.97	-15.66	-13.73	-17.69
1000	-5.72	-5.56	-5.75	-6.22	-6.66	-6.86	-6.57	-6.16
1012 TOTAL	-205.09	-202.81	-187.84	-188.28	-200.02	-194.76	-194.31	-190.98

ROW 5	1	2	3	4	5	6	7	8
100	-2.75	-5.20	-4.91	-2.75	-1.47	-.97	-1.68	-3.71
200	-17.41	-18.65	-18.30	-16.44	-15.27	-14.65	-14.01	-15.68
300	-24.90	-25.46	-24.52	-24.02	-24.97	-23.53	-23.79	-24.23
400	-28.58	-24.21	-23.87	-26.66	-32.45	-37.80	-43.60	-31.74
500	-27.08	-24.31	-25.84	-28.47	-33.59	-29.86	-29.04	-24.53
600	-25.27	-23.26	-25.62	-28.76	-26.98	-24.18	-23.83	-23.80
700	-30.09	-25.99	-26.27	-30.27	-27.97	-27.98	-25.81	-27.66
800	-24.35	-21.66	-20.72	-22.99	-21.35	-23.84	-19.71	-23.38
900	-11.35	-11.50	-12.94	-15.30	-14.73	-18.07	-12.84	-15.00
1000	-5.92	-6.13	-6.59	-6.79	-6.69	-6.86	-6.72	-6.29
1012 TOTAL	-197.69	-186.34	-189.58	-202.45	-205.47	-207.75	-201.02	-196.02

Table B1. Continued on next page.

ROW 6	1	2	3	4	5	6	7	8
100	-1.23	-1.59	-2.03	-1.96	-1.14	-1.31	-2.24	-1.86
200	-15.86	-16.50	-17.49	-16.07	-15.88	-16.34	-15.78	-14.96
300	-22.41	-23.22	-24.97	-24.67	-22.70	-22.90	-22.43	-22.46
400	-29.18	-29.29	-35.03	-30.68	-33.46	-30.63	-23.59	-28.46
500	-29.10	-29.93	-26.20	-27.90	-31.68	-26.72	-24.08	-27.69
600	-27.78	-27.88	-22.20	-25.46	-27.44	-26.70	-26.27	-27.87
700	-32.22	-32.52	-26.84	-31.82	-29.45	-31.86	-37.51	-33.60
800	-27.83	-26.15	-22.42	-24.03	-23.09	-29.82	-37.38	-31.84
900	-16.16	-13.25	-17.30	-17.10	-17.19	-16.06	-15.99	-16.43
1000	-7.16	-6.87	-7.27	-7.56	-7.56	-7.21	-7.07	-7.13
1012								
TOTAL	-208.93	-207.20	-201.74	-207.25	-209.59	-209.54	-212.34	-212.30

ROW 7	1	2	3	4	5	6	7	8
100	-1.15	-1.10	-1.18	-1.45	-1.53	-1.24	-.99	-1.12
200	-14.02	-15.11	-15.41	-15.20	-14.45	-13.83	-13.29	-13.54
300	-20.59	-21.98	-19.91	-20.23	-20.90	-20.34	-19.30	-19.92
400	-23.20	-24.86	-27.50	-23.38	-22.98	-23.66	-23.39	-22.89
500	-22.40	-23.92	-24.30	-24.02	-23.16	-22.46	-23.64	-24.07
600	-23.26	-24.63	-26.88	-29.39	-27.53	-23.99	-25.74	-26.51
700	-28.75	-28.41	-27.69	-32.49	-35.51	-31.07	-30.36	-30.00
800	-40.34	-35.08	-29.68	-32.14	-37.54	-39.29	-42.80	-44.69
900	-33.44	-30.08	-33.17	-31.06	-28.42	-35.97	-31.35	-26.97
1000	-8.42	-7.85	-8.51	-8.51	-8.28	-8.50	-8.73	-8.33
1012								
TOTAL	-215.96	-213.02	-214.24	-217.86	-220.29	-220.36	-219.60	-218.04

Table B1. Mean nighttime radiative convergence profiles in W m^{-2} per pressure interval.

ROW 1	1	2	3	4	5	6	7	8
100	3.41	3.45	3.42	3.42	3.43	3.34	3.33	3.36
200	10.40	9.11	8.70	8.75	8.58	9.10	10.65	11.34
300	20.76	17.84	17.47	18.27	17.13	16.64	19.64	21.71
400	19.53	19.92	19.81	16.98	18.20	22.16	21.80	18.41
500	17.70	22.14	19.79	16.79	21.17	20.74	20.58	17.78
600	18.09	22.40	18.37	18.85	20.51	16.87	18.04	18.37
700	17.16	21.15	22.87	31.23	21.86	13.91	14.55	17.71
800	16.09	16.28	23.42	18.42	19.27	14.12	12.32	14.31
900	10.27	3.55	3.37	.06	2.80	14.32	12.77	11.06
1000	.83	.00	.00	.00	.00	2.49	2.72	1.90
1012								
TOTAL	133.23	135.85	137.22	132.78	132.95	133.69	136.38	135.95

ROW 2	1	2	3	4	5	6	7	8
100	3.36	3.41	3.48	3.37	3.37	3.32	3.31	3.30
200	10.76	9.27	8.24	8.50	8.75	8.87	9.69	10.90
300	19.02	17.17	16.71	18.17	18.71	17.90	18.27	19.75
400	17.73	19.34	22.43	21.43	21.94	21.42	21.11	18.92
500	18.07	19.15	21.61	22.12	22.80	19.15	18.90	18.23
600	16.70	17.48	18.44	18.13	17.71	16.08	15.50	15.85
700	12.63	16.44	16.40	12.77	12.04	14.98	13.89	11.87
800	12.21	18.34	16.22	13.82	10.53	14.28	13.49	10.38
900	13.85	12.40	10.07	12.11	11.44	13.05	12.96	13.06
1000	3.34	1.77	1.07	1.84	2.13	2.63	3.07	3.69
1012								
TOTAL	127.68	134.77	134.67	132.26	129.40	131.70	130.19	125.95

ROW 3	1	2	3	4	5	6	7	8
100	3.39	3.42	3.42	4.37	4.19	3.42	3.52	3.45
200	9.57	9.83	10.71	12.09	11.87	10.10	10.98	11.09
300	17.15	17.42	19.51	21.35	21.27	20.36	19.36	19.05
400	20.83	19.93	19.56	20.19	20.79	22.36	20.36	20.08
500	19.96	21.41	20.25	19.47	20.57	21.21	19.45	18.24
600	18.13	20.12	18.83	18.08	17.13	18.31	16.86	16.36
700	18.34	22.25	20.03	15.81	14.48	16.42	15.65	15.95
800	19.68	18.28	17.99	12.45	12.53	13.03	14.67	16.71
900	13.70	7.82	7.15	6.46	8.43	8.58	10.81	11.46
1000	.88	.47	.56	.65	.86	.88	.85	.79
1012								
TOTAL	141.64	140.94	138.01	130.91	132.12	134.67	132.51	133.19

ROW 4	1	2	3	4	5	6	7	8
100	4.87	6.83	10.33	4.11	4.58	3.45	3.44	3.41
200	12.39	13.21	15.68	13.23	12.70	10.74	9.86	9.37
300	20.64	19.89	18.05	23.26	22.95	22.82	22.10	21.00
400	19.61	18.26	16.28	22.70	23.62	26.48	26.76	23.70
500	18.57	17.94	15.87	19.21	18.98	22.86	22.05	22.74
600	17.11	15.43	13.37	15.27	15.34	16.07	16.20	19.08
700	15.25	14.13	11.14	12.50	12.97	12.76	13.54	16.34
800	13.34	12.94	9.36	10.09	10.79	10.26	11.11	13.51
900	9.55	7.67	6.71	8.27	8.90	7.97	8.58	10.69
1000	.84	.33	.49	.86	1.03	.86	.68	1.01
1012								
TOTAL	132.15	126.62	117.28	129.50	131.87	134.26	134.33	140.83

ROW 5	1	2	3	4	5	6	7	8
100	5.62	6.32	6.08	4.65	3.56	3.50	3.52	4.53
200	12.71	15.99	14.33	12.58	9.59	8.98	9.76	10.67
300	19.46	20.20	21.53	20.34	18.95	15.92	15.94	17.95
400	20.33	19.13	20.51	21.54	25.37	26.62	25.04	21.99
500	19.06	16.88	18.43	19.40	22.74	22.45	22.96	20.78
600	16.38	13.63	14.83	16.03	16.47	16.67	17.30	17.45
700	14.38	11.72	11.89	13.31	13.60	15.05	14.98	15.55
800	11.80	9.31	9.80	11.21	11.90	13.37	12.35	13.44
900	8.08	6.87	6.54	9.51	9.65	10.39	9.06	9.50
1000	.67	.81	.78	1.50	1.29	1.25	1.09	.74
1012								
TOTAL	128.49	120.86	124.72	130.06	133.13	134.20	132.00	132.61

Table B2. Continued on next page.

ROW 6	1	2	3	4	5	6	7	8
100	4.07	3.41	3.51	3.89	3.88	3.72	3.80	3.86
200	10.71	10.30	10.89	10.62	10.99	11.50	11.11	10.69
300	17.30	18.92	19.71	19.42	17.46	18.08	17.98	18.14
400	20.55	22.21	22.67	22.38	21.57	20.64	20.38	20.94
500	20.35	22.52	22.10	20.47	20.23	19.57	19.78	20.10
600	17.45	17.89	18.34	17.36	17.14	17.22	17.08	16.59
700	14.94	14.82	15.22	15.75	15.29	16.02	16.16	14.40
800	13.73	13.48	13.38	13.99	14.09	13.47	13.87	12.94
900	11.87	10.66	9.30	11.07	11.83	9.38	10.39	10.98
1000	1.57	1.13	1.00	1.14	1.45	1.02	1.17	1.38
1012								
TOTAL	132.52	135.38	136.14	136.09	133.93	130.62	131.73	130.00

ROW 7	1	2	3	4	5	6	7	8
100	3.43	3.35	3.41	3.35	3.46	3.40	3.64	3.36
200	9.17	9.26	9.49	9.01	9.19	8.17	8.30	8.19
300	15.53	15.47	15.88	16.23	15.92	15.04	14.53	15.26
400	19.97	20.56	20.01	19.14	19.36	20.35	19.22	18.92
500	18.78	19.31	20.88	20.05	18.12	18.94	19.23	19.49
600	16.27	16.58	18.34	18.77	16.40	17.07	17.61	18.19
700	15.52	15.70	15.97	16.65	16.44	17.03	16.90	16.68
800	16.89	16.36	15.03	15.53	16.25	17.55	17.50	18.00
900	16.99	15.77	14.24	14.35	15.05	15.71	15.34	16.97
1000	1.78	2.12	1.74	2.04	2.29	1.90	2.02	1.75
1012								
TOTAL	134.34	134.48	134.98	135.12	132.49	135.16	134.28	136.81

Table B2. Mean daytime shortwave component of the radiative convergence profiles in W m^{-2} per pressure interval.

ROW 1	1	2	3	4	5	6	7	8
100	-1.91	-1.30	-4.13	-5.72	-3.54	-2.01	-3.26	-3.79
200	-19.60	-17.88	-15.85	-14.98	-15.18	-16.19	-17.94	-19.38
300	-22.52	-21.82	-21.26	-20.66	-20.92	-22.52	-24.32	-23.60
400	-20.13	-19.49	-16.96	-14.49	-18.05	-22.33	-21.10	-17.95
500	-15.36	-20.59	-16.36	-14.31	-21.57	-16.18	-17.07	-14.56
600	-16.50	-25.94	-15.82	-17.15	-21.07	-18.97	-22.64	-19.28
700	-34.90	-58.10	-77.26	-136.17	-68.08	-26.96	-29.84	-37.65
800	-75.07	-69.92	-82.05	-25.77	-71.07	-46.21	-38.92	-52.67
900	-33.04	-11.96	-10.39	-11.17	-11.79	-50.43	-48.24	-37.09
1000	1.53	1.91	2.52	2.74	.70	-5.05	-5.06	-.99
1012								
TOTAL	-237.41	-245.10	-257.56	-257.68	-250.57	-226.87	-228.39	-226.97

ROW 2	1	2	3	4	5	6	7	8
100	-3.93	-1.81	-1.05	-1.49	-1.49	-1.54	-3.03	-4.61
200	-17.90	-17.26	-15.24	-14.48	-15.74	-17.45	-18.01	-17.78
300	-21.93	-21.22	-21.92	-23.69	-24.29	-23.16	-22.04	-22.65
400	-16.34	-19.22	-26.17	-24.98	-25.55	-21.86	-20.66	-17.95
500	-17.15	-17.43	-21.10	-23.13	-25.18	-17.98	-17.95	-17.85
600	-20.00	-18.31	-19.96	-21.51	-22.77	-18.82	-16.77	-18.90
700	-19.67	-32.59	-33.96	-19.61	-20.84	-28.17	-24.51	-18.67
800	-32.63	-59.34	-55.96	-46.66	-29.06	-40.25	-39.44	-25.37
900	-49.06	-39.47	-38.07	-43.76	-43.62	-42.12	-44.89	-50.41
1000	-8.03	-4.13	-3.44	-6.36	-7.65	-5.91	-5.76	-8.58
1012								
TOTAL	-206.63	-230.78	-236.88	-225.68	-216.80	-217.24	-213.07	-202.78

ROW 3	1	2	3	4	5	6	7	8
100	-.95	-.91	-.93	-1.87	-1.83	-1.15	-1.25	-1.08
200	-16.15	-16.56	-17.28	-18.36	-18.29	-16.60	-16.53	-16.72
300	-21.88	-21.82	-24.27	-26.74	-26.16	-24.97	-25.04	-25.19
400	-22.92	-21.16	-21.06	-23.79	-24.60	-27.32	-23.97	-23.51
500	-20.91	-24.26	-22.68	-22.73	-25.61	-26.23	-23.36	-19.74
600	-23.32	-26.15	-24.32	-26.45	-25.99	-28.81	-25.00	-22.67
700	-38.76	-55.70	-49.95	-36.35	-32.45	-37.32	-34.91	-34.78
800	-63.93	-44.84	-44.06	-31.86	-32.45	-32.51	-44.74	-54.98
900	-24.19	-22.57	-24.17	-24.24	-25.03	-24.42	-24.51	-24.84
1000	-5.52	-5.07	-5.17	-5.81	-6.49	-6.78	-6.37	-5.81
1012								
TOTAL	-238.53	-239.03	-233.90	-218.19	-218.99	-226.11	-225.66	-229.32

ROW 4	1	2	3	4	5	6	7	8
100	-2.00	-3.49	-6.33	-.94	-1.36	-.36	-.50	-.88
200	-18.15	-18.15	-19.00	-19.25	-18.91	-17.14	-15.89	-15.61
300	-24.84	-24.28	-23.56	-29.07	-28.45	-27.92	-27.44	-25.46
400	-23.50	-23.58	-21.30	-29.39	-29.96	-34.37	-34.94	-26.86
500	-24.92	-25.32	-23.35	-27.28	-26.18	-30.70	-28.28	-29.76
600	-27.22	-23.63	-22.01	-26.53	-27.80	-26.89	-26.31	-30.38
700	-33.59	-31.85	-24.73	-26.29	-27.68	-27.93	-30.14	-34.97
800	-32.54	-31.57	-23.44	-20.68	-19.57	-20.36	-24.14	-29.38
900	-15.39	-11.75	-12.80	-15.31	-16.10	-16.15	-14.86	-18.69
1000	-5.68	-5.46	-5.81	-6.32	-6.57	-6.78	-6.42	-6.00
1012								
TOTAL	-207.51	-199.08	-182.33	-201.07	-202.57	-208.61	-208.91	-217.80

ROW 5	1	2	3	4	5	6	7	8
100	-3.13	-3.71	-3.15	-1.74	-.71	-.75	-.90	-2.01
200	-17.22	-20.08	-19.06	-17.72	-15.01	-13.67	-14.06	-15.16
300	-24.28	-25.39	-26.67	-25.23	-25.13	-23.28	-23.26	-23.90
400	-26.05	-25.64	-27.17	-26.23	-32.06	-34.48	-32.73	-27.92
500	-26.92	-25.03	-27.17	-26.51	-29.95	-27.71	-29.95	-27.69
600	-26.79	-23.64	-25.91	-28.29	-27.15	-26.74	-27.53	-27.94
700	-31.43	-25.85	-25.37	-28.94	-30.25	-33.97	-33.45	-34.48
800	-26.33	-20.33	-18.17	-22.46	-25.86	-29.02	-26.84	-28.78
900	-10.51	-12.66	-12.19	-18.57	-18.51	-19.06	-16.32	-14.52
1000	-5.84	-6.16	-6.66	-6.97	-6.93	-6.73	-6.71	-6.15
1012								
TOTAL	-198.49	-188.50	-191.51	-202.67	-211.47	-215.42	-211.75	-208.57

Table B3. Continued on next page.

ROW 6	1	2	3	4	5	6	7	8
100	-1.89	-.99	-1.01	-1.44	-1.55	-1.49	-1.77	-1.85
200	-16.26	-16.51	-16.71	-16.12	-16.39	-16.80	-16.18	-15.80
300	-21.75	-23.49	-24.44	-24.04	-21.68	-23.11	-23.08	-23.29
400	-26.13	-27.67	-27.22	-26.57	-25.68	-25.34	-24.83	-27.27
500	-25.93	-30.49	-30.16	-26.42	-25.37	-25.41	-26.57	-26.86
600	-27.44	-28.43	-29.71	-27.98	-27.43	-28.50	-27.13	-25.64
700	-29.97	-30.94	-32.57	-33.82	-32.23	-35.83	-35.78	-29.88
800	-29.77	-28.36	-26.82	-29.66	-31.72	-28.77	-30.48	-29.53
900	-21.87	-16.99	-17.13	-19.68	-23.02	-17.02	-17.87	-21.70
1000	-7.32	-7.03	-7.21	-7.53	-7.71	-7.23	-7.14	-7.35
1012 TOTAL	-208.31	-210.93	-212.98	-213.25	-212.78	-209.50	-210.82	-209.18

ROW 7	1	2	3	4	5	6	7	8
100	-1.23	-1.12	-1.20	-1.31	-1.40	-1.08	-1.26	-1.10
200	-14.26	-14.91	-15.37	-15.03	-14.80	-13.77	-13.43	-13.36
300	-20.55	-20.14	-20.05	-20.43	-21.14	-20.28	-19.32	-19.82
400	-23.27	-23.39	-24.11	-23.17	-22.82	-23.97	-23.64	-22.76
500	-22.54	-22.52	-25.74	-24.02	-20.90	-22.51	-23.64	-24.17
600	-22.69	-23.88	-28.08	-29.00	-23.84	-24.71	-25.54	-26.06
700	-27.36	-29.08	-31.20	-32.73	-32.50	-32.84	-32.13	-29.75
800	-37.80	-35.66	-30.66	-32.06	-35.13	-38.26	-37.82	-41.77
900	-39.87	-37.92	-32.27	-32.21	-36.39	-35.72	-32.51	-33.36
1000	-7.98	-8.27	-8.16	-8.65	-8.88	-8.44	-8.62	-8.23
1012 TOTAL	-217.94	-216.89	-216.85	-218.60	-217.91	-221.57	-217.92	-220.37

Table B3. Mean daytime infrared component of the radiative convergence profiles in W m^{-2} per pressure interval.

ROW 1	1	2	3	4	5	6	7	8
100	1.80	2.15	-.71	-2.30	-.10	1.32	.07	-.43
200	-9.20	-8.77	-7.15	-6.23	-6.60	-7.10	-7.30	-8.04
300	-1.76	-3.98	-3.79	-2.39	-3.79	-5.88	-4.68	-1.90
400	-1.90	.43	2.85	2.49	.14	-.17	.70	.46
500	2.34	1.55	3.43	2.48	-.40	4.56	3.51	3.22
600	1.58	-3.54	2.55	1.70	-.56	-2.09	-4.60	-.91
700	-17.74	-36.94	-54.38	-104.94	-46.22	-13.05	-15.29	-19.94
800	-58.99	-53.64	-58.64	-7.35	-51.80	-32.09	-26.60	-38.36
900	-22.77	-8.41	-7.02	-11.11	-8.99	-36.11	-35.47	-26.03
1000	2.35	1.91	2.52	2.74	.70	-2.56	-2.35	.91
1012								
TOTAL	-104.18	-109.25	-120.34	-124.90	-117.62	-93.18	-92.01	-91.02

ROW 2	1	2	3	4	5	6	7	8
100	-.56	1.60	2.43	1.88	1.87	1.79	.28	-1.31
200	-7.14	-7.99	-7.00	-5.97	-6.99	-8.58	-8.32	-6.89
300	-2.91	-4.05	-5.21	-5.52	-5.58	-5.26	-3.77	-2.90
400	1.40	.12	-3.74	-3.55	-3.62	-.44	.44	.98
500	.92	1.71	.51	-1.02	-2.38	1.18	.95	.37
600	-3.30	-.83	-1.53	-3.38	-5.07	-2.73	-1.27	-3.05
700	-7.03	-16.15	-17.56	-6.84	-8.80	-13.19	-10.62	-6.80
800	-20.43	-41.00	-39.74	-32.85	-19.14	-25.97	-25.95	-14.99
900	-35.21	-27.07	-28.00	-31.65	-32.18	-29.07	-31.93	-37.35
1000	-4.69	-2.36	-2.37	-4.52	-5.51	-3.27	-2.69	-4.88
1012								
TOTAL	-78.95	-96.01	-102.21	-93.42	-87.40	-85.55	-82.88	-76.83

ROW 3	1	2	3	4	5	6	7	8
100	2.44	2.51	2.49	2.50	2.36	2.28	2.28	2.38
200	-6.57	-6.73	-6.58	-6.27	-6.42	-6.50	-5.54	-5.63
300	-4.73	-4.39	-4.75	-5.39	-4.89	-4.60	-5.68	-6.15
400	-2.09	-1.24	-1.51	-3.60	-3.81	-4.96	-3.61	-3.43
500	-.94	-2.85	-2.43	-3.26	-5.24	-5.02	-3.91	-1.49
600	-5.19	-6.03	-5.50	-8.37	-8.76	-10.50	-8.13	-6.31
700	-20.42	-33.45	-29.91	-20.53	-17.97	-20.91	-19.27	-18.83
800	-44.25	-26.55	-26.07	-19.41	-19.91	-19.48	-30.07	-38.27
900	-10.49	-14.75	-17.01	-17.78	-16.59	-15.84	-13.70	-13.38
1000	-4.64	-4.60	-4.61	-5.16	-5.63	-5.90	-5.52	-5.01
1012								
TOTAL	-96.88	-98.09	-95.88	-87.28	-86.87	-91.45	-93.15	-96.13

ROW 4	1	2	3	4	5	6	7	8
100	2.87	3.34	4.00	3.17	3.23	3.09	2.94	2.74
200	-5.76	-4.94	-3.32	-6.02	-6.21	-6.40	-6.03	-6.24
300	-4.40	-4.39	-5.51	-5.82	-5.90	-5.11	-5.35	-4.46
400	-3.89	-5.32	-5.82	-6.69	-6.34	-7.89	-8.18	-3.17
500	-6.05	-7.39	-7.48	-8.08	-7.20	-7.84	-6.22	-7.02
600	-10.12	-8.20	-8.63	-11.26	-12.46	-10.82	-10.10	-11.30
700	-18.34	-17.72	-13.60	-13.79	-14.71	-15.17	-16.61	-18.63
800	-19.20	-18.63	-14.08	-10.58	-8.79	-10.10	-13.02	-15.87
900	-5.84	-4.09	-6.09	-7.04	-7.20	-8.18	-6.28	-8.01
1000	-4.84	-5.12	-5.33	-5.46	-5.53	-5.92	-5.73	-5.00
1012								
TOTAL	-75.36	-72.46	-65.05	-71.57	-70.70	-74.34	-74.58	-76.97

ROW 5	1	2	3	4	5	6	7	8
100	2.49	2.61	2.93	2.90	2.85	2.75	2.63	2.52
200	-4.50	-4.09	-4.73	-5.14	-5.42	-4.69	-4.29	-4.49
300	-4.81	-5.19	-5.14	-4.90	-6.17	-7.36	-7.32	-5.95
400	-5.72	-6.52	-6.66	-4.70	-6.69	-7.86	-7.69	-5.93
500	-7.86	-8.15	-8.74	-7.11	-7.21	-5.26	-6.99	-6.91
600	-10.42	-10.01	-11.08	-12.26	-10.68	-10.07	-10.23	-10.49
700	-17.05	-14.13	-13.48	-15.63	-16.64	-18.92	-18.47	-18.93
800	-14.53	-11.02	-8.36	-11.25	-13.96	-15.65	-14.49	-15.35
900	-2.43	-5.79	-5.66	-9.06	-8.87	-8.67	-7.27	-5.02
1000	-5.17	-5.36	-5.88	-5.47	-5.53	-5.48	-5.62	-5.61
1012								
TOTAL	-70.01	-67.63	-66.79	-72.61	-78.33	-81.22	-79.75	-75.96

Table B4. Continued on next page.

ROW 6	1	2	3	4	5	6	7	8
100	2.18	2.41	2.49	2.45	2.33	2.23	2.03	2.01
200	-5.93	-6.21	-5.81	-5.50	-5.40	-5.30	-5.07	-5.10
300	-4.45	-4.58	-4.72	-4.62	-4.22	-5.03	-5.11	-5.15
400	-5.59	-5.46	-4.54	-4.19	-4.11	-4.09	-4.45	-6.33
500	-5.58	-7.97	-8.06	-5.95	-5.15	-5.04	-6.79	-6.76
600	-10.00	-10.56	-11.37	-10.62	-10.28	-11.28	-10.04	-9.06
700	-15.03	-16.12	-17.35	-18.07	-16.94	-19.81	-19.62	-15.48
800	-16.04	-14.90	-13.44	-15.67	-17.82	-15.30	-16.60	-16.59
900	-10.01	-6.30	-7.83	-8.61	-11.19	-7.04	-7.48	-10.72
1000	-5.75	-5.90	-6.21	-6.40	-6.25	-6.21	-5.96	-5.97
1012								
TOTAL	-75.79	-75.55	-76.85	-77.17	-78.85	-78.88	-79.10	-79.17

ROW 7	1	2	3	4	5	6	7	8
100	2.20	2.23	2.21	2.04	2.06	2.31	2.38	2.26
200	-5.09	-5.64	-5.87	-6.02	-5.61	-5.60	-5.13	-5.17
300	-5.02	-4.67	-4.17	-4.20	-5.22	-5.24	-4.79	-4.56
400	-3.30	-2.83	-4.10	-4.03	-3.45	-3.81	-4.42	-3.84
500	-3.76	-3.21	-4.86	-3.97	-2.78	-3.96	-4.41	-4.68
600	-6.42	-7.30	-9.74	-10.23	-7.45	-7.63	-7.94	-7.86
700	-11.84	-13.39	-15.23	-16.08	-16.07	-15.81	-15.23	-13.07
800	-20.91	-19.30	-15.64	-16.53	-18.88	-20.71	-20.32	-23.77
900	-22.88	-22.15	-18.04	-17.86	-21.34	-20.01	-17.17	-16.38
1000	-6.20	-6.16	-6.43	-6.61	-6.99	-6.54	-6.60	-6.48
1012								
TOTAL	-83.20	-82.42	-81.87	-83.48	-85.33	-86.41	-83.64	-83.56

Table B4. Mean daytime radiative convergence profiles in W m^{-2} per pressure interval.

ROW 1	1	2	3	4	5	6	7	8
100	3.29	3.29	3.29	3.29	3.29	3.29	3.29	3.29
200	10.26	8.92	8.52	8.52	8.39	9.04	10.60	11.26
300	20.44	17.50	17.21	18.02	16.82	16.54	19.56	21.57
400	16.38	18.75	19.21	16.34	17.31	21.96	21.63	18.09
500	15.29	17.49	17.60	15.18	16.80	20.38	19.91	16.82
600	15.75	14.95	14.49	14.64	15.28	15.77	16.11	16.18
700	13.96	12.00	11.25	11.94	11.98	11.52	12.11	13.31
800	11.88	12.26	11.81	10.58	10.07	10.87	11.79	11.53
900	12.22	15.85	16.25	12.09	11.02	14.40	14.54	12.26
1000	3.93	4.28	4.45	4.76	4.57	3.92	3.41	3.56
1012								
TOTAL	122.99	125.28	124.09	115.36	115.53	127.70	132.75	127.88

ROW 2	1	2	3	4	5	6	7	8
100	3.29	3.29	3.29	3.29	3.29	3.29	3.29	3.29
200	10.71	9.17	8.11	8.39	8.65	8.65	9.67	10.82
300	19.00	17.06	16.42	17.89	18.43	17.75	18.23	19.38
400	17.65	19.03	20.39	19.76	19.85	21.34	20.97	18.77
500	17.79	18.35	19.62	19.91	19.17	18.55	18.43	18.17
600	16.31	16.21	16.72	17.39	16.90	15.60	15.29	15.98
700	12.18	13.68	13.59	12.69	13.30	14.48	13.49	12.03
800	10.57	12.34	12.14	10.87	11.74	13.55	12.90	10.66
900	13.37	12.57	12.79	13.55	13.21	12.30	12.44	13.37
1000	4.03	3.74	3.69	3.83	3.86	3.34	3.47	3.91
1012								
TOTAL	124.90	125.44	126.75	127.54	128.21	128.86	128.37	126.39

ROW 3	1	2	3	4	5	6	7	8
100	3.29	3.29	3.29	3.29	3.29	3.29	3.29	3.29
200	9.30	9.67	9.79	10.03	10.03	9.42	8.79	8.79
300	16.87	17.07	18.99	20.46	20.47	19.48	18.48	17.44
400	20.18	19.14	18.64	19.41	20.03	19.94	19.76	20.14
500	18.96	18.48	17.85	17.78	17.85	17.29	17.47	18.47
600	16.42	16.31	16.40	16.51	16.39	16.19	16.23	16.49
700	14.89	14.22	13.91	14.63	15.79	16.46	16.21	15.53
800	14.52	13.94	13.30	13.69	14.91	15.80	15.68	15.00
900	14.79	15.24	14.92	14.03	13.77	14.16	14.51	14.54
1000	3.49	3.68	3.68	3.36	3.12	3.15	3.32	3.40
1012								
TOTAL	132.91	131.03	130.77	133.18	135.43	135.19	133.75	133.09

ROW 4	1	2	3	4	5	6	7	8
100	3.29	3.29	3.29	3.29	3.29	3.29	3.29	3.29
200	9.79	10.49	10.71	10.49	10.37	9.91	9.17	8.92
300	20.23	19.67	19.79	21.07	21.84	21.17	20.25	20.18
400	19.82	18.34	20.02	22.69	23.35	23.47	23.42	22.46
500	18.22	17.38	18.83	20.01	20.16	19.79	19.76	19.55
600	17.34	17.38	17.08	16.96	16.75	16.41	16.36	16.86
700	16.26	16.71	15.71	14.71	14.57	14.80	14.94	15.33
800	14.94	15.40	14.44	13.23	13.07	13.60	13.97	14.23
900	13.75	13.99	13.43	12.45	12.04	12.37	12.92	13.33
1000	3.07	3.13	3.06	2.87	2.78	2.83	2.96	3.01
1012								
TOTAL	136.70	135.78	136.17	137.77	138.42	137.64	137.06	137.16

ROW 5	1	2	3	4	5	6	7	8
100	3.29	3.29	3.29	3.29	3.29	3.29	3.29	3.29
200	9.54	10.26	10.49	9.91	8.79	7.83	7.49	8.52
300	18.55	20.42	21.14	19.83	17.00	14.35	14.57	16.53
400	21.45	21.44	21.62	22.50	24.31	25.84	24.74	22.43
500	19.87	19.42	19.48	20.02	20.99	21.72	21.35	20.30
600	17.42	17.29	17.22	17.09	16.81	16.70	16.95	17.32
700	16.11	15.62	15.22	15.20	15.37	15.49	15.75	16.14
800	14.88	14.06	13.60	13.78	14.37	14.80	14.94	14.96
900	13.07	12.73	12.53	12.63	13.02	13.44	13.58	13.41
1000	2.96	2.90	2.89	2.91	2.95	3.01	3.08	3.05
1012								
TOTAL	136.74	137.42	137.45	137.15	136.49	136.46	135.94	135.96

Table C1. Continued on next page.

ROW 6	1	2	3	4	5	6	7	8
100	3.29	3.29	3.29	3.29	3.29	3.29	3.29	3.29
200	8.92	9.30	9.54	9.54	9.42	9.17	8.92	8.65
300	16.73	17.73	19.05	18.64	16.95	16.50	17.10	17.07
400	20.89	21.15	21.60	21.87	21.82	20.79	20.43	20.74
500	20.32	20.11	19.10	18.84	19.29	19.10	18.57	19.17
600	17.71	17.55	16.55	15.96	16.23	16.60	15.61	17.02
700	15.22	15.25	15.50	15.45	15.39	15.88	16.27	15.91
800	13.94	13.72	14.48	14.81	14.77	15.15	15.44	14.68
900	13.09	13.03	13.18	13.40	13.72	13.97	13.88	13.47
1000	3.23	3.14	3.06	3.09	3.20	3.24	3.23	3.24
1012								
TOTAL	133.03	134.27	135.35	134.91	133.89	133.68	133.73	133.15

ROW 7	1	2	3	4	5	6	7	8
100	3.29	3.29	3.29	3.29	3.29	3.29	3.29	3.29
200	8.65	9.17	9.17	8.92	8.39	7.97	7.83	8.11
300	15.36	15.31	15.47	15.80	15.66	14.86	14.44	15.06
400	19.93	20.20	19.47	18.71	19.47	19.97	19.09	18.55
500	18.20	18.56	19.35	19.02	17.88	18.10	18.89	18.82
600	15.27	15.34	16.88	17.39	16.96	15.74	17.15	17.25
700	14.45	14.13	14.69	15.37	15.57	15.54	15.61	15.26
800	14.35	14.12	13.75	14.21	15.20	15.19	14.67	14.24
900	14.00	14.40	13.97	14.05	14.50	14.57	14.28	14.31
1000	3.78	3.73	3.58	3.53	3.78	3.81	3.65	3.70
1012								
TOTAL	127.88	128.24	129.63	130.28	129.69	129.05	129.00	128.61

Table C1. Mean clear region shortwave radiative convergence profiles in W m^{-2} per pressure interval.

ROW 1	1	2	3	4	5	6	7	8
100	0.00	0.00	0.00	0.00	0.00	0.00	0.00	0.00
200	0.00	0.00	0.00	0.00	0.00	0.00	0.00	0.00
300	0.00	0.00	0.00	0.00	0.00	0.00	0.00	0.00
400	0.00	0.00	0.00	0.00	0.00	0.00	0.00	0.00
500	1.82	1.02	1.01	.92	.93	1.92	1.94	1.84
600	3.63	1.02	1.01	.92	.93	3.84	3.88	3.68
700	9.08	1.02	1.01	.92	.93	9.61	9.71	9.21
800	0.00	0.00	0.00	0.00	0.00	0.00	0.00	0.00
900	0.00	0.00	0.00	0.00	0.00	0.00	0.00	0.00
1000	0.00	0.00	0.00	0.00	0.00	0.00	0.00	0.00
1012	0.00	0.00	0.00	0.00	0.00	0.00	0.00	0.00
TOTAL	14.53	3.07	3.03	2.77	2.79	15.37	15.53	14.73

ROW 2	1	2	3	4	5	6	7	8
100	0.00	0.00	0.00	0.00	0.00	0.00	0.00	0.00
200	0.00	0.00	0.00	0.00	0.00	0.00	0.00	0.00
300	0.00	0.00	0.00	0.00	0.00	0.00	0.00	0.00
400	0.00	0.00	0.00	0.00	0.00	0.00	0.00	0.00
500	1.86	1.03	1.05	1.04	1.04	1.95	1.91	1.85
600	3.71	1.03	1.05	1.04	1.04	3.89	3.81	3.71
700	9.28	1.03	1.05	1.04	1.04	9.73	9.53	9.27
800	0.00	0.00	0.00	0.00	0.00	0.00	0.00	0.00
900	0.00	0.00	0.00	0.00	0.00	0.00	0.00	0.00
1000	0.00	0.00	0.00	0.00	0.00	0.00	0.00	0.00
1012	0.00	0.00	0.00	0.00	0.00	0.00	0.00	0.00
TOTAL	14.85	3.08	3.14	3.13	3.12	15.57	15.24	14.82

ROW 3	1	2	3	4	5	6	7	8
100	0.00	0.00	0.00	0.00	0.00	0.00	0.00	0.00
200	0.00	0.00	0.00	0.00	0.00	0.00	0.00	0.00
300	0.00	0.00	0.00	0.00	0.00	0.00	0.00	0.00
400	0.00	0.00	0.00	0.00	0.00	0.00	0.00	0.00
500	2.08	1.09	1.07	1.07	1.09	2.08	2.09	2.09
600	4.15	1.09	1.07	1.07	1.09	4.15	4.17	4.17
700	10.38	1.09	1.07	1.07	1.09	10.38	10.43	10.43
800	0.00	0.00	0.00	0.00	0.00	0.00	0.00	0.00
900	0.00	0.00	0.00	0.00	0.00	0.00	0.00	0.00
1000	0.00	0.00	0.00	0.00	0.00	0.00	0.00	0.00
1012	0.00	0.00	0.00	0.00	0.00	0.00	0.00	0.00
TOTAL	16.61	3.27	3.20	3.20	3.26	16.61	16.69	16.69

ROW 4	1	2	3	4	5	6	7	8
100	0.00	0.00	0.00	0.00	0.00	0.00	0.00	0.00
200	0.00	0.00	0.00	0.00	0.00	0.00	0.00	0.00
300	0.00	0.00	0.00	0.00	0.00	0.00	0.00	0.00
400	0.00	0.00	0.00	0.00	0.00	0.00	0.00	0.00
500	2.09	1.12	1.10	1.07	1.06	1.99	2.02	2.06
600	4.18	1.12	1.10	1.07	1.06	3.99	4.05	4.12
700	10.45	1.12	1.10	1.07	1.06	9.97	10.12	10.29
800	0.00	0.00	0.00	0.00	0.00	0.00	0.00	0.00
900	0.00	0.00	0.00	0.00	0.00	0.00	0.00	0.00
1000	0.00	0.00	0.00	0.00	0.00	0.00	0.00	0.00
1012	0.00	0.00	0.00	0.00	0.00	0.00	0.00	0.00
TOTAL	16.71	3.36	3.29	3.21	3.17	15.96	16.18	16.46

ROW 5	1	2	3	4	5	6	7	8
100	0.00	0.00	0.00	0.00	0.00	0.00	0.00	0.00
200	0.00	0.00	0.00	0.00	0.00	0.00	0.00	0.00
300	0.00	0.00	0.00	0.00	0.00	0.00	0.00	0.00
400	0.00	0.00	0.00	0.00	0.00	0.00	0.00	0.00
500	2.10	1.09	1.08	1.09	1.11	2.13	2.14	2.13
600	4.20	1.09	1.08	1.09	1.11	4.26	4.28	4.26
700	10.49	1.09	1.08	1.09	1.11	10.64	10.71	10.65
800	0.00	0.00	0.00	0.00	0.00	0.00	0.00	0.00
900	0.00	0.00	0.00	0.00	0.00	0.00	0.00	0.00
1000	0.00	0.00	0.00	0.00	0.00	0.00	0.00	0.00
1012	0.00	0.00	0.00	0.00	0.00	0.00	0.00	0.00
TOTAL	16.78	3.28	3.24	3.27	3.34	17.03	17.13	17.04

Table C2. Continued on next page.

ROW 6	1	2	3	4	5	6	7	8
100	0.00	0.00	0.00	0.00	0.00	0.00	0.00	0.00
200	0.00	0.00	0.00	0.00	0.00	0.00	0.00	0.00
300	0.00	0.00	0.00	0.00	0.00	0.00	0.00	0.00
400	0.00	0.00	0.00	0.00	0.00	0.00	0.00	0.00
500	2.08	1.10	1.09	1.09	1.10	2.10	2.10	2.08
600	4.16	1.10	1.09	1.09	1.10	4.20	4.20	4.17
700	10.40	1.10	1.09	1.09	1.10	10.49	10.50	10.42
800	0.00	0.00	0.00	0.00	0.00	0.00	0.00	0.00
900	0.00	0.00	0.00	0.00	0.00	0.00	0.00	0.00
1000	0.00	0.00	0.00	0.00	0.00	0.00	0.00	0.00
1012								
TOTAL	16.64	3.31	3.27	3.26	3.30	16.79	16.80	16.68

ROW 7	1	2	3	4	5	6	7	8
100	0.00	0.00	0.00	0.00	0.00	0.00	0.00	0.00
200	0.00	0.00	0.00	0.00	0.00	0.00	0.00	0.00
300	0.00	0.00	0.00	0.00	0.00	0.00	0.00	0.00
400	0.00	0.00	0.00	0.00	0.00	0.00	0.00	0.00
500	2.02	1.07	1.10	1.11	1.11	2.07	2.11	2.09
600	4.05	1.07	1.10	1.11	1.11	4.15	4.22	4.18
700	10.12	1.07	1.10	1.11	1.11	10.37	10.54	10.45
800	0.00	0.00	0.00	0.00	0.00	0.00	0.00	0.00
900	0.00	0.00	0.00	0.00	0.00	0.00	0.00	0.00
1000	0.00	0.00	0.00	0.00	0.00	0.00	0.00	0.00
1012								
TOTAL	16.19	3.21	3.29	3.34	3.32	16.59	16.87	16.72

Table C2. Shortwave radiative convergence profiles for the aerosol regions of the wave (W m^{-2} per pressure interval).

CLOUD PERCENTAGE FOR DAYTIME B ARRAY

	1	2	3	4	5	6	7	8
100	3.01	13.37	11.05	11.24	14.06	1.49	.78	2.34
200	5.93	13.64	12.33	22.53	15.89	6.10	2.71	3.14
300	5.27	11.27	9.95	20.02	12.28	9.93	4.70	3.55
400	6.48	10.98	11.58	14.37	8.89	19.60	8.21	4.94
500	7.12	7.42	11.47	9.53	10.57	17.13	13.47	8.19
600	7.34	8.33	10.93	7.99	10.19	13.48	15.04	10.61
700	9.98	7.90	9.03	5.96	8.12	9.99	12.80	10.52
800	11.05	7.58	7.13	4.51	8.21	7.92	13.25	12.34
900	16.13	8.70	5.47	2.54	5.34	5.99	13.66	15.77
1000	25.98	10.80	11.07	1.29	6.45	8.37	15.37	28.37
1012 OTAL	99.99	100.01	100.01	99.98	100.00	100.00	99.99	100.01

IR CONVERGENCE FOR DAYTIME B ARRAY

	1	2	3	4	5	6	7	8
100	-7.27	-12.72	-11.01	-11.24	-12.90	-6.55	-6.24	-6.89
200	-17.08	-19.61	-19.90	-23.86	-20.88	-17.60	-16.09	-16.24
300	-24.83	-24.94	-24.65	-29.27	-25.12	-27.63	-25.06	-24.03
400	-26.10	-24.73	-26.05	-24.88	-22.58	-35.37	-28.57	-26.05
500	-27.97	-22.27	-26.47	-20.14	-24.36	-32.87	-34.61	-30.09
600	-26.16	-20.65	-22.39	-16.21	-21.02	-24.06	-30.41	-29.33
700	-28.67	-19.78	-19.29	-14.02	-18.06	-19.18	-26.69	-29.17
800	-24.24	-16.06	-14.84	-11.11	-14.15	-14.43	-20.46	-24.47
900	-14.35	-9.81	-9.43	-7.76	-7.81	-9.79	-11.29	-14.02
1000	-4.00	-3.98	-4.03	-4.01	-3.94	-4.05	-3.94	-4.01
1012 OTAL	-200.47	-174.55	-178.06	-162.50	-170.82	-191.53	-203.36	-204.30

SW CONVERGENCE FOR DAYTIME B ARRAY

	1	2	3	4	5	6	7	8
100	6.39	12.41	10.43	9.24	9.91	6.51	5.80	6.01
200	13.08	18.85	18.27	20.63	17.07	14.56	11.91	12.43
300	21.81	17.86	19.41	21.64	20.27	23.59	22.56	21.90
400	21.95	14.47	17.26	16.01	17.69	22.80	23.58	22.82
500	21.39	12.53	15.85	12.73	16.71	20.83	24.21	22.92
600	17.68	10.71	12.00	8.78	13.79	15.08	21.56	21.39
700	15.35	7.97	7.93	5.40	9.06	9.88	16.19	16.48
800	12.78	6.62	5.10	3.23	7.01	6.62	12.37	13.10
900	10.37	5.30	3.14	1.58	4.16	4.19	8.69	9.38
1000	.55	.29	.20	.03	.17	.19	.36	.46
1012 OTAL	141.35	107.01	109.59	99.27	116.44	124.25	147.23	146.89

IR+SW CONVERGENCE FOR DAYTIME B ARRAY

	1	2	3	4	5	6	7	8
100	-.88	-.31	-.58	-2.00	-2.99	-.04	-.44	-.88
200	-4.00	-.76	-1.63	-3.23	-3.81	-3.04	-4.18	-3.81
300	-2.82	-7.08	-5.24	-7.63	-4.85	-4.04	-2.50	-2.13
400	-4.15	-10.26	-8.79	-8.87	-4.89	-12.57	-4.99	-3.23
500	-6.58	-9.74	-10.62	-7.41	-7.65	-12.04	-10.40	-7.17
600	-8.48	-9.94	-10.39	-7.43	-7.23	-8.98	-8.85	-7.94
700	-13.32	-11.81	-11.36	-9.62	-8.40	-9.30	-10.50	-12.69
800	-11.46	-9.44	-9.74	-7.88	-7.14	-7.81	-8.09	-11.37
900	-3.98	-4.51	-6.29	-6.18	-3.65	-5.60	-2.60	-4.64
1000	-3.45	-3.69	-3.83	-3.94	-3.77	-3.86	-3.58	-3.55
1012 OTAL	-59.12	-67.54	-68.47	-63.23	-54.38	-67.28	-56.13	-57.41

Table D1. Mean daytime profiles for the B-scale array as a function of wave column. Convergence profiles are W m^{-2} per pressure interval.

CLOUD PERCENTAGE FOR NIGHT TIME B ARRAY

	1	2	3	4	5	6	7	8
100	11.89	9.80	3.93	12.24	16.75	.41	2.29	2.81
200	8.52	11.94	7.25	20.91	19.32	1.54	3.14	3.08
300	9.97	11.52	9.73	24.12	15.75	7.28	6.98	3.54
400	6.14	13.30	11.80	14.53	9.31	24.67	15.68	5.48
500	4.81	8.74	12.02	8.41	11.04	21.11	22.57	8.23
600	8.01	9.33	12.97	7.23	9.28	15.49	15.67	8.35
700	9.90	9.34	11.49	5.40	6.31	10.67	10.08	9.44
800	10.44	8.12	9.98	3.16	5.61	7.54	7.47	10.65
900	10.15	9.22	9.01	1.60	3.26	4.37	5.38	15.33
1000	20.15	8.69	11.82	2.39	3.38	6.93	10.73	33.09
1012								
TOTAL	99.98	100.00	100.00	99.99	100.01	100.01	99.99	100.00

IR CONVERGENCE FOR NIGHT TIME B ARRAY

	1	2	3	4	5	6	7	8
100	-11.89	-11.11	-7.56	-11.87	-14.60	-6.04	-7.01	-7.16
200	-17.16	-18.95	-18.05	-23.24	-22.03	-15.91	-16.35	-16.15
300	-25.46	-26.22	-26.82	-31.30	-25.97	-26.96	-26.26	-23.94
400	-22.79	-27.54	-28.92	-25.03	-21.23	-40.70	-33.13	-26.21
500	-22.83	-24.07	-29.62	-18.30	-22.54	-36.38	-39.42	-29.78
600	-24.21	-21.48	-26.16	-15.09	-18.18	-24.97	-25.45	-27.68
700	-24.87	-20.51	-22.76	-13.36	-14.76	-18.13	-19.33	-29.12
800	-20.06	-15.84	-17.24	-10.60	-11.83	-13.02	-14.15	-25.00
900	-10.88	-9.58	-10.31	-7.87	-7.08	-9.40	-9.60	-14.84
1000	-3.93	-3.95	-4.01	-4.02	-3.96	-4.07	-4.04	-4.05
1012								
TOTAL	-184.08	-179.25	-191.45	-160.68	-162.18	-195.58	-194.74	-203.93

Table D2. Mean nighttime profiles for the B-scale array as a function of wave column.

CLOUD PERCENTAGE FOR DAYTIME A/B ARRAY

	1	2	3	4	5	6	7	8
100	5.24	7.04	6.26	9.67	9.44	2.82	.97	1.69
200	6.47	11.54	8.67	15.32	11.70	6.31	3.50	2.94
300	5.93	9.79	7.63	13.75	11.10	9.01	5.64	3.84
400	7.04	8.89	9.92	13.23	12.81	16.00	9.88	5.56
500	6.82	8.05	10.94	11.32	11.67	14.21	12.41	9.10
600	8.29	9.32	10.94	10.39	10.73	12.60	14.31	10.93
700	10.42	10.43	10.10	8.60	9.90	10.39	12.40	10.75
800	9.31	8.53	9.54	7.37	8.91	9.11	12.03	11.36
900	14.46	10.31	10.02	5.10	6.73	8.94	13.98	15.40
1000	26.02	16.12	15.97	5.25	7.31	10.62	15.29	28.43
1012								
TOTAL	100.00	100.02	99.99	100.00	100.00	100.01	100.01	100.00

IR CONVERGENCE FOR DAYTIME A/B ARRAY

	1	2	3	4	5	6	7	8
100	-8.46	-9.41	-8.79	-10.61	-10.80	-7.20	-6.28	-6.62
200	-17.35	-19.21	-18.48	-20.99	-19.29	-17.56	-16.46	-16.16
300	-24.28	-25.70	-24.83	-26.83	-25.88	-26.82	-25.65	-24.33
400	-25.90	-25.24	-26.90	-26.52	-27.17	-32.33	-28.73	-26.69
500	-26.71	-25.17	-28.62	-25.00	-27.05	-31.33	-32.95	-30.76
600	-26.00	-23.74	-25.10	-20.68	-22.07	-24.90	-29.75	-29.45
700	-27.34	-23.52	-23.20	-17.75	-19.68	-21.31	-26.43	-28.96
800	-22.39	-18.38	-18.43	-13.57	-14.95	-16.52	-20.18	-23.90
900	-13.61	-11.38	-11.18	-8.44	-8.69	-10.28	-11.39	-13.86
1000	-4.03	-4.03	-4.02	-3.99	-3.97	-4.01	-3.95	-4.01
1012								
TOTAL	-196.07	-185.78	-189.55	-174.38	-179.55	-192.26	-201.77	-204.74

SW CONVERGENCE FOR DAYTIME A/B ARRAY

	1	2	3	4	5	6	7	8
100	7.40	9.32	8.14	8.64	8.90	6.85	5.93	6.03
200	13.63	16.83	15.37	17.84	15.76	14.10	12.38	12.29
300	21.23	20.28	20.90	21.71	21.45	22.89	22.67	21.90
400	21.11	17.56	20.08	18.32	19.53	22.45	23.37	22.81
500	20.08	15.76	19.02	16.31	18.19	20.97	23.39	22.90
600	17.63	13.29	15.91	12.22	14.43	16.06	20.44	21.04
700	14.46	10.49	12.12	8.17	10.28	11.23	15.35	16.30
800	11.53	8.32	9.01	5.59	7.29	8.20	11.54	12.70
900	9.10	6.50	6.30	3.36	4.41	5.67	8.03	9.74
1000	.53	.44	.34	.13	.19	.25	.36	.54
1012								
TOTAL	136.30	118.79	127.19	112.29	120.43	128.67	143.46	146.25

IR+SW CONVERGENCE FOR DAYTIME A/B ARRAY

	1	2	3	4	5	6	7	8
100	-1.06	-.09	-.65	-1.97	-1.90	-.35	-.35	-.59
200	-3.72	-2.38	-3.11	-3.15	-3.53	-3.46	-4.08	-3.87
300	-3.05	-5.42	-3.93	-5.12	-4.43	-3.93	-2.98	-2.43
400	-4.79	-7.68	-6.82	-8.20	-7.64	-9.88	-5.36	-3.88
500	-6.63	-9.41	-9.60	-8.69	-8.86	-10.36	-9.56	-7.86
600	-8.77	-10.45	-9.19	-8.46	-7.64	-8.84	-9.31	-8.41
700	-12.88	-13.03	-11.08	-9.58	-9.40	-10.08	-11.08	-12.66
800	-10.86	-10.06	-9.42	-7.98	-7.66	-8.32	-8.64	-11.20
900	-4.91	-4.88	-4.88	-5.08	-4.28	-4.61	-3.36	-4.12
1000	-3.90	-3.59	-3.68	-3.86	-3.78	-3.76	-3.59	-3.47
1012								
TOTAL	-59.77	-66.99	-62.36	-62.09	-59.12	-63.59	-58.31	-58.49

Table D3. Mean daytime profiles for the A/B-scale array as a function of wave column.

CLOUD PERCENTAGE FOR NIGHT TIME A/B ARRAY

	1	2	3	4	5	6	7	8
100	6.41	5.28	3.67	11.72	10.49	1.97	1.52	1.78
200	5.56	10.03	6.83	13.21	12.01	4.47	3.61	2.74
300	8.20	9.85	7.53	14.33	12.23	8.74	7.82	4.14
400	14.30	9.70	12.09	13.72	15.43	18.58	13.71	6.47
500	8.00	9.26	13.56	11.45	12.38	16.91	16.27	9.35
600	9.03	10.35	12.00	10.92	10.34	13.90	15.35	9.63
700	10.23	12.10	10.01	9.38	8.90	11.29	10.77	10.25
800	8.21	9.63	9.37	6.96	7.52	8.72	8.55	10.87
900	9.03	11.31	11.55	4.07	6.03	6.17	11.60	15.10
1000	21.03	12.50	13.39	4.23	4.67	9.25	10.80	29.66
1012								
TOTAL	100.00	100.01	100.00	99.99	100.00	100.00	100.00	99.99

IR CONVERGENCE FOR NIGHT TIME A/B ARRAY

	1	2	3	4	5	6	7	8
100	-8.99	-8.56	-7.51	-11.81	-11.60	-6.78	-6.60	-6.68
200	-17.04	-18.70	-17.81	-20.03	-19.26	-16.94	-16.49	-16.07
300	-25.35	-26.35	-25.72	-26.78	-26.03	-27.05	-26.84	-24.48
400	-30.87	-26.55	-29.30	-27.13	-28.50	-34.92	-31.34	-27.25
500	-26.20	-26.77	-31.47	-24.66	-27.02	-33.41	-35.09	-30.89
600	-23.85	-24.69	-25.57	-20.72	-20.43	-25.19	-27.51	-28.29
700	-24.03	-24.26	-22.65	-17.45	-17.79	-20.41	-22.04	-28.73
800	-19.11	-18.10	-18.10	-12.63	-13.47	-15.02	-16.67	-24.04
900	-11.72	-10.73	-11.13	-7.84	-8.28	-9.65	-10.64	-13.99
1000	-4.03	-3.98	-4.00	-3.98	-3.97	-4.03	-3.98	-4.01
1012								
TOTAL	-191.19	-188.69	-193.26	-173.03	-176.35	-193.40	-197.20	-204.43

Table D4. Mean nighttime profiles for the A/B-scale array as a function of wave column.

BIBLIOGRAPHIC DATA SHEET	1. Report No. CSU-ATS-324	2.	3. Recipient's Accession No.
4. Title and Subtitle GATE PHASE III MEAN SYNOPTIC-SCALE RADIATIVE CONVERGENCE PROFILES			5. Report Date April, 1980 6.
7. Author(s) Steven A. Ackerman and Stephen K. Cox			8. Performing Organization Rept. No. CSU-ATS-324
9. Performing Organization Name and Address Department of Atmospheric Science Colorado State University Fort Collins, Colorado 80523			10. Project/Task/Work Unit No. 11. Contract/Grant No. ATM-78-05743 / ATM-78-12631
12. Sponsoring Organization Name and Address National Science Foundation, NOAA			13. Type of Report & Period Covered 14.

15. Supplementary Notes

16. Abstracts

Tropospheric radiative convergence profiles were derived for an easterly wave composite during Phase III of the GATE. The easterly waves observed during this period were generally well developed. The profiles also represent the magnitude and the spatial distribution of the Intertropical Convergence Zone (ITCZ) in the GATE area. The 12 hour mean daytime and nighttime profiles are presented. Cloud top pressure distributions, as a function of wave position, are also presented. Day-night differences in the cloud top pressure distributions and radiative convergence profiles are discussed.

The results of this research indicate three possible radiative induced mechanisms which contribute to the observed diurnal cycle in mass convergence. The are:

1) Radiative convergence differences between the ITCZ and the surrounding regions;

2) Mesoscale raditive convergence differences between clear cluster regions and; 3) a nighttime upper-level tropospheric cooling maximum that is centered one-half a wavelength from the region of maximum convective activity.

17. Key Words and Document Analysis. 17a. Descriptors

Radiative convergence profiles
Cloud top distributions
GATE Phase III
Diurnal variability
Synoptic-scale composite

17b. Identifiers/Open-Ended Terms

17c. COSATI Field/Group

18. Availability Statement	19. Security Class (This Report) UNCLASSIFIED	21. No. of Pages 119
	20. Security Class (This Page) UNCLASSIFIED	22. Price

FORM NTIS-35 (Rev. 3-72)